Molecular Dynamics at Water Interfaces: From Astrophysical to Biochemical Applications

Inauguraldissertation

zur
Erlangung der Würde eines Doktors der Philosophie
vorgelegt der
Philosophisch-Naturwissenschaftlichen Fakultät
der Universität Basel

von
Marco Pezzella
aus Italien

Basel, 2020

Originaldokument gespeichert auf dem Dokumentenserver der Universität Basel
`https://edoc.unibas.ch`

This work is licensed under a Creative Commons BY-NC-SA 4.0 International License.

Genehmigt von der Philosophisch-Naturwissenschaftlichen Fakultät auf Antrag von:

Prof. Dr. Markus Meuwly
Prof. Dr. Jonathan Tennyson

Basel, 21. April 2020

Prof. Dr. Martin Spiess, Dekan

Contents

Acknowledgements vii

Abstract ix

I. Introduction and Methods 1

II. Oxygen formation in interstellar media 3

1. Molecular oxygen formation in interstellar ice does not require tunneling 5

1.1. The role of the Zwanzig equation for rough potentials 6

1.2. New FES 8

2. O_2 formation in cold environments 21

2.1. MS-ARMD 21

2.2. The KKY water model 23

2.3. Vibrational relaxation 25

3. Recombination of O_2 in ground and excited states 41

3.1. Spin orbit coupling 43

III. Hydrophobicity 69

4. Water Dynamics Around Proteins: T- and R-States of Hemoglobin and Melittin 71

4.1. Simulation set-up and analysis 72
4.2. Hydration Dynamics around Hemoglibin 74
4.3. Hydration Dynamics around Melittin 93
4.4. Conclusions 107

IV. Conclusion and Outlook 109

V. Appendix 115

5. A distributed charge approach to molecular dynamics simulations models 117

5.1. iAMOEBA/(M)DCM in OpenMM 118

6. Contributions in CHARMM 125

6.1. EXTBOND 125
6.2. TRIAKERN 128

References 132

The Ancient of Days in *Europe a Prophecy*, copy copy K from the Fitzwilliam Museum, ©2001 Fitzwilliam Museum

Obscurum per obscurius, ignotum per ignotius.

Alchemical motto.

Acknowledgements

First of all I would like to thank Professor Markus Meuwly for being my supervisor of my doctoral study, his patience and his advice during this period of my life, and professor Jonathan Tennyson for accepting to be my second supervisor.

Special thanks to all the colleagues I met during all these years: Mike, Oliver, Silvan, Luis, Meenu, Krystel, Juan Carlos, Jasmine, Padma, Sarbani, Maryam, Taylan, Eric Uxia and Akshay. A special thanks goes to Zhen-Hao, Polydefkis and Florent for helping me during the first months in Basel. Thanks to Debasish for the useful science discussion and the indian cuisine, Sebastian (and Sarah) and Otoniel for being not only colleauges but also good friends. At last but not least, especially because thanks to his advice this thesis is written in proper English, thanks Ali!

Grazie mille con abbraccione incluso to the friends I have made here in Basel: Marco, Maddalena, Matteo, Andrea, Fede, Stefano (sigh), Angelo, Flavio e Miranda. I hope to not have scandalized you too much (Stefano is excluded here, he is notoriously the bottom of what the human kind can reach)! One day, when pigs fly (and not shot by a dam), I will be a perfect educated and elegant person.

Thanks to my family for bearing me, the closest Mà, Pà, Francesca, Mamm' Elia, and the extended Sean, Gayle, Lorenza Malì and Luca.

Obviously thanks to all the people that are still part of my life that are scattered all around, here I am giving just a sample: Francesco, Simone, Marta, Mattia, Carlo, Michela, Vale, Piero, Maresciallo Matteo Cameli (or whatever is your grade), Aneta , Luc Pasq, the MM's, Nicola, Luca Martino , Serena, Alessandra, Marcella, Stefano, Matteo Iafrate (sorry, too many Matteo and Luca), Andrea, Gaia, Acebes, Veronica, Maria, Marta, Sara, Marco Baldazzi and Luca Schio.

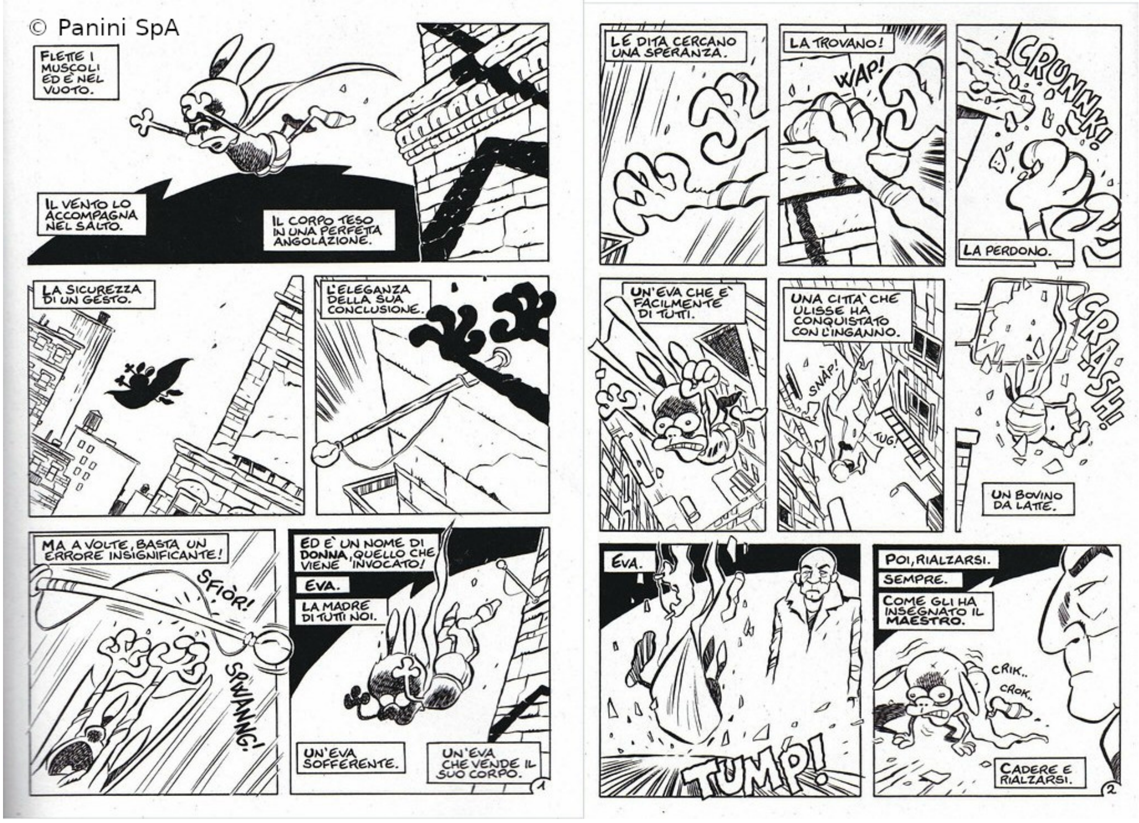
© Panini SpA
FLETTE I MUSCOLI ED È NEL VUOTO.
IL VENTO LO ACCOMPAGNA NEL SALTO.
IL CORPO TESO IN UNA PERFETTA ANGOLAZIONE.
LA SICUREZZA DI UN GESTO.
L'ELEGANZA DELLA SUA CONCLUSIONE.
MA A VOLTE, BASTA UN ERRORE INSIGNIFICANTE!
SFIÒR!
SBWANNG!
ED È UN NOME DI DONNA, QUELLO CHE VIENE INVOCATO!
EVA.
LA MADRE DI TUTTI NOI.
UN'EVA SOFFERENTE.
UN'EVA CHE VENDE IL SUO CORPO.
1
LE DITA CERCANO UNA SPERANZA.
LA TROVANO!
WAP!
CRUNNK!
LA PERDONO.
UN'EVA CHE È FACILMENTE DI TUTTI.
UNA CITTÀ CHE ULISSE HA CONQUISTATO CON L'INGANNO.
SNÀP!
TUG!
GRASH!
UN BOVINO DA LATTE.
EVA.
TUMP!
POI, RIALZARSI.
SEMPRE.
COME GLI HA INSEGNATO IL MAESTRO.
CRIK..
CROK..
CADERE E RIALZARSI.
2

A metaphor of the scientific method by Leo Ortolani. ©1997 Panini SpA

Abstract

This PhD thesis investgates the chemical and physical interactions between water and systems of different sizes. The first section illustrates the chemical context of the projects and methodological basis used.

The second part studies the dynamics and reactivity of small systems of astrochemical interest on top of water ice, at each step the complexity of the model is increased. Initially the ice surface is characterized, then different aspects of the reaction are examined.

The final part explores the interactions between water molecules and two different proteins, to understand water's role as solvent and how it influences protein macromolecule dynamics.

The appendix includes a discussion on the interatomic interaction of water and the contribution apported in CHARMM software package are presented.

Part I.

Introduction and Methods

Part II.

Oxygen formation in interstellar media

1. Molecular oxygen formation in interstellar ice does not require tunneling

Quantum nuclear effects are known to increase a reactions efficiency and reactivity. An atom can pass through an energy barrier without having sufficient energy for crossing it due to tunneling effects. The tunneling probability is inversely proportional to the mass of the particle and the temperature of the system. A pictorial representation is given in Figure 1.1. This relation is expressed by the de Broglie wavelength (λ):

$$\lambda = \frac{h}{mv} = \frac{h}{\sqrt{2mk_BT}} \tag{1.1}$$

This effect is more efficient for light atoms, $\lambda_{\mathrm{H}}(10\mathrm{K}) = 0.98$ nm than for heavy atoms, i.e. $\lambda_{\mathrm{O}} = 0.24$ nm. In the ISM, for temperatures T$\leq$ 10 K, H diffusion and H_2 formation on top of water surfaces is supposed to be enhanced by tunneling[1]. Studies on water ice surfaces show how this effect is dramatically affected by the grain morphology. In crystalline water, both diffusion and reactivity are positively enhanced by tunneling[2,3] but it is still debated for ASW. Senevirathne et *al*[4] observed that tunneling is always prominent, while others[2,3,5] reported that tunneling has almost no contribution in diffusion processes. Those studies agree that quantum tunneling is suppressed in ASW because of non-periodic potential. Possible effects can be observed only for nearest-neighbour hops.

Given these consideration, it was surprising to observe experimental interpretation of

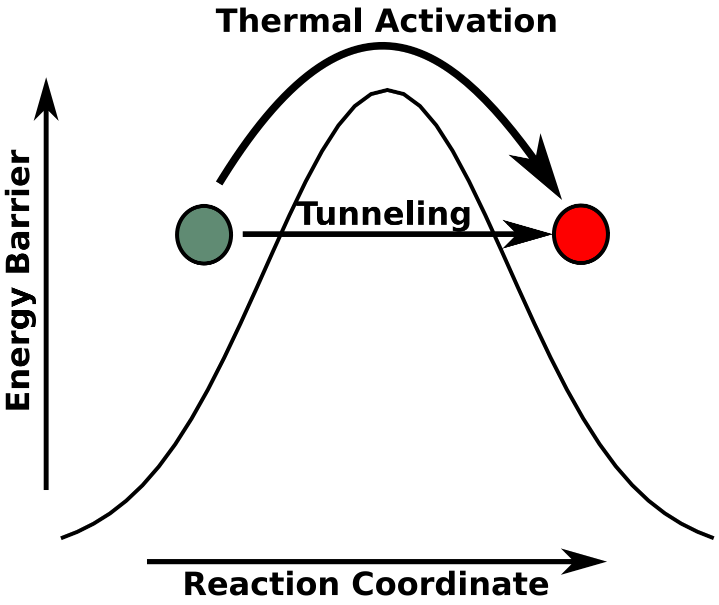

Figure 1.1.: General representation of the tunneling vs thermal activated reaction. Two different colors, green and red, are used to distinguish between reactants and products.

heavy atom diffusion (specifically O) on ASW through quantum diffusion[6]. In this chapter this process is studied to observe if quantum effects actually play a role or if classic physics fully explains the atom dynamics. All procedure and results are described in the article, and it is preceded by two insights. Details on the Zwanzing equation are illustrated in the first section, while information on how the free energy surface is built will be found in the second.

1.1. The role of the Zwanzig equation for rough potentials

Protein folding[7] and diffusion of particles on glassy surfaces[8] occurs on a hierarchical PES, where a minimum is inside another minimum. A PES structured in this way is defined as *rough* PES.

The roughness is defined by the characteristic potential energy scale ϵ of the PES. For temperature $T < \epsilon$ the diffusion process is dramatically slowed down, while for $T > \epsilon$ it is not affected. As a consequence, the Arrhenius-like diffusion equation (see Eq. **??**) should not be used for low temperatures regimes.

The mathematical derivation of the diffusion expression for a rough surface was derived in 1988 by Zwanzig[9]. It was derived for a one dimensional rough potential $U(x)$ along a general x dimension. This potential has a smooth background component $U_0(x)$ on which a random potential $U_1(x)$ is superimposed.

$$U(x) = U_0(x) + U_1(x) \tag{1.2}$$

The effective diffusion coefficient D_{eff} was derived from the result for D from Equation **??**:

$$D_{\text{eff}} = \frac{D}{\mathrm{e}^{\beta U_1} e^{-\beta U_1}} \tag{1.3}$$

with

$$e^{\beta U_1} e^{-\beta U_1} = \mathrm{e}^{(\beta\epsilon)^2}, \tag{1.4}$$

obtaining the expression:

$$D_{\text{eff}} = D\mathrm{e}^{-(\beta\epsilon)^2}. \tag{1.5}$$

In this work Equation 1.5 is used to understand how diffusion processes takes place on the ASW surface, finding that the experimental observations from Ref[6] can be qualitatively explained by classic mechanics. A perfect agreement with experimental data is obtained if contribution from the zero point energy are taken into account[10,11]. This interpretation is confirmed as well from the direct comparison between classical and quantum dynamics.

1.2. New FES

A key information for the determination of the interaction between O and ASW surface is the knowledge of free energy surface (FES) along the diffusion path. The probability distribution $P(x, y)$ is determined by MC simulations, the details of which are reported in the article. The free energy $G(x, y)$ is then calculated using the expression:

$$G(x, y) = k_\mathrm{B}T \ln(P(x, y)) \tag{1.6}$$

As reported in the article the interaction between H_2O and O was reparametrized, *via* the oxygen van der Waals interactions, for improving the agreement between our simulations and experimental data[12]. The problem is that the strong interaction precludes the complete sampling of the FES: only the 60% of the grid is sampled. In order to overcome this difficulty, the same MC simulations were repeated with the original CHARMM36 FF[13], in combination with the evaluation of the PES for each grid point with both parameter sets.

Knowing that the Helmotz free energy (A) is related to the potential energy (U) and Gibbs free energy (g) by the expression:

$$A = U - TS = G - pV \tag{1.7}$$

where S is the entropy of the system, V is the volume and p is the pressure of the system. In case of the ASW-vacuum interface $p = 0$ leading to $G = A$. For each grid point on the surface, U is estimated for $N = 11$ different values along the z direction, from the minimum dwell to the height where the surface and O don't interact, equispaced by 1 Å. The three dimensional PES can be reduced to a 2D problem performing a Maxwell-Boltzmann average along z.

For each single (x, y) element, the difference (ΔU_{z_i}) between each value in z (U_{z_i}) and its minimum $(\min(U_{z_i}))$ is performed,

$$\Delta U_{z_i} = U_{z_i} - \min(U_{z_i}) \tag{1.8}$$

ΔU_{z_i} is then used for calculating the Maxwell-Boltzann probability $(p(\Delta U_{z_i}))$

$$p(\Delta U_{z_i}) = \exp\left(\frac{\Delta U_{z_i}}{k_{\mathrm{B}T}}\right) \tag{1.9}$$

which is then used for evaluating the weight in the z position (k_i).

$$k_i = \frac{p(\Delta U_{z_i})}{\sum_{i=1}^{N} p(\Delta U_{z_i})} \tag{1.10}$$

The averaged PES for each point can be then rewritten as:

$$\langle U \rangle (x, y) = \sum_{i=1}^{N} k_i U_(x, y, z_i) \tag{1.11}$$

For both the complete and incomplete FES, the potential energy contribution is subtracted in order to obtain the entropic contribution TS. A linear regression fitting is then performed within the two models:

$$TS = m \times TS_{\mathrm{orig}} + q \tag{1.12}$$

where TS is the entropic contribution for the target FES, TS_{orig} the contribution from the original CHARMM parameters, $m = 1.92 \pm 0.02$ is the slope of the regression and $q = 0.60 \pm 0.01$ kcal/mol its intercept. A correlation coefficient of 0.925 is found between the true and the fitted values. In Figure 1.2 the correlation is shown. The values from the regression allow to obtain missing points in the FES.

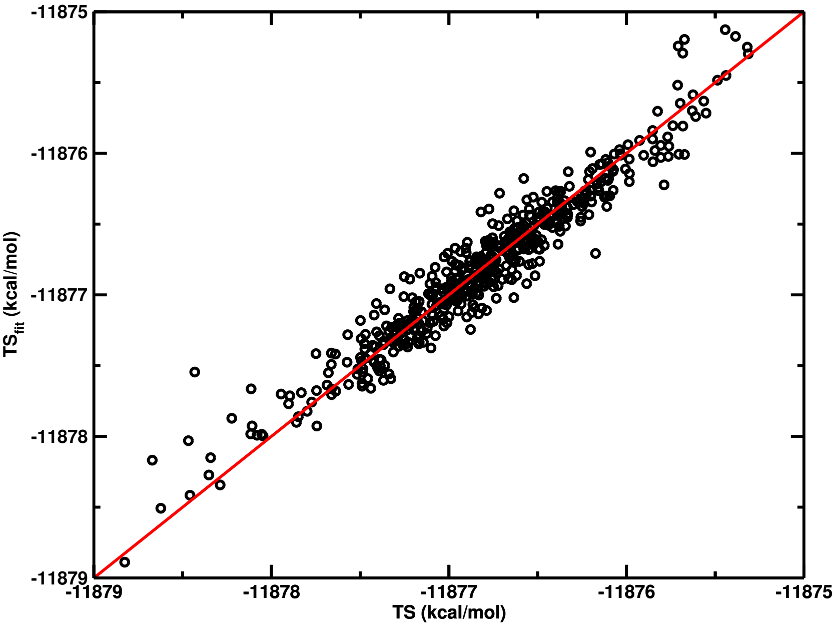

Figure 1.2.: Correlation between the original data from MC simulations (TS) and the fitted data (TS_{fit}).

The Journal of Physical Chemistry Letters

Letter

Cite This: J. Phys. Chem. Lett. 2018, 9, 1822−1826

pubs.acs.org/JPCL

Downloaded via UNIV OF BASEL on September 25, 2019 at 08:18:36 (UTC).
See https://pubs.acs.org/sharingguidelines for options on how to legitimately share published articles.

Molecular Oxygen Formation in Interstellar Ices Does Not Require Tunneling

Marco Pezzella, Oliver T. Unke, and Markus Meuwly*

Department of Chemistry, University of Basel, Klingelbergstrasse 80, 4056 Basel, Switzerland

Supporting Information

ABSTRACT: The formation of molecular oxygen in and on amorphous ice in the interstellar medium requires oxygen diffusion to take place. Recent experiments suggest that this process involves quantum tunneling of the oxygen atoms at sufficiently low temperatures. Fitting experimental diffusion rates between 6 and 25 K to an expression that accounts for the roughness of the surface yields excellent agreement. The molecular dynamics of adsorbed oxygen is characterized by rapid intrasite dynamics, followed by intersite transitions over distances of ∼10 Å. Explicit simulations using a realistic free-energy surface for oxygen diffusion on amorphous ice down to 10 K show that quantum tunneling is not required for mobility of adsorbed oxygen. This is confirmed by comparing quantum and classical simulations using the same free-energy surface. The ratio of diffusional and desorption energy $E_{dif}/E_{des} = 275/1082 \approx 0.3$ is at the lower end of typically used values but is still consistent with the assumptions made in models for interstellar chemistry.

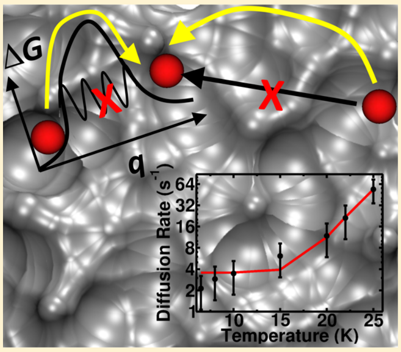

The diffusion of oxygen atoms in and on interstellar ice grains is of fundamental importance for the formation of CO_2 and molecular oxygen O_2.[1−3] In addition, O diffusion has also been implicated in the formation of ozone in laboratory experiments[4,5] within a Langmuir−Hinshelwood mechanism (surface diffusion) and has been proposed to be relevant for interstellar grains,[1] eventually leading to the formation of water,[5] although the major water-formation pathway involves mobile hydrogen atoms.

In all of these cases the diffusion of atomic oxygen is a primary driver for forming di- or triatomic molecules under conditions typical for interstellar environments. These include higher temperatures ($T \approx 50$ K) for translucent and diffuse clouds and temperatures $T \approx 10$ K for dense molecular clouds.[1,6] Questions of particular relevance pertain to the diffusional barrier for intersite migration of oxygen atoms on amorphous solid water (ASW) and their desorption energies away from the surface. For this, experiments based on temperature-programmed desorption have been used.[4,7]

For analyzing the diffusion rate (i.e., the probability for one hop between different adsorption sites in s^{-1}, which is referred to as D in ref 4) of atomic oxygen on ASW, either an Arrhenius expression ($D(T) \approx Ae^{(-\beta E_{dif})}$, where E_{dif} is a conformationally averaged diffusional barrier and $\beta = 1/(k_BT)$) or an expression accounting for tunneling through a square well barrier was used.[4,7] A diffusion coefficient D_{dif} (in units of length^2/time) can be converted into a diffusion rate D (in 1/time) through $D = D_{dif}/a^2$, where a^2 is a typical area sampled by the adsorbate between consecutive hops (see Figure S1). Typically, a^2 is on the order of 10 Å^2, which corresponds to 10^{15} adsorption sites/cm^2.[8] Using temperature-programmed desorption, the formation of molecular oxygen and ozone from atomic oxygen was studied on amorphous solid water and crystalline water.[4] From monitoring the relative amounts of the two molecular species $n(O_3)/n(O_2)$ as a function of temperature (between 6 and 25 K), the oxygen diffusion rate as a function of temperature was obtained. These data were analyzed by assuming an Arrhenius law with an activation energy of 450 K and a prefactor of 10^{12} s^{-1}, which was unable to describe the temperature dependence (see blue line in Figure 1).[4,7] Alternatively, a model that accounts for tunneling through a square barrier was used, which, however, also did not yield a satisfactory fit using a typical activation energy of 500 K and a barrier width of 1 Å.[4]

However, it is to be noted that such models assume homogeneous, noncorrugated (i.e., "smooth") surfaces on which the diffusing particle moves. Once the surface contains variations on atomic length scales ("roughness" of scale ϵ, see Figure 1), as is typical for ASW, the temperature dependence of the diffusion rate may change. Diffusion in a rough, 1D potential was investigated by Zwanzig, who found that the motion of a particle on a rough potential energy surface (PES) is characterized by an effective diffusion coefficient D^*_{dif}.[9] If the roughness of the surface is random, independent of position x, and Gaussian-distributed in ϵ (the scale of the roughness), then the effective diffusion coefficient is $D^*_{dif} = D_{dif}e^{-(\beta\epsilon)^2}$, where D_{dif} is the diffusion coefficient on the surface with zero roughness. On the contrary, for a periodic perturbation $\propto \epsilon \cos(qx)$ of the roughness with periodicity q the effective diffusion coefficient at low temperatures is $D^*_{dif} = D_{dif}e^{-(2\beta\epsilon)}$, that is, an Arrhenius dependence.

Received: January 31, 2018
Accepted: March 25, 2018
Published: March 26, 2018

ACS Publications © 2018 American Chemical Society

DOI: 10.1021/acs.jpclett.8b00328
J. Phys. Chem. Lett. 2018, 9, 1822−1826

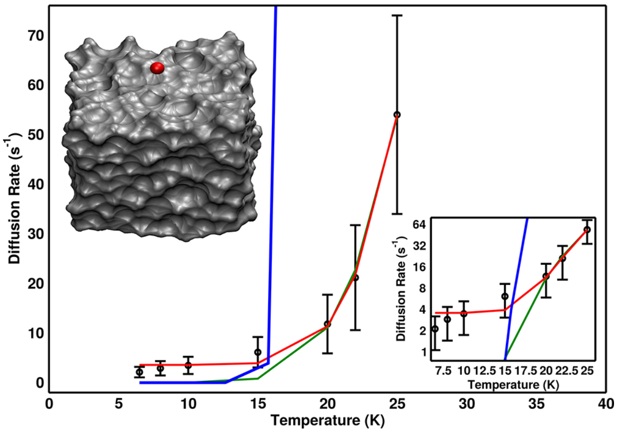

Figure 1. Different models for oxygen diffusion at low temperatures (6−25 K). Experimental points and error bars are those from ref 4. The blue curve is the Arrhenius expression using the parameters from ref 4 (Figure 2, $D = Ae^{(-\beta\epsilon)}$ with $A = 10^{12}$ s^{-1} and $\epsilon = 450$ K), which fails to describe the experimental data. Fitting to an expression suggested in ref 9 ($D^* = De^{-(\epsilon/T)^2}$, $D = 2.88 \times 10^4 \pm 2.61 \times 10^4$ s^{-1}, $\epsilon = 78.6 \pm 11.0$ K, green line) describes the data down to 20 K. Allowing for finite diffusion down to very low temperatures ($D^* = D_0 + De^{-(\epsilon/T)^2}$, $D_0 = 3.75 \pm 0.70$ s^{-1}, $D = 8.83 \times 10^4 \pm 4.82 \times 10^4$ s^{-1}, $\epsilon = 93.4 \pm 6.8$ K, red curve) reproduces the experimental data to 6 K. The inset reports the y axis on a logarithmic scale.

Because an Arrhenius expression does not manifestly describe the diffusion at low temperatures correctly, we used an expression $D^* = D_0 + De^{-(\beta\epsilon)^2}$ in which D_0, D, and ϵ are adjustable parameters to fit the experimental data from ref 4 Figure 1 demonstrates that such an expression faithfully describes the experiments down to 6 K, whereby the parameter values are $D_0 = 3.75$ s^{-1}, $D = 8.83 \times 10^4$ s^{-1}, and $\epsilon = 93.4$ K. For comparison, fits with $D_0 = 0$ and the Arrhenius expression used in ref 4 are also shown. Diffusivities larger than 0 at very low temperatures (≤1 K) have, for example, been observed for atom diffusion in body-centered tungsten.[10,11] Finite diffusivities at such low temperatures (<1 K) have been primarily associated with zero-point motion.[11]

To further corroborate the finding that no major corrections due to tunneling are required, atomistic simulations together with quantum-dynamical calculations for the translational motion of the oxygen atom were carried out. Molecular dynamics (MD) and Monte Carlo (MC) simulations were performed using CHARMM.[12] The initial ASW structure was generated as previously described.[13] Starting from a TIP3P[14] water box (31 × 31 × 50 Å^3), equilibrated at 300 K, the system was first quenched to 50 K, then equilibrated in the NpT ensemble, followed by further equilibration with NVT using periodic boundary conditions. A cutoff of 13 Å was applied to the nonbonded interactions. All production MD simulations were performed in the microcanonical (NVE) ensemble with a time step of 1 fs. For both simulation temperatures of 10 and 50 K, respectively, heating and equilibration runs were performed for 10 and 50 ps, respectively. At 10 K only a single production simulation was run for 900 ns due to the low mobility of the oxygen atom on the surface. Increasing the temperature to 50 K lead to much wider sampling, and 10 independent simulations, each 900 ns long, were run. Bonds involving hydrogen atoms were constrained using SHAKE.[15]

For determining the nonbonded parameters for oxygen, 34 clusters (from an equilibrium MD simulation at 50 K) consisting of 12 water molecules interacting with one oxygen atom were extracted, and total energies at the MP2/aug-cc-pVDZ level of theory using Gaussian09[16] were determined. Next, the oxygen atom van der Waals parameters $r_{\mathrm{min,O}}$ and ϵ_{O} were fitted using a simplex algorithm to best reproduce the target energies, which yielded $r_{\mathrm{min,O}} = 1.62$ Å and $\epsilon_{\mathrm{O}} = -0.518$ kcal/mol. This parametrization gives oxygen desorption energies of 2.15 kcal/mol (1082 K), in good agreement with values of 1380 K derived from temperature-programmed desorption experiments.[7]

Using this parametrization, the 2D free-energy surface $G(x, y)$ was determined from Monte Carlo (MC) simulations at 50 K on an equally spaced grid (31 × 31 Å^2). For each of the 961 grid points, 10^8 MC steps were run to determine the probability distribution $P(x, y)$ from which $G = -RT \ln(P)$ was determined. The interaction of the oxygen atom with the water surface is sufficiently strong to preclude exhaustive sampling of the entire $G(x, y)$ (only 60% of the grid is sampled). Therefore, the same MC simulations were repeated with the original ("orig") CHARMM36 parametrization for the oxygen atom. For this force field the oxygen desorption energy is reduced to ∼1 kcal/mol, which allows complete and exhaustive sampling of $G_{\mathrm{orig}}(x, y)$ due to the smaller desorption energy, which also lowers the intersite barrier. The two free-energy surfaces can be readily related for the grid points that are sufficiently sampled (60% of all grid points) with a correlation coefficient of 0.925, and hence the less sampled regions using the correct, present parametrization for the oxygen atom can be extrapolated from $G_{\mathrm{orig}}(x, y)$, as shown in Figure S2.

In addition, explicit MD simulations were carried out at 10 and 50 K using the refined nonbonded parameters for the oxygen atom. For 10 K the oxygen atom diffuses between neighboring minima for 900 ns; see Figure 2. Increasing the temperature to 50 K, the oxygen atom samples an extended path (length 62.4 Å (minima 1 to 8 and 17 to 26; see Figure 2A)) within 900 ns of explicit MD simulations. Hence, in translucent and diffuse clouds oxygen diffusion is expected to occur. The average value of the free-energy profile is indicated by the dashed red line, whereas the average barrier height (0.55 kcal/mol equivalent to 275 K) is the dashed green line above the average energy. As can be seen, many barriers along the path are below the average barrier height. At 50 K the average dwell time in a local minimum is ∼5 ns, which suggests facile diffusion at such temperatures on comparatively short time scales.

To explicitly address the question of whether quantum effects are relevant for oxygen diffusion, the 1D Schrödinger equation for the translational motion of the oxygen atom was solved for part of the free-energy profile from Figure 2 (minima 23, 24, and 25; see Figure 3). For comparison, classical MD simulations solving Newton's equations of motion were also carried out using the same free-energy profile. Parabolic walls were added at the outer boundaries to confine the motion of the oxygen atom.

For following the quantum-mechanical time evolution of the system, the time-dependent Schrödinger equation

$$i\hbar \frac{\partial}{\partial t}\Psi(x, t) = \hat{H}\Psi(x, t) \qquad (1)$$

was solved using the Crank−Nicholson (CN) method.[17] Here x is the position, t is time, $\hat{H}$ is the Hamiltonian, and $\Psi(x, t)$ is

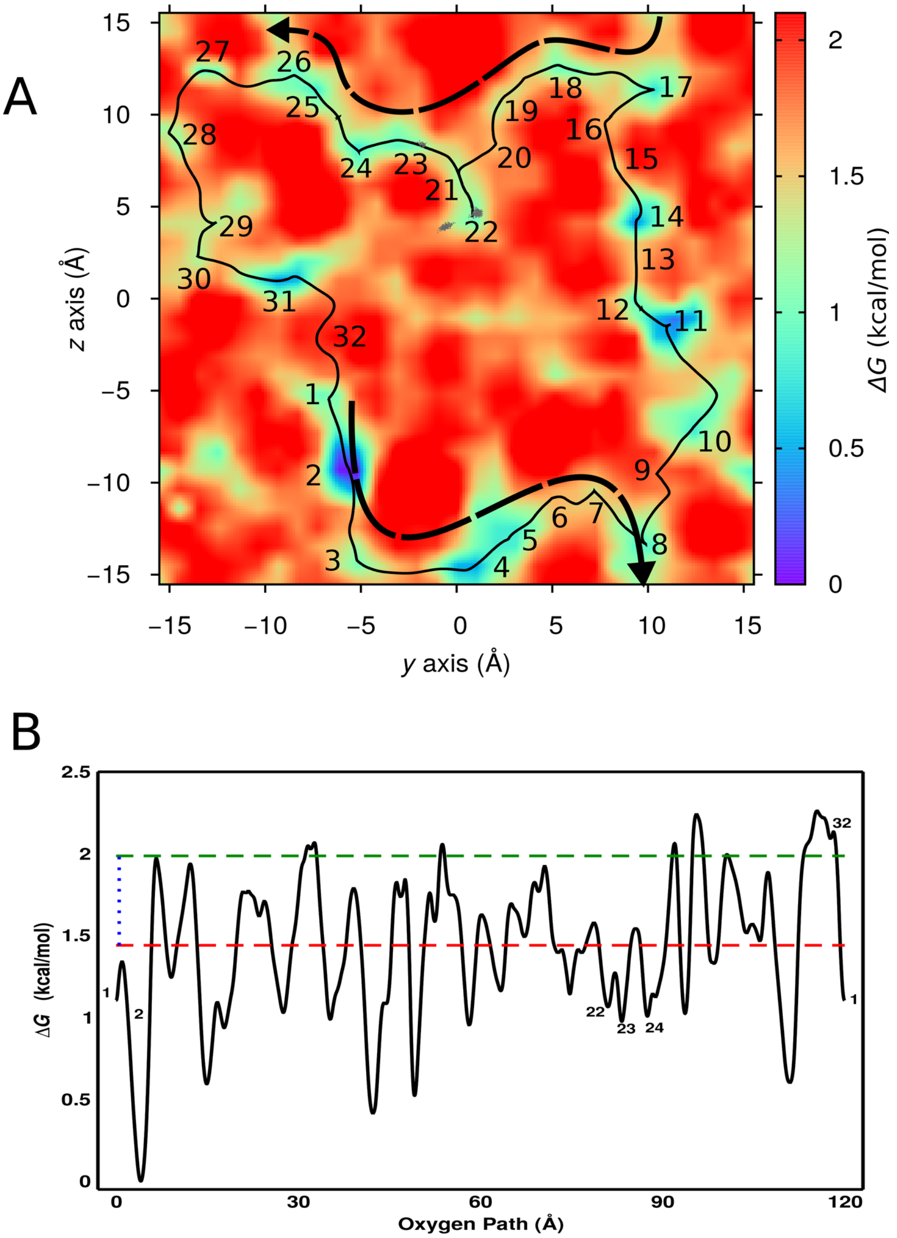

Figure 2. Typical oxygen diffusion path. (A) 2D free-energy surface $G(x, y)$. All of the minima of the free-energy surface are labeled from 1 to 32. They form a continuous closed loop of length 120 Å. The typical region visited during one single 500 ns MD simulation at 50 K is indicated by a dashed, arrowed line and includes minima 1 to 8 and (due to periodic boundaries) 17 to 26. Even for a 900 ns simulation at 10 K (gray dots) several minima (22 to 23) are sampled. (B) 1D projection of the closed loop from panel A with the path starting and ending at minimum number 1. The average free energy is indicated by the red dashed line, and the average barrier height (green dashed line) is 275 K (0.55 kcal/mol).

the wave function. The CN method is a second-order, symplectic method that conserves total energy and provides high accuracy. Simulations used a time step of δt = 0.2 fs and a grid spacing of $\delta x = 0.01a_0$. The original width of the ground-state wave function was 2.048 au, which is the width of the harmonic approximation to the potential around the minimum.

For the classical molecular dynamics simulations the initial position of all particles was $\delta(x - x_0)$, where x_0 = 2.279 Å is the minimum of the 1D energy profile in region 1 (see Figure 3) and velocities were sampled from a Maxwell−Boltzmann distribution at 50 K. The classical equations for motion were propagated with a 1 fs time step using a velocity Verlet algorithm.[18] Each dynamics was run for 5 ns and averaged over 10000 independent simulations. For solving the 1D time-dependent Schrödinger equation using the CN method, 1000 simulations were initialized according to a Maxwell−Boltzmann distribution at 50 K. For each time frame the amplitudes were Boltzmann-averaged to obtain the total probability distribution.

Both classical (panel C) and quantum simulations (panel D) reach a steady distribution after 10 (classical) and 20 ps (quantum), respectively, showing a slightly larger probability (10^{-3} vs 5×10^{-4} for region 3 and 10^{-2} vs 3×10^{-2} for region 2) if quantum effects are included. At the end (5 ns) of both simulations the probability remains highly localized in region 1,

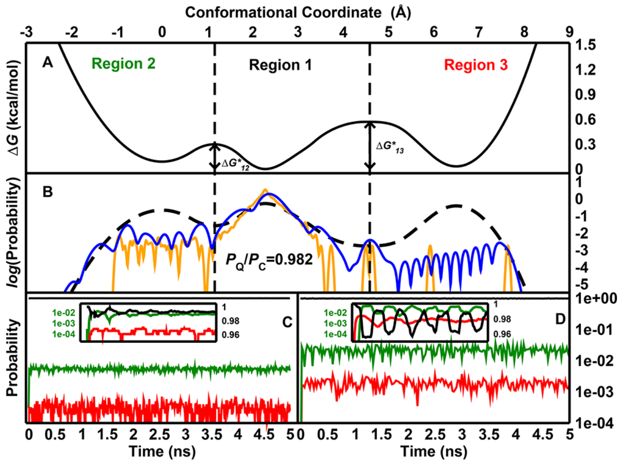

Figure 3. (A) Free-energy curve for the path between minima 23 and 25 (regions 2 (green), 1 (black), and 3 (red), respectively) from the oxygen diffusion path in Figure 2. This particular path is chosen because it is representative of the average barrier height (275 K) of the free-energy surface. The barrier heights between regions (1, 2) and (1, 3) are ΔG_{12} = 150 K and ΔG_{13} = 256 K, respectively. (B) Probability distribution after 5 ns of CN (blue) and classical MD simulations (orange) along with the equilibrium distribution (dashed black). The ratio of their amplitudes in region 1 is 0.98, indicating close agreement for quantum and classical dynamics on a time scale of 5 ns. Using an *NVE* ensemble, the equilibrium probability is not reached. (C,D) Probability distribution in regions 1 (black), 2 (green), and 3 (red) from panel A for classical MD (panel C, as number of particles per region) and CN (panel D, as wave packet density per region). Amplitudes are reported on a logarithmic scale (for linear scale, see Figure S3). Results in panel C are from classical *NVE* MD simulations of 10 000 oxygen atoms at 50 K. Results in panel D are from a quantum-mechanical simulation of a Boltzmann-averaged oxygen over 1000 simulations at 50 K. The insets in the panels show the results from the first 10 ps of simulation. The black scale refers to the black trace, whereas the green scale corresponds to the green and red traces.

with just a small portion able to overcome the barriers. This reflects the fact that the system is unable to reach thermal equilibrium at 50 K for both the potential and the free energy because no energy exchange with the environment can take place and only particles with sufficient initial velocity eventually overcome the barrier between the global minimum and the neighboring local minima. Hence the classical and quantum simulations are consistent with one another and suggest that tunneling plays a minor role. Remaining deviations from purely classical behavior, for example, a value of $D_0 \neq 0$ in the expression for the diffusion rate $D^* = D_0 + De^{-(\epsilon/T)^2}$, are likely to be related to zero-point motion.

Oxygen diffusion on a rough potential energy surface as provided by ASW allows for facile diffusion of the adsorbate down to temperatures relevant to interstellar chemistry. The parametrization for oxygen interacting with ASW used in this work correctly describes the average desorption energy of oxygen from water. Fitting the temperature dependence of the experimentally measured diffusion rates[4] to an expression that accounts for roughness of the underlying PES yields a typical scale of the roughness of $\epsilon \approx 100$ K, which compares with typical average barrier heights of $E_{\rm dif}$ = 275 K. Direct comparison of these two quantities should be done with care as they originate from two quite different analyses: ϵ is an effective roughness from a fit of experimental data sampling a large number of transitions and including the actual dynamics, whereas $E_{\rm dif}$ is an average barrier height experienced by the diffusing oxygen from a few tens of transitions (see Figure 2B). Furthermore, the morphologies of the ASW surfaces from experiments and in the simulations are likely to differ. Nevertheless, both analyses clearly establish the existence of surface roughness, and it is encouraging that the magnitudes of the two effective parameters, ϵ and $E_{\rm dif}$, characterizing the surface corrugation are within less than a factor of 3 given the differences in the systems investigated. Explicit quantum and classical simulations for the translational motion of the oxygen atom on the free-energy surface demonstrate that quantum and classical simulations on the 5 ns time scale agree well and tunneling does not play a role. This is particularly true when considering that rough surfaces tend to suppress tunneling effects.

The ratio of diffusional versus desorption barrier $E_{\rm dif}/E_{\rm des}$ = 275/1082 ≈ 0.3 found in the present work (from sampling an exemplary circular path) is somewhat lower than that recently proposed from temperature desorption experiments (0.55)[7] but similar to other typically used ratios of 0.3 to 0.4.[19] This ratio may depend on the surface morphology and change if longer simulations with more extensive sampling are carried out. Furthermore, the diffusion barrier height $E_{\rm dif}$ = 275 K is sufficiently low to yield comparatively rapid mobility at low temperatures. Such a barrier corresponds to $\sim 10^4$ hops per second (based on an Arrhenius dependence with a frequency factor of 10^{12} $\rm s^{-1}$)[7] and is consistent with values for $D \approx 10^4$ to 10^5 $\rm s^{-1}$ from Figure 1, which suggests that oxygen atoms under such conditions are able to sample appreciable parts of the available surface to eventually find reaction partners. Conversely, the desorption energy $E_{\rm des}$ = 1000 K is sufficiently high to prevent escape from the surface and leads to long residence times.

In conclusion, the analysis of experimental and simulation results shows that oxygen diffusion on ASW down to very low temperatures is possible and does not require quantum tunneling. This insight is of fundamental relevance for the formation of molecules including CO_2, water (minor pathway), and other molecules (e.g., OCOH from HCO or OCCHO from HCCO)[3] in laboratory experiments and on grains under conditions characteristic of the interstellar medium. The extension of such considerations to surfaces including graphite and silicon may provide further insight into chemical processing of grains in later stages of their development.

■ ASSOCIATED CONTENT

Ⓢ Supporting Information

The Supporting Information is available free of charge on the ACS Publications website at DOI: 10.1021/acs.jpclett.8b00328.

> Figure S1. Explicit diffusion path at 50 K. Figure S2. Additional information about the construction of the 2D free-energy surface for the parametrized model for oxygen interacting with water clusters. Figure S3. Data from Figure 3B on a linear *y* scale. (PDF)

■ AUTHOR INFORMATION

Corresponding Author

*E-mail: m.meuwly@unibas.ch.

ORCID

Oliver T. Unke: 0000-0001-7503-406X
Markus Meuwly: 0000-0001-7930-8806

Notes

The authors declare no competing financial interest.

ACKNOWLEDGMENTS

This work was supported by the Swiss National Science Foundation through grants 200021-117810 and the NCCR MUST. We are grateful to Prof. F. Dulieu for providing us with raw experimental data and Profs. F. Dulieu and A. G. G. M. Tielens for insightful discussions.

REFERENCES

(1) Tielens, A. G. G. M.; Hagen, W. Model Calculations of the Molecular Composition of Interstellar Grain Mantles. *Astron. Astrophys.* **1982**, *114*, 245–260.

(2) Ruffle, D.; Herbst, E. New models of interstellar gas-grain chemistry - III. Solid CO2. *Mon. Not. R. Astron. Soc.* **2001**, *324*, 1054–1062.

(3) Charnley, S. B.; Rodgers, S. D. In *Astrochemistry: Recent Successes and Current Challenges*; Lis, D. C., Blake, G. A., Herbst, E., Eds.; International Astronomical Union, 2006; pp 237–246.

(4) Minissale, M.; Congiu, E.; Baouche, S.; Chaabouni, H.; Moudens, A.; Dulieu, F.; Accolla, M.; Cazaux, S.; Manico, G.; Pirronello, V. Quantum Tunneling of Oxygen Atoms on Very Cold Surfaces. *Phys. Rev. Lett.* **2013**, *111*, 053201.

(5) Cuppen, H. M.; Ioppolo, S.; Romanzin, C.; Linnartz, H. Water formation at low temperatures by surface O-2 hydrogenation II: the reaction network. *Phys. Chem. Chem. Phys.* **2010**, *12*, 12077–12088.

(6) Cuppen, H. M.; Herbst, E. Simulation of the formation and morphology of ice mantles on interstellar grains. *Astrophys. J.* **2007**, *668*, 294–309.

(7) Minissale, M.; Congiu, E.; Dulieu, F. Direct measurement of desorption and diffusion energies of O and N atoms physisorbed on amorphous surfaces. *Astron. Astrophys.* **2016**, *585*, A146.

(8) Congiu, E.; Minissale, M.; Baouche, S.; Chaabouni, H.; Moudens, A.; Cazaux, S.; Manico, G.; Pirronello, V.; Dulieu, F. Efficient diffusive mechanisms of O atoms at very low temperatures on surfaces of astrophysical interest. *Faraday Discuss.* **2014**, *168*, 151–166.

(9) Zwanzig, R. Diffusion on a rough potential. *Proc. Natl. Acad. Sci. U. S. A.* **1988**, *85*, 2029.

(10) Dausinger, F.; Schultz, H. Long-range migration of self-interstitial atoms in tungsten. *Phys. Rev. Lett.* **1975**, *35*, 1773–1775.

(11) Swinburne, T. D.; Ma, P.-W.; Dudarev, S. L. Low temperature diffusivity of self-interstitial defects in tungsten. *New J. Phys.* **2017**, *19*, 073024.

(12) Brooks, B. R.; et al. CHARMM: The biomolecular simulation program. *J. Comput. Chem.* **2009**, *30*, 1545–1614.

(13) Lee, M. W.; Meuwly, M. Diffusion of atomic oxygen relevant to water formation in amorphous interstellar ices. *Faraday Discuss.* **2014**, *168*, 205–222.

(14) Jorgensen, W. L.; Chandrasekhar, J.; Madura, J. D.; Impey, R. W.; Klein, M. L. Comparison of Simple Potential Functions for Simulating Liquid Water. *J. Chem. Phys.* **1983**, *79*, 926–935.

(15) Ryckaert, J.-P.; Ciccotti, G.; Berendsen, H. J. C. Numerical integration of the cartesian equations of motion of a system with constraints: molecular dynamics of n-alkanes. *J. Comput. Phys.* **1977**, *23*, 327–341.

(16) Frisch, M. J.; et al. *Gaussian 09*, revision D.01; Gaussian, Inc.: Wallingford, CT, 2009.

(17) Crank, J.; Nicolson, P.; Hartree, D. R. A practical method for numerical evaluation of solutions of partial differential equations of the heat conduction type. *Math. Proc. Cambridge Philos. Soc.* **1947**, *43*, 50–67.

(18) Verlet, L. Computer "Experiments" on Classical Fluids. I. Thermodynamical Properties of Lennard-Jones Molecules. *Phys. Rev.* **1967**, *159*, 98–103.

(19) Karssemeijer, L. J.; Cuppen, H. M. Diffusion-desorption ratio of adsorbed CO and CO2 on water ice (Research Note). *Astron. Astrophys.* **2014**, *569*, A107.

DOI: 10.1021/acs.jpclett.8b00328
J. Phys. Chem. Lett. 2018, 9, 1822–1826

Molecular Oxygen Formation in Interstellar Ices Does Not Require Tunneling

Marco Pezzella, Oliver T. Unke, and Markus Meuwly*

Department of Chemistry, University of Basel,
Klingelbergstrasse 80, 4056 Basel, Switzerland

E-mail: m.meuwly@unibas.ch

Figure S1 reports an explicit diffusion path at 50 K. The supplementary information also provides additional information about the construction of the 2-dimensional free energy surface for the parametrized model for oxygen interacting with water clusters, see Figure S2. Furthermore, Figure S3 reports the data from Figure 3B in the main text on a linear $y-$scale.

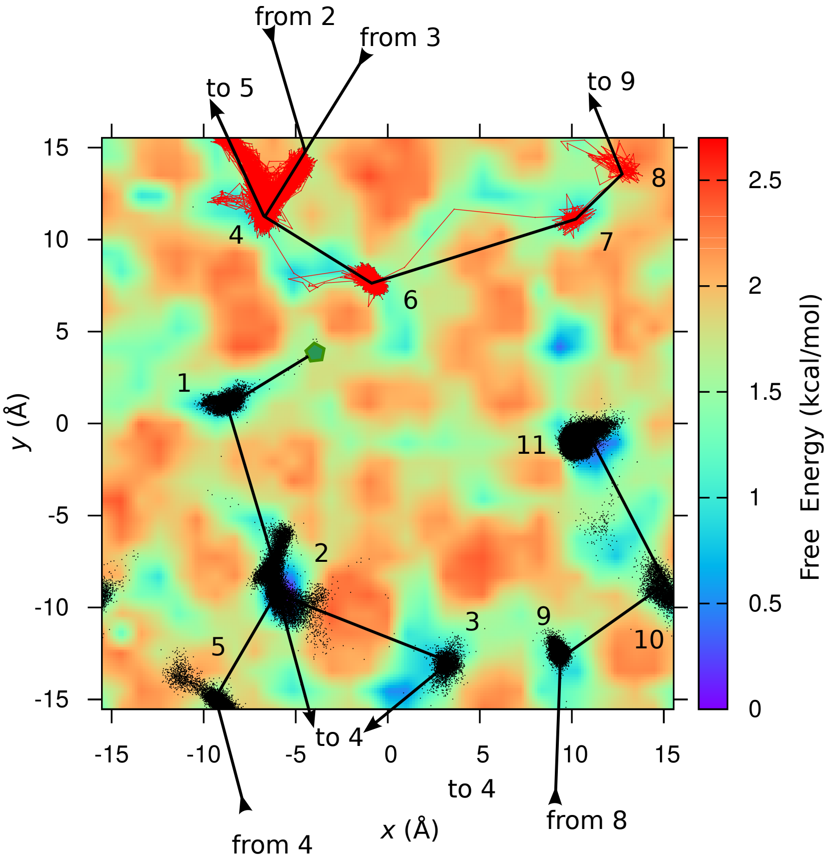

Figure S1: Trace (black dots) of one exemplary MD trajectory at 50 K projected onto the free energy surface at 50 K. The dynamics is characterized by rapid intrastate dynamics (red connecting lines) followed by jumps (thick black lines) between adsorption sites 10 Å or further away (see e.g. transitions 1 → 2 or 6 → 7). The overall path follows the sequence 1 (green symbol) → 2 → 3 → 4 → 5 → 2 → 4 → 6 → 7 → 8 → 9 → 10 → 11. A typical intrasite diffusivity is of the order of 20 to 30 Å^2/ns compared with 60 Å^2/ns from simulations of oxygen in bulk ASW.[1]

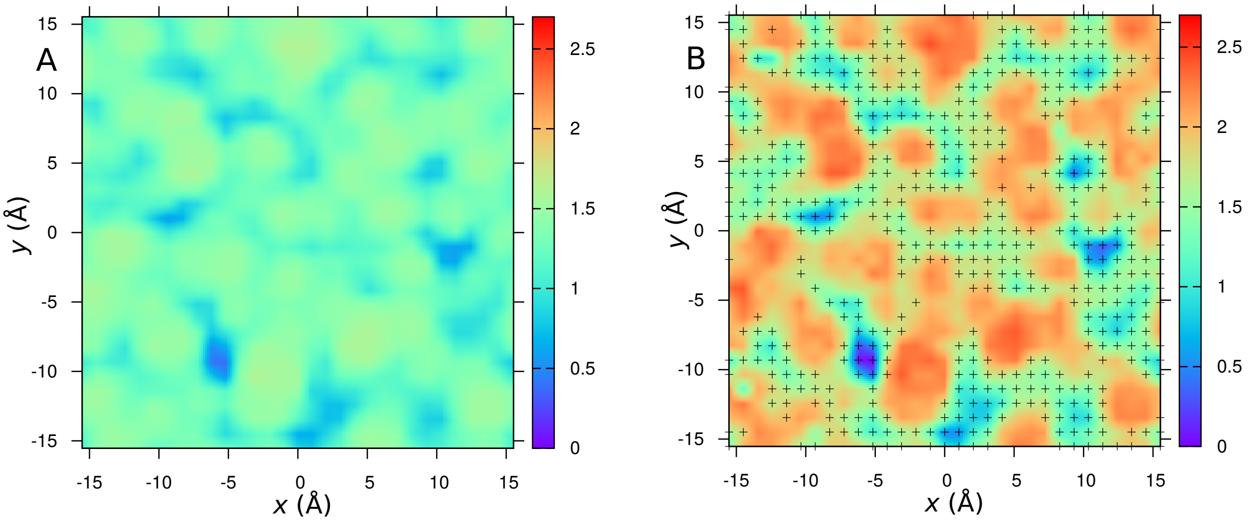

Figure S2: The free energy surface with the original CHARMM36 parametrization for the oxygen atom, panel A, allows complete sampling of $G_{\mathrm{orig}}(x, y)$. Contrary to that the new, modified parametrization precludes complete exploration of the surface, exploring only the 60 % of the grid with 4 millions points, due to the stronger interaction between the oxygen atom and the surface. Matching the sampled parts of $G_{\mathrm{orig}}(x, y)$ and $G_{\mathrm{mod}}(x, y)$ allows to extrapolate unsampled regions of $G_{\mathrm{mod}}(x, y)$. The sampled regions on $G_{\mathrm{mod}}(x, y)$ are indicated using black crosses (right panel).

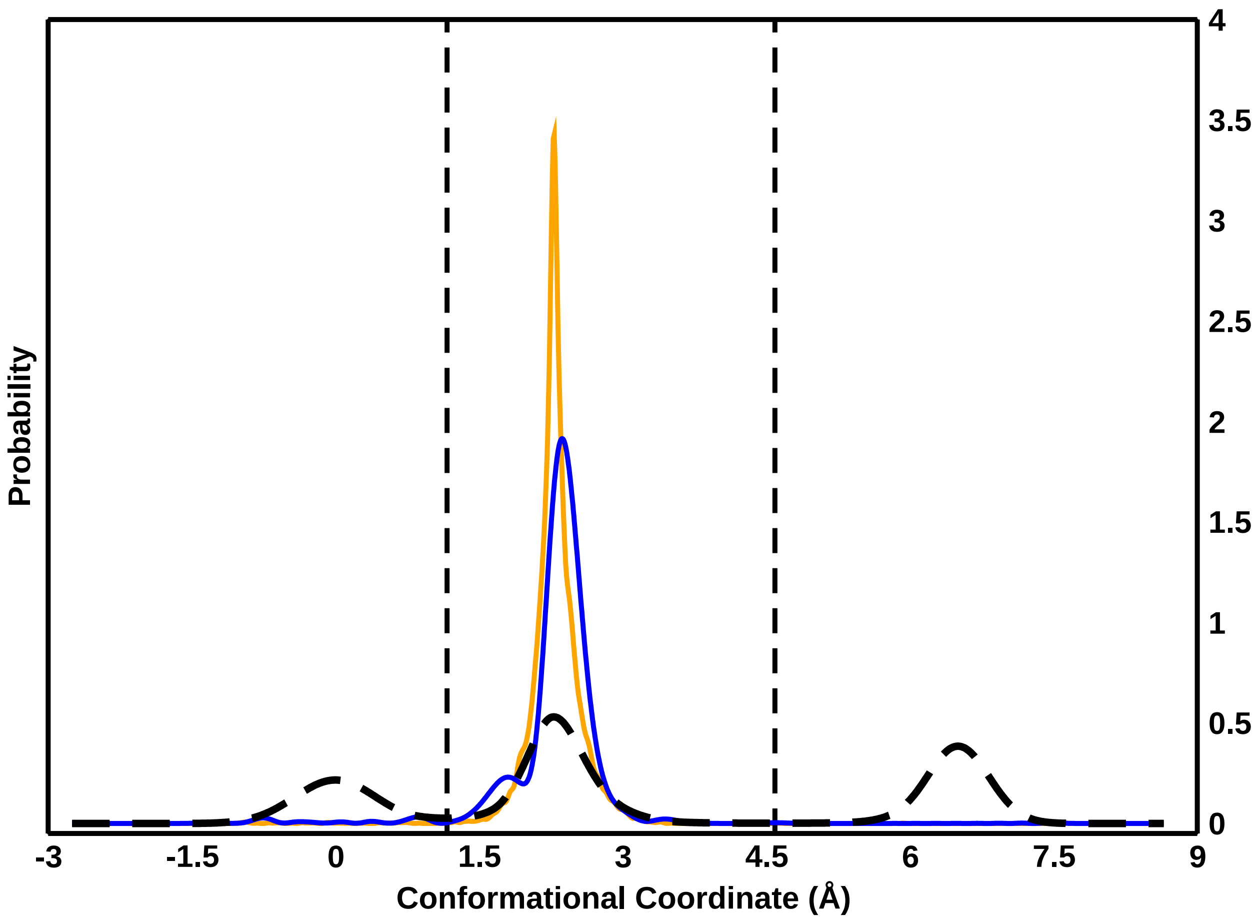

Figure S3: The equilibrium oxygen distribution (black dashed), and the distributions from the swarm-MD (orange) and Crank-Nicolson (blue) simulations from Figure 4 in the main manuscript on a linear $y-$scale. In a microcanonical ensemble, as employed here, the kinetic energy is not sufficient to reach thermal equilibrium.

References

(1) Lee, M. W.; Meuwly, M. Diffusion of atomic oxygen relevant to water formation in amorphous interstellar ices. *Faraday Discuss.* **2014**, *168*, 205–222.

2. O_2 formation in cold environments

In this chapter the recombination of two oxygen atoms forming the ground state $O_2(^3\Sigma_g^-)$ is studied both inside and on top of the ASW surface. Different aspects of the reactions are taken into exam: the efficiency of the reaction, the relaxation mechanism and the possibility that desorption mechanism could happen at ISM condition.

Different models of potentials are used for O_2 and H_2O. In case of the first, results from the Morse potential are compared with a more sophisticated RKHS potential based on the work from Ruedenberg[14]. The rigid TIP3P water is compared to flexible model to observe how the water flexibility influences the new formed molecule relaxation.

The lack of desorption and the slow relaxation are examined taking into account similar phenomena encountered in literature. At the end, an estimation of the relaxation time is achieved considering the glassy nature of the water matrix.

2.1. MS-ARMD

The study of chemical reaction through quantum chemistry methods is limited due to the high computational cost required and by the approximations introduced. The implementation of reactive FF can offer a fast and complete option for exploring the complete PES.

The empirical valence bond[15] and its multistate variant[16] are two options used for studying proton transfer in solution. The main drawbacks of these methods are the introduction of a dependence on the choice of the reaction coordinate and the prohibitive computational cost for reactions in which multiple paths are involved. Another possible way to study the reaction is to follow the reaction along the simulation time as implemented in the adiabatic reactive molecular dynamics (ARMD) methodology[17], even if energy conservation problems are observed for small molecular system.

Reactive simulations can be simulated with a rigorous energy conservation and made time independent with the introduction of the multisurface version of ARMD, known as MS-ARMD[18]. The total potential energy of the PES, $V_{\text{MS-ARMD}}$ is defined as function of the Cartesian coordinate, $\mathbf{x}$, the n PES involved in the process (V_i) and weights $w_i(\mathbf{x})$ between them:

$$V_{\text{MS-ARMD}}(\mathbf{x}) = \sum_{i=1}^{n} w_i(\mathbf{x}) V_i(\mathbf{x}) \tag{2.1}$$

The $w_i(\mathbf{x})$ are obtained by renormalizing the raw weights $w_{i,0}(\mathbf{x})$ calculated by exponential decay function depending on the lowest energy surface $V_{min}(\mathbf{x})$ and the user defined ΔV parameter:

$$w_i(\mathbf{x}) = \frac{w_{i,0}(\mathbf{x})}{\sum_j^n w_{j,0}(\mathbf{x})} \tag{2.2}$$

$$w_{i,0}(\mathbf{x}) = \exp\left(-\frac{V_i(\mathbf{x}) - V_{min}(\mathbf{x})}{\Delta V}\right) \tag{2.3}$$

Only those surfaces explicitly contribute to the adiabatic PES whose energy is few integer bigger than ΔV.

For describing the adiabatic barrier, Gaussian × polynomial (GAPO) functions are used for correctly mixing the two PES at the crossing point, accurately reproducing the trend. The energy correction due to the GAPOs ($\Delta V^{ij}_{\mathrm{GAPO},k}(\mathbf{x})$) is:

$$\Delta V^{ij}_{\mathrm{GAPO},k}(\mathbf{x}) = \exp\left(-\frac{\left(\Delta V_{i,j}(\mathbf{x}) - V^0_{ij,k}\right)^2}{\sigma^2_{ij,k}}\right) \times \sum_{l=0}^{m_{ij,k}} a_{ij,kl}\left(\Delta V_{i,j}(\mathbf{x}) - V^0_{ij,k}\right)^l \tag{2.4}$$

with $\Delta V_{i,j}(\mathbf{x})$ the difference in energy between the two reactive states, $V^0_{ij,k}$, $\sigma_{ij,k}$ and $a_{ij,kl}$ user defined parameters. The total energy becomes:

$$V_{\text{MS-ARMD}}(\mathbf{x}) = \sum_{i=1}^{n} w_i(\mathbf{x})V_i(\mathbf{x}) + \sum_{i=1}^{n-1}\sum_{j=i+1}^{n}\left(w_i(\mathbf{x}) + w_j(\mathbf{x})\right)\sum_{k=1}^{n_{ij}}\Delta V^{ij}_{\mathrm{GAPO},k}(\mathbf{x}) \tag{2.5}$$

This method is used to simulate the reaction between the unbound and bound O_2. In order to properly reproduce the *ab-initio* trend of the diatomic the monodimensional RKHS potential is implemented in the original version of MS-ARMD.

2.2. The KKY water model

The Kumagai, Kawamura and Yokokawa (KKY) water model[19] is a dedicated FF which consists of a series of two and three body terms. Different to other water models, it does not require the application of constraints to the intramolecular motions.

The model was developed for water and different ice polymorphs. Nonbonded interaction and intramolecular Morse stretching terms are calculated using a two body terms. The three body term is used for describing the HOH bend (E_{bend}) and has the following form:

$$E_{\mathrm{bend}} = 2f_{\mathrm{k}}k_1k_2 sin^2\left(\theta - \theta_{\mathrm{eq}}\right) \tag{2.6}$$

with

$$k_{1,2} = \frac{1}{e^{g_\mathrm{r}(r1,2-r\mathrm{m})} + 1} \tag{2.7}$$

$f_\mathrm{k} = 23.85$ kcal/mol, $g_\mathrm{r} = 1.96$ Å^{-1} and $r\mathrm{m} = 1.40$ Å are empirical parameters, θ is the angle at a given instant, $\theta_\mathrm{eq} = 99.5$ degrees is the equilibrium angle. Those parameters are the ones used in this thesis and obtained by Gupta and Meuwly[20].

In Table S1 of the article the normal modes frequencies are compared with experimental data, showing a good agreement within the two models.

The term $k_{1,2}$ indirectly introduce the O-H stretching dependence of the angle. It introduces forces acting along the perpendicular of the OH bond inside the molecular plane.

In the original publication[19] the model correctly reproduced crystal and structural parameters for ice I_h, ice II and ice IX in good agreement with the experimental values but failed to reproduce the compressibility of liquid water and ice I_h.

This model is used for studying behavior of small molecules under astrochemical conditions. A first application from Plattner and Meuwly[21] studied the CO vibration on both I_h and ASW, showing the complexity of the CO vibrational progression due to the environment interaction. Lee and Meuwly[22] used free energy techniques to estimate the diffusion barrier and hopping rate inside the ASW at 50 K, 100 K, 200 K, finding a barrier height of 1.8 kcal/mol and hopping rate of 15.5 ns^{-1}.

The importance of using flexible water is in the coupling that can occur between the water bending and O_2 stretching. This effect is shown to speed up the relaxation process of the recombined O_2 by a factor of 4 in respect to the simulations where the TIP3P water is used.

2.3. Vibrational relaxation

In the diatomic recombination, it is expected that the excess of energy in vibrational methods would be transferred to the translational and rotational degrees of freedom of the newly formed O_2 and to the ASW matrix, which acts as thermal bath that removes the excess of energy.

The relaxation from the O_2 ($\nu \sim 35$) to the ground state occurs via a series of single quantum transitions of the kind $O_2(\nu = n) \longrightarrow O_2(\nu = n-1)$, via matrix coupling or quantum fluorescence. Multiple quantum transitions are excluded in the process as they are forbidden by dipole selection rules.

However, during the reactive events in this and in the next chapter, a very slow relaxation is observed during the simulations. A fast step is observed within the first nanosecond of simulations followed by a slow process. Complete relaxation is too long to be observed during the simulation time (arriving at $\nu = 15$ at 100 ns of simulation). After testing the validity of the FF, the decoupling between O_2 and ASW matrix is hypothesized.

This hypothesis is supported by previous works in literature. Chang and Edwing[23] explored the vibrational relaxation of CO on top a NaCl(100) surface around 55 K. The decoupling between the vibrational modes of CO and NaCl phonon modes is of the order of 1900 cm^{-1} ($\nu_{\text{CO}} \sim 2100$ cm^{-1} and $\nu_{\text{NaCl}} \sim 223$ cm^{-1}) and the complete relaxation is observed after $10^{-4} - 10^{-3}$ s. Corcelli and Tully[24] observed that the vibrational energy relaxation rates for the diatomics are exponential and they decrease as a function of the vibrational level. As n decreases the energy gap for the $n \rightarrow n-1$ transition increases, with a possible explanation found in the difficulty for the excess of energy to be dissipated by lower order phonon process in the ASW surface.

The relaxation process can be properly fitted using a *stretched exponential function*. This expression is of particular importance for the relaxation of glassy materials at low temperatures[25]. The use of stretched exponential function is justified by the glassy nature of ASW and on the fact that vibrational excited O_2 acts as a source of excitation on top of it.

$$r_{OO}(t) = r_{t_0} \exp\left[-\left(\frac{t}{\tau}\right)^{\beta}\right] + r_{eq} \tag{2.8}$$

with $r_{t_0} = r_{OO}(t=0)$ is the relaxing quantity at the beginning of the observation, τ is the characteristic time in which the relaxation takes place, $r_{eq} = 1.2075$ Å is the oxygen-oxygen equilibrium distance and β is the stretching exponent with the condition of $0 < \beta < 1$.

The value of β was presented by Phillips[26] , and it was based on the diffusion of the excitation to randomly distributed particles. In case $\beta \rightarrow 1$ the particle distribution is constant and time independent and the relaxation recovers the limit of an exponential relaxation, otherwise the stretched relaxation is obtained. This value can be expressed as a function of the effective dimensional (d^*) of process in exam:

$$\beta = \frac{d^*}{d^* + 2} \tag{2.9}$$

d^* is both dependent on the dimensionality itself (d) and on the fraction of channels that play a role in the relaxation (f) with the following formulation: $d^* = fd$. For surface relaxation $\beta \sim 0.15$ while in bulk phase is found to be $\beta \sim 0.20$. Assuming that the same fraction of active channel is active in both environments, it is found that in bulk phase $d = 3$, while on top of the surface $d = 2$. Full relaxation is estimated to take place around ~ 200 ns .

Open Access Article. Published on 26 February 2019. Downloaded on 6/6/2019 10:53:06 AM.
This article is licensed under a Creative Commons Attribution-NonCommercial 3.0 Unported Licence.

PCCP

PAPER

View Article Online
View Journal | View Issue

Cite this: *Phys. Chem. Chem. Phys.*, 2019, **21**, 6247

Received 6th December 2018,
Accepted 15th February 2019

DOI: 10.1039/c8cp07474g

rsc.li/pccp

O_2 formation in cold environments†

Marco Pezzella and Markus Meuwly *

The diffusional dynamics of atomic oxygen in and on amorphous solid water (ASW) to form molecular oxygen is characterized. Reactive molecular dynamics simulations to study bond breaking and bond formation show that vibrational relaxation of the highly excited diatomic occurs on the 10 ns to 100 ns time scale. The relaxation process is highly nonexponential and can be characterized by a stretched exponential decay reminiscent of the dynamics of glasses. The stretched exponents range from $\beta = 0.15$ for relaxation on the surface to $\beta = 0.21$ for the dynamics in bulk. It is also found that coupling of the O_2 relaxation to the internal water modes occurs which speeds up the vibrational relaxation by a factor of 4. Extrapolation of the stretched exponential decay to 1 μs yields a final vibrational quantum number $v = 2$ for $O_2(X^3\Sigma_g^-)$, consistent with experimental results from photolysis of SO_2 on ASW at 193 nm which find $v \leq 3$. Desorption energies of water from the surface range from 1.5 to 2.0 kcal mol^{-1} compared with 1.8 kcal mol^{-1} found from experiment, depending on whether the water molecules are flexible or not.

1 Introduction

The mobility of atomic and molecular species on solid surfaces is a primary driver for surface-induced chemistry at low temperatures. It has been found from experiments[1,2] and atomistic simulations[3,4] that H and O atoms can diffuse on amorphous water surfaces down to low temperatures (~10 K). This is relevant for the possibility to form diatomic or larger molecules (such as O_2, O_3 or CO_2) in laboratory experiments[2] and may also play a role for the conditions in interstellar space.[5–7] If other atomic species than hydrogen (such as N, C, or O) are able to diffuse on cold surfaces, the range of molecules that can be formed by diffusion and aggregation is considerably expanded. Given the very long processing times (~years or longer) that are available in translucent, diffuse and dense molecular clouds,[5,8] the accessible chemical space from such reaction pathways may be affected appreciably.

Molecular oxygen is an important tracer for characterizing the physical properties of star forming regions and molecular clouds and is implicated in various chemical processes leading to diverse chemical compositions in the interstellar space. Molecular oxygen in interstellar clouds was directly observed in the ρOphiuchi cloud using submillimeter wave spectroscopy.[9] Understanding of the formation and ensuing concentration[10] of O_2 is relevant for better characterizing the evolution of stellar clouds and their chemical composition.

In interstellar clouds, dust provides a suitable substrate for deposition and chemical synthesis of a variety of small molecules in a bottom-up fashion. Due to the low temperatures (10 K to 50 K),[5,8] residence times are long despite the small barriers (~1 to 2 kcal mol^{-1})[11,12] for desorption and migration which also allows reactions to occur. In laboratory experiments with amorphous solid water as the substrate, deposition of oxygen (O) and O_2 leads to ozone formation at 10 K.[13,14] These experiments suggest that using pure oxygen species, only two reactions are relevant: $O + O \rightarrow O_2$ and $O + O_2 \rightarrow O_3$.[2] In the experiments atomic oxygen ($O(^3P)$) was generated from dissociating O_2 through a microwave discharge and it was verified that all participating species are in their ground electronic state. In modeling interstellar processes, the $O + O \rightarrow O_2$ channel is sometimes included[5] and sometimes not.[15] Another, and probably the predominant,[16,17] O_2-formation reaction is $O + OH \rightarrow O_2 + H$. A more exhaustive list of O_2-formation reactions, including $O + OH \rightarrow O_2 + H$ in the gas phase[18] or on the surface of grains,[19] can be found in the KIDA database.[20]

It has been previously shown by experiment and simulations that migration of atomic species, such as oxygen, in ASW is readily possible on the sub-microsecond time scale over distances of several ten Angstroms.[2,4] Similarly, oxygen atom diffusion in Neon matrices at temperatures as low as 4 K has recently been established.[21] Diffusing oxygen atoms have also been implicated in the formation of CO_2 through $O + CO \rightarrow CO_2$.[22–24] This pathway for the formation of molecular species from adsorbates is generally known as the Langmuir–Hinshelwood mechanism.[25]

In laboratory experiments using amorphous solid water, formation of ground state $^3\Sigma_g^-$ (from $OH + O(^3P)$ with $\Delta H = -68$ kJ mol^{-1}) and excited state $^1\Delta_g$ O_2 (from $OH + O(^3P)$ with $\Delta H = 26$ kJ mol^{-1})

Department of Chemistry, University of Basel, Klingelbergstrasse 80, CH-4056 Basel, Switzerland. E-mail: m.meuwly@unibas.ch

† Electronic supplementary information (ESI) available. See DOI: 10.1039/c8cp07474g

Open Access Article. Published on 26 February 2019. Downloaded on 6/6/2019 10:53:06 AM.
This article is licensed under a Creative Commons Attribution-NonCommercial 3.0 Unported Licence.

was found following electronic excitation of the ASW with 157 nm irradiation at 90 K.[17] This process for O_2 formation follows a non-equilibrium route, involves higher electronic states and differs from the processes considered in temperature-programmed desorption experiments.[2] The study of SO_2 photolysis at 193 nm adsorbed on ASW yields $O_2(^3\Sigma_g^-)$ from recombination of $O(^3P) + O(^3P)$ with $\Delta H = -498$ kJ mol^{-1}.[17] Furthermore, a model for formation of O_2 following electronic excitation of ice by fast ions, low-energy electrons, and UV photons at low temperatures was presented.[26] In this model trapped $O(^3P)$ is the principal species considered for formation of O_2 at low doses. This route for O_2 formation is also implicated in the atmospheres of the icy moons of Jupiter and in the rings of Saturn, where molecular oxygen has been detected as a result of the decomposition of ice by energetic ions and electrons or by UV photon-induced production from ice.

In the present work the dynamics of O_2 formation in and on amorphous solid water (ASW) from collision of two $O(^3P)$ is studied. The main questions considered are the possibility for formation and stabilization, the likely formation time scales, the vibrational relaxation of highly excited O_2 following recombination, the desorption of molecular oxygen following a Langmuir–Hinshelwood mechanism and the energy transfer between the energized molecule and the surrounding water matrix. After presenting the methods, atomic oxygen recombination within and on the surface of an ice grain is considered and analyzed. Then, the desorption dynamics from the oxygen is considered.

2 Methods

2.1 Molecular dynamics simulations

All reactive MD simulations are carried out using CHARMM[27] with MS-ARMD[28–30] and the Leap Frog integrator with a time step of $\Delta t = 0.1$ fs. Such a short time step is required due to the high vibrational excitation upon oxygen–oxygen recombination and also in simulations with flexible water (*vide infra*). The simulation system is a cubic box with dimensions $(31\ \text{Å})^3$ with periodic boundary conditions and the nonbonded cutoff is 14 Å. The box size along the z-axis is elongated by 20 Å to allow for surface desorption of the O and O_2 adsorbate. Initial velocities are drawn from a Maxwell–Boltzmann distribution at 50 K. All simulations are initialized as follows: a minimization of 100 steps using the steepest descent method is followed by 10 ps heating, where the temperature is increased by 10 K every ps and then relaxed for the last 5 ps, and 50 ps equilibration dynamics with rescaling of the temperatures every 2.5 ps. Then, the following different types of simulations are considered: the (rigid) TIP3P[31] or the (flexible) KKY[32,33] water model are combined with either a reproducing kernel Hilbert space (RKHS) or a Morse representation of the reactive O–O potential (*vide infra*) to follow the recombination and relaxation dynamics.

Oxygen (O_2) formation from collision of two oxygen atoms is studied by using reactive MD which requires two potential energy surfaces, one for the unbound state (O + O), and a second one for bound O_2. MS-ARMD then handles the transition between the two states.[28] Only the state with the lowest energy is propagated in the simulations except for configurations for which the energy difference between the lowest and next higher-energy states is within ΔV for which mixing of the two (or multiple) states occurs. In those cases the total energy for each configuration $\mathbf{x}$ is the weighted sum of the involved states:

$$V_{\text{MRMD}}(\mathbf{x}) = \sum_{i=1}^{n} w_i(\mathbf{x}) V_i(\mathbf{x}) \tag{1}$$

where V_{MRMD} is the total energy surface, $w_i(\mathbf{x})$ is the weight of the ith state with energy V_i. The weight

$$w_i(\mathbf{x}) = \frac{w_{i,0}(\mathbf{x})}{\sum_{j=1}^{n} w_{j,0}(\mathbf{x})} \tag{2}$$

is calculated by re-normalizing the raw weights $w_{i,0}$, using an exponential decay function of the energy difference between the minimum $v_{\min}$ and the ith surface.

$$w_{i,0}(\mathbf{x}) = \exp\left(\frac{V_i(\mathbf{x}) - V_{\min}(\mathbf{x})}{\Delta V}\right) \tag{3}$$

In this work two states are used for the dynamics: the unbound state, described by two isolated oxygen atoms which interact through nonbonded interactions with a charge of zero and van der Waals parameters $\sigma = 1.7$ Å and $\varepsilon = 0.12$ kcal mol^{-1}, as parametrized in the CHARMM36 force field[34] and the bound O_2 in its ground electronic state $(^3\Sigma_g^-)$ for which accurate MRCISD + Q calculations are available.[35] These calculations employed the cc-pCVQZ basis set and the 12 electrons in the last 8 orbitals, including core-valence and relativistic contributions from the lower electronic states, were correlated.[35] The energies are represented using a reproducing kernel Hilbert space (RKHS) approach[36,37] or they were fitted to a Morse potential $V(r) = D_e(1 - e^{-\beta(r-r_e)})^2$. The parameters from a least-squares fit are $D_e = 123.1$ kcal mol^{-1}, $r_{eq} = 1.2075$ Å, and $\beta = 2.68673$ Å^{-1} for the well depth, equilibrium separation and steepness parameters, respectively. For the simulations using a RKHS representation the MRMD module in CHARMM was suitably modified.

For water two models are considered in the present work. One is the standard transferable interaction potential 3 points (TIP3P) water model[31] which is rigid. In order to study energy transfer between the highly excited oxygen molecule and the internal water degrees of freedom a flexible water model, a modified Kumagai, Kawamura and Yokokawa (KKY) model was used as well.[32,33] This model has also been used for studies of ASW in the past.[3,33] The functional form of the KKY model involves a stretching term

$$E_{\text{str}} = D_e\left(1 - e^{-\beta(r-r_{eq})}\right) - D_e \tag{4}$$

with $D_e = 75.037$ kcal mol^{-1}, $r_{eq} = 0.957$ Å, and $\beta = 2.74$ Å^{-1}. The bending potential is

$$E_{\text{bend}} = 2f_k\sqrt{k_1k_2}\sin^2(\theta - \theta_{eq}) \tag{5}$$

This journal is © the Owner Societies 2019

Open Access Article. Published on 26 February 2019. Downloaded on 6/6/2019 10:53:06 AM.
This article is licensed under a Creative Commons Attribution-NonCommercial 3.0 Unported Licence.

with

$$k_i = \frac{1}{e^{g_r(r_i - r_m)} + 1} \tag{6}$$

where θ_{eq} = 99.50°, r_i is one of the O–H bond distances and g_r = 6.99 Å^{-1} and r_m = 1.402 Å are original force field parameters and f_k = 0.11 J is a re-parametrized bending parameter, fitted to match the experimental bending frequency (see Table S1, ESI†).[33]

The ASW is prepared by annealing liquid water from 300 K to 50 K for a total simulation time of 10 ns. The final density (1.01 g cm^{-3}) of the system is compatible with what is expected for high density amorphous solid water.[38] To study O_2 formation within ASW, a cavity with volume ~1000 Å^3 is created by removing 15 water molecules. Then, the system is minimized and equilibrated and further relaxed by running a 1 ns equilibrium simulation at 50 K. This leads to one main cavity with a volume of 583 Å^3 and several smaller cavities with volumes ranging from 30 to 100 Å^3. The cavity volumes were determined from GHECOM.[39] No further deformation is observed after this preparation.

3 Results

In the following, the results are discussed separately for formation of O_2 in an inside ASW-cavity and for recombination at the surface.

3.1 Recombination in the cavity

Initial conditions for O_2-formation were generated from a 500 ps equilibrium MD simulation at 50 K with the two oxygen atoms in the same internal cavity as illustrated in Fig. 1. From this simulation, 1000 structures were chosen to initiate MS-ARMD simulations. The initial distribution of oxygen–oxygen separations (see Fig. 2) has distinct maxima at 3.4 Å, 7.0 Å, and 10.0 Å covering a wide range of initial conditions. The oxygen atoms are almost thermalized, with a kinetic temperature of 70 K compared with 50 K of the surrounding water lattice, although the meaning of temperature for a diatomic molecule is somewhat debatable.

All 1000 rebinding simulations are run for 100 ps and 16 of them are extended out to 5 ns to better characterize the relaxation process. The fraction of O_2-forming simulations is 79.3% within 100 ps with half of them forming O_2 within 20 ps. The whole range of initial separations (between 3.4 Å and ~13 Å) leads to formation of O_2, see red distribution in Fig. 2. Typical O_2-formation curves (black, red, blue, indigo) are reported in Fig. 3 whereas for the green trace no molecular oxygen is formed on the 100 ps time scale. The red trace shows that O_2 can also be formed transiently (at 40 ps), break up, reform and stabilize at a later stage. The overall distribution of the O_2-formation times is strongly peaked at short times with an extended tail, see top panel of Fig. 3.

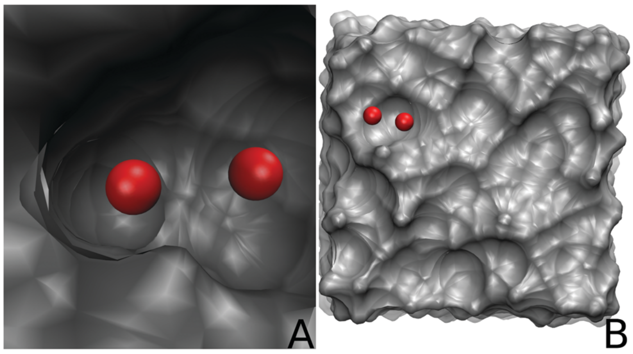

Fig. 1 Two physical conditions in which O_2 formation is studied: panel A shows two oxygen atoms (red) trapped inside a cavity of the ASW (grey); in panel B shows the two on top of the water surface.

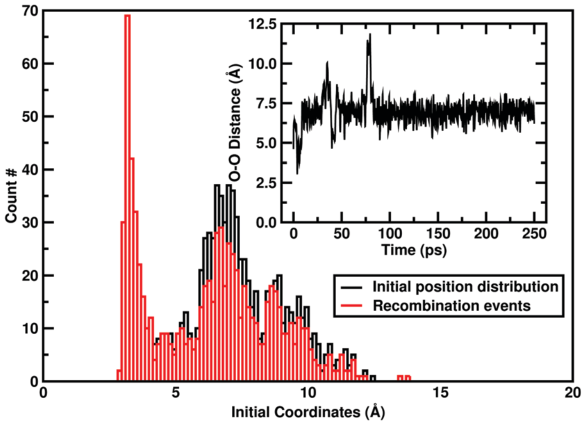

Fig. 2 Initial distribution of the oxygen–oxygen separation $P(r)$ at the beginning of the rebinding simulations using [TIP3P/RKHS]. $P(r)$ has three maxima at ~3.4 Å (the minimum of the O–O van der Waals complex), at 7.0 Å and at 10.0 Å. The total distribution (black) is compared with the one for initial conditions that lead to rebinding (red, 793 events on the 100 ps time scale). The inset shows the time series for the oxygen–oxygen distance $r(t)$ for one sample trajectory and confirms that all distances in $P(r)$ can be sampled even for one single trajectory.

Because rebinding of the two oxygen atoms leads to the liberation of the O_2 binding energy, it is expected that the kinetic temperature in the system increases. This is illustrated for one particular trajectory in Fig. 3 bottom panel. The lower panel in Fig. 3A reports the O_2 distance as a function of simulation time for one specific trajectory. At t = 23 ps a short encounter of the two oxygen atoms occurs which, however, does not stabilize O_2. Only after 55 ps molecular O_2 forms. Concomitantly, the kinetic energy and the temperature increase significantly, as is shown in Fig. 3B. This also leads to a marked temperature increase in the overall system from 50 K to >60 K.

Due to the weak coupling between the O_2 stretch and the phonons of the solid water matrix, vibrational relaxation of the diatomic is slow. In order to quantify this, 16 trajectories using [TIP3P/RKHS] were continued out to ~5 ns, see Fig. S2A (ESI†). Relaxation times were estimated by fitting the time dependent oxygen–oxygen separation $r_{OO}(t)$ to a sum of exponentials

$$r_{OO}(t) = \sum_{i=1}^{2} a_i \exp(-t/\tau_i) + r_0 \tag{7}$$

or to a stretched exponential

$$r_{OO}(t) = a \exp(-(t/\tau)^{\beta}) + r_0 \tag{8}$$

Open Access Article. Published on 26 February 2019. Downloaded on 6/6/2019 10:53:06 AM.
This article is licensed under a Creative Commons Attribution-NonCommercial 3.0 Unported Licence.

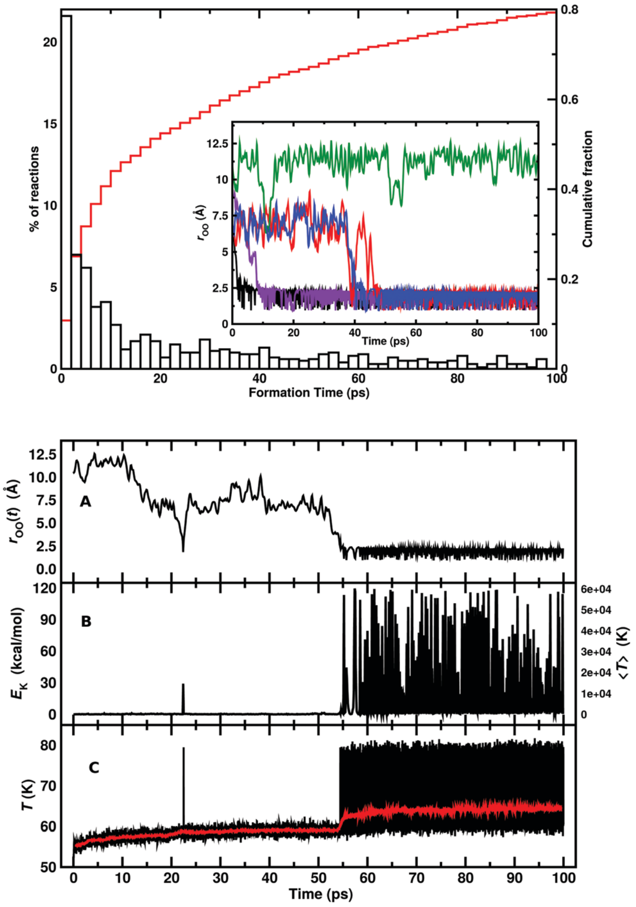

Fig. 3 Top: Histogram $P(\tau)$ of the formation times for the 793 reactive simulations; 40% react within the first 20 ps and the cumulative fraction is shown as the red line. Several time series $r_{OO}(t)$ are shown in the inset. In black and indigo two examples of a reaction within the first 20 ps, a late reaction (around 40 ps, blue), and a simulation where dissociation occurs soon after O_2 recombination (red) and in green a simulation where the atoms remain in the unbound state. Bottom: Interatomic distance (panel A), O_2 kinetic energy (panel B) and temperature profiles for water (red trace) and the overall system (black trace, panel C) for one recombination process. At t = 23 ps a nonproductive collision occurs and stabilization of O_2 starts after $t > 55$ ps. In panel B the right hand side y-axis reports the temperature associated with the kinetic energy of O_2.

with r_0 = 1.2075 Å, which is the O_2 equilibrium separation. Using stretched exponentials is probably more meaningful in the present context as such a dependence has been found to be particularly suitable to describe the relaxation of glasses[40] and for ligand rebinding to proteins[41] both of which are characterized by distributed barriers. In the present case (see Table 1) it is also found that the quality of the fit improves when one stretched exponential function is used compared to a fit to two exponentials. Considering one particular trajectory, the exponential decays involve a rapid decay τ_1 = 0.5 ns and a longer relaxation τ_2 = 14.6 ns whereas one stretched exponential leads to τ^{SE} = 1.4 ns with β = 0.21. The average long-time relaxation for the 16 trajectories is τ_2 = 15 ± 0.5 ns, see Fig. S2A (ESI†).

Upon O_2 formation the binding energy released will be partially converted into heat and dissipates through the ASW.

Table 1 Parameters and quality for fitting the O_2 vibrational relaxation to exponential (first line), one stretched exponential (second line) using eqn (7) and (8), respectively. The force fields (O_2 potential and water) with which the simulations were run are also indicated

Region	FF	a_1 (Å)	a_2 (Å)	τ_1 (ns)	τ_2 (ns)	β	RMSD (Å)
Inside	[TIP3P/RKHS]	0.28	0.38	0.5	14.6	—	3.638×10^{-3}
		1.38	—	1.4	—	0.207	6.546×10^{-5}
Surface	[TIP3P/RKHS]	0.35	0.31	1.1	83.4	—	9.154×10^{-3}
		1.08	—	1.1	—	0.144	2.032×10^{-4}
Surface	[KKY/RKHS]	0.27	0.34	0.7	20.7	—	2.156×10^{-3}
		1.12	—	0.9	—	0.182	3.082×10^{-4}
Surface	[TIP3P/Morse]	0.29	0.25	3.2	206.9	—	3.223×10^{-2}
		1.08	—	1.3	—	0.139	4.680×10^{-4}

To quantify this, the averaged kinetic energy of all water molecules projected along the z-direction is averaged on a (x, y)-grid with voxels 1 × 1 × 30 Å^3 (*i.e.* a column of height 30 Å and (x, y)-base 1 × 1 Å^2). The average kinetic energy of all water atoms in a single column is calculated, and averaged over 8 independent trajectories for times 10 ps before the recombination (at t = 0), *i.e.* for $-10 < t < 0$. Recombination was considered to have occurred for $r_{OO} < 2.5$ Å. The corresponding heat map is shown in Fig. 4A. The low energy region (blue) in the center of the chart corresponds to the cavity region where fewer water molecules are located along the z-direction.

A similar heat map was generated for the time $0 < t < 10$ ps, *i.e.* after recombination, see Fig. 4B and the difference map is shown in Fig. 4C. Heating of the ASW molecules around the recombination region is found to occur in a range of ~8 Å on the 10 ps time scale. Furthermore, energy flow is anisotropic due to the amorphous nature of the water matrix. Fig. 4D shows an ensemble average over 10 ps and 8 trajectories for a situation in which the two oxygen atoms are separated by an initial distance of 5 Å and are not allowed to recombine, *i.e.* MS-ARMD was disabled and the two oxygen atoms only interact through van der Waals interactions. The distribution of the kinetic energy in Fig. 4A and D are comparable and differ substantially from panel B.

3.2 O_2 formation: surface reaction

Atomic oxygen recombination on the surface of ASW is probably even more relevant under astrophysical conditions. There are two typical scenarios: the Langmuir–Hinshelwood (LH)[42,43] mechanism whereby the two reacting species are in thermal equilibrium with the environment before they react or the Eley–Rideal (ER)[44] mechanism for which a thermalized, surface-adsorbed reactant collides with an impinging, non-thermalized partner. The scenario explored here is the LH mechanism.

For these simulations, one of the oxygen atoms is initially localized (but unconstrained) in a surface cavity sufficiently deep to avoid spontaneous desorption for the present simulations and the second oxygen atom diffuses freely on the surface. Altogether, one 110 ns [Morse/TIP3], one 25 ns [KKY/RKHS], and one 10.5 ns [RKHS/TIP3] simulation were initially run and analyzed. The relaxation of the O–O bond length for the [Morse/TIP3] simulation is shown in Fig. 5 and Fig. S2, S3 (ESI†). Relaxation is characterized by a rapid initial phase during which ~50% or

Open Access Article. Published on 26 February 2019. Downloaded on 6/6/2019 10:53:06 AM.
This article is licensed under a Creative Commons Attribution-NonCommercial 3.0 Unported Licence.

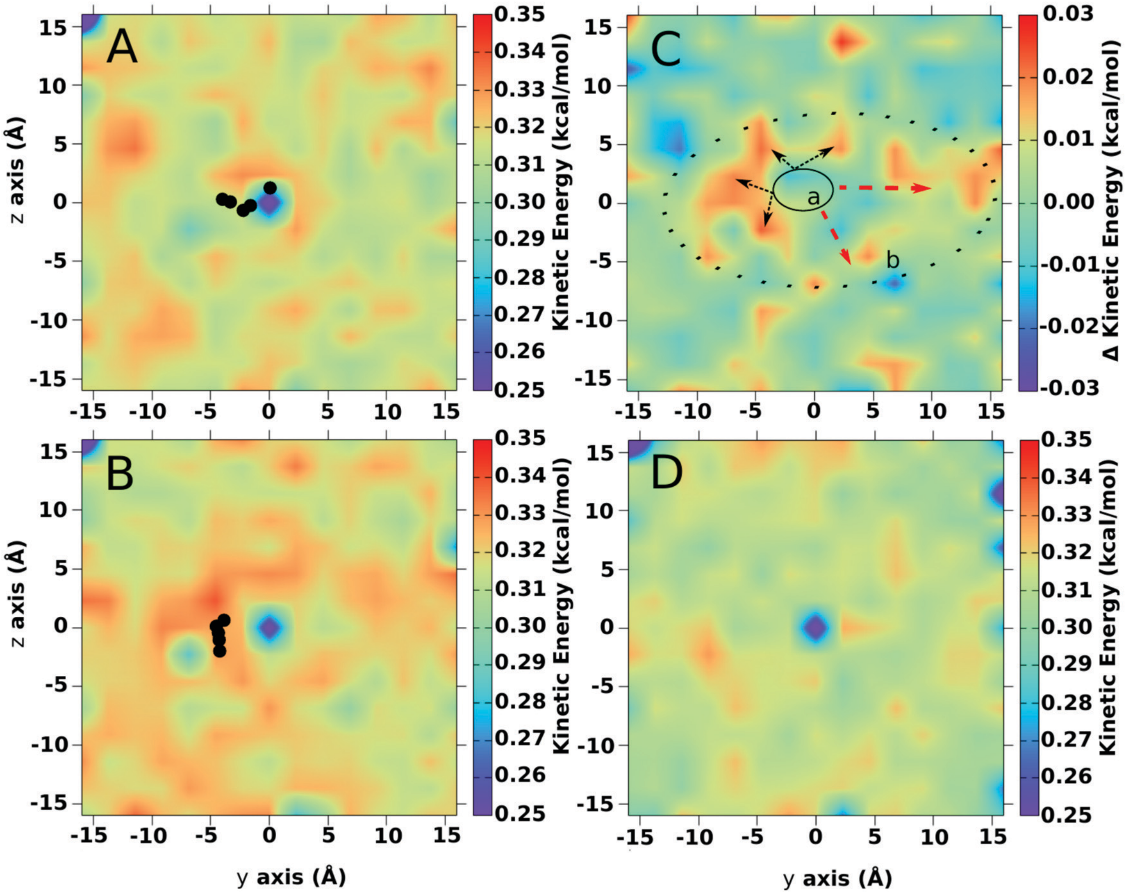

Fig. 4 Averaged temperature distribution in the (*x*, *y*)-plane averaged over 8 simulations using the RKHS PES and TIP3P water before (panel A: $-10 \leq t \leq 0$ ps) and after (panel B: $0 \leq t \leq 10$ ps) O_2-formation. Here, $t = 0$ is defined as the instance along each of the trajectories for which $r_{OO} < 2.5$ Å for the first time and all time series are aligned with respect to this reference. The color scale reports the kinetic energy (in kcal mol^{-1}). The averaged position of the center of mass of O_2 is indicated by filled circles. The low-energy region in the center of the simulation box is due to the cavity which contain fewer water molecules along the *z*-axis that can contribute to the kinetic energy. Panel C shows the difference between panels A and B which highlights the direction and magnitude of energy transfer. The region "a", delimited by the continuous line ellipse, represents the region where the recombination takes places, while the second region "b" is a qualitative delimitation of the energy flow after the reaction. Panel D shows the energy distribution for two not reacting oxygen atoms.

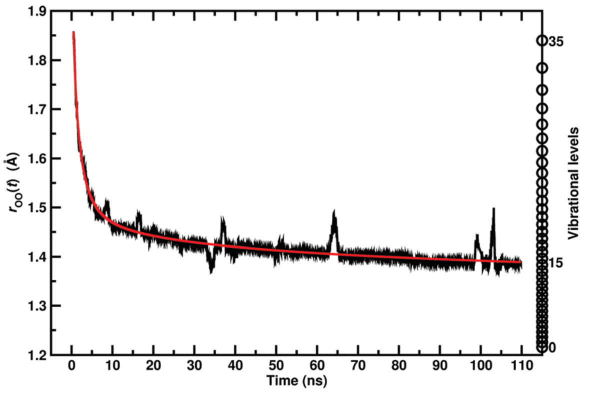

Fig. 5 Time evolution of the O_2 vibrational relaxation and its fit to a stretched exponential function (eqn (8)) for a [TIP3P/Morse] simulation with recombination on the ASW surface. Scattering of the O_2 from the surrounding water lattice leads to the peaks in the relaxation curve. The right-hand *y*-axis label reports the vibrational quantum number from solving the 1d-Schrödinger equation using LEVEL.[45] After 110 ns of simulation time the O_2 molecule is still in a state corresponding to $v = 15$.

the binding energy relax (relaxation to $\nu = 15$) within a few nanoseconds. This is followed by a second, considerably slower phase extending over many 10 s to 100 s of nanoseconds during which collisions with the surrounding water lattice can lead to de-excitation and re-excitation. Similarly, the [TIP3P/RKHS] simulation (see Fig. S2, ESI†) shows a first phase (with time constant $\tau_1^{\mathrm{DE}} = 1.1$ ns from a double exponential (DE) fit) during which the average O–O distance decreases from $\langle r_{\mathrm{OO}} \rangle = 2.1$ Å to 1.5 Å within 3.6 ns, followed by a much slower relaxation ($\tau_2^{\mathrm{DE}} = 83.4$ ns) during which the O–O separation only decreases by another 0.1 Å. Using a single stretched exponential yields $\tau_1^{\mathrm{SE}} = 1.1$ ns and $\beta_1 = 0.144$, see Table 1 and for two stretched exponentials the parameters are $\beta_1 = 0.51$ for the short-time process ($\tau_2^{\mathrm{SE}} = 0.9$ ns) and $\beta_2 = 0.02$ for the long-time process ($\tau_2^{\mathrm{SE}} = 1.2$ ns). At the end of this simulation the water temperature has increased by ∼15 K, see Fig. 6.

Simulations with the Morse Potential for the O–O coordinate and the TIP3P water model establishes that relaxation is slow. This model is computationally less demanding than the RKHS

Open Access Article. Published on 26 February 2019. Downloaded on 6/6/2019 10:53:06 AM.
This article is licensed under a Creative Commons Attribution-NonCommercial 3.0 Unported Licence.

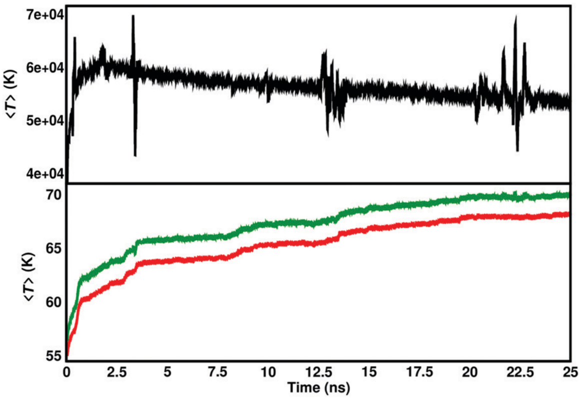

Fig. 6 The kinetic temperature of the O_2 (top panel) and the water (bottom panel, red) and the total system (green) after formation at $t = 0$ from a [TIP3P/RKHS] surface simulation. After 20 ns the average temperature of the system has increased by ∼15 K. The spikes in the black trace are due to collisions of O_2 with the surrounding water matrix.

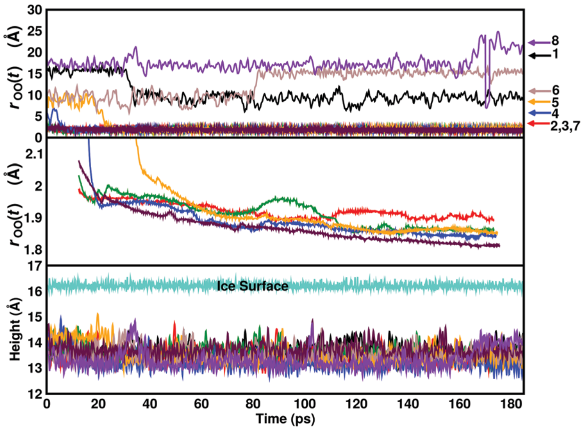

Fig. 7 Top: Time series of the O–O distance during 180 ps for eight different simulations, with one oxygen in a deep crevice: for three trajectories no recombination is observed, because the two atoms diffuse away from the cavity where the first atom is trapped; five reactions instead leads to the molecule formation. The colored arrows indicate the initial distance, r_{OO}, of the two atoms. In the central panel, the moving average of those last simulation is shown: as from the previous simulations, a slow relaxation of the O–O distance is observed. The bottom panel shows the maximum height of the ice surface, *i.e.* the maximum z-coordinate of any water molecule, compared with the z-coordinate of the center of mass of O_2. The molecules remain, in all simulations, on the surface, regardless of whether they rebind or not.

representation and longer simulations are possible. The relaxation times from the 110 ns simulation are $\tau_1 = 3.2$ ns and $\tau_2 = 207$ ns which can only be an estimate because the data from which this value was determined does not probe dynamics on this time scale. Nevertheless, these results confirm that coupling between the oxygen stretching mode and the water phonon modes is small.

To evaluate how water flexibility influences the relaxation dynamics of molecular oxygen, a 10.5 ns [KKY/RKHS] simulation was carried out. Such simulations are even more computational demanding because the KKY water is flexible and a time step of $\Delta t = 0.1$ fs is required in the MD simulation for energy conservation. Vibrational relaxation times decreases by a factor of two to four, with $\tau_1 = 0.7$ ns and $\tau_2 = 20.7$ ns for a double exponential fit. For the stretched exponential fits, the values of β increase by ∼30% compared to simulations with rigid waters (see Table 1) and the two relaxation times decrease to $\tau_1^{SE} = 0.5$ ns and $\tau_2^{SE} = 1.0$ ns. This suggests that the O_2 relaxation dynamics is somewhat less nonexponential probably due to coupling to the water matrix which also speeds up the relaxation process.

Stretched exponential decays have been employed in the past to discuss relaxation within a diffusion-trap model and to characterize the dynamics in disordered molecular systems.[46] The case $\beta = 1$ in eqn (8) corresponds to a conventional exponential decay and for all other cases $0 < \beta < 1$. The value of β can be related to the effective dimensionality of the problem through $\beta = d^*/(d^* + 2)$ where $d^* = f \times d$, d is the dimensionality of the problem (here $d = 3$) and f is the fraction of active channels for relaxation.[46] Discussing the present results (see Table 1) for one stretched exponential, it is found that for surface relaxation $\beta \sim 0.15$ whereas for relaxation within the bulk $\beta \sim 0.2$. For relaxation in the bulk and $d = 3$ this yields $f = 1/6$ whereas for relaxation on the surface the value for d is not obvious *a priori*. For $d = 3$ the number of relaxation channels is $f = 0.12$ whereas for $d = 2$ the value increases to $f = 0.18$. It is reasonable to expect that more rapid relaxation is caused by a larger number of relaxation channels (*i.e.* a larger number of collision partners). Because $\tau^{\text{bulk}} > \tau^{\text{surface}}$ for [TIP3P/RKHS] one finds $d = 2$ for the relaxation on the surface.

In order to better characterize the formation probability for the surface reaction an additional 534 simulations, using [TIP3/RKHS], were performed. The two oxygen atoms were placed in two neighboring cavities on the surface with an initial distance of 8 Å and velocities randomly chosen from a Maxwell–Boltzmann distribution at $T = 50$ K. Within 25 ps, 25% of the simulations lead to recombination with an average formation time of $\langle t_{\text{formation}} \rangle = 10.8$ ps, see Fig. 7 This establishes that not only a specifically prepared initial state leads to O_2 formation but also initial conditions which require diffusion of the two oxygen atoms before recombination can take place.

3.3 Desorption of O_2

Despite energy in excess of 100 kcal mol^{-1} is available upon oxygen recombination, which compares with desorption energies of 2 to 3 kcal mol^{-1},[4,47] O_2 remains localized on the surface for the simulations described so far. In order to explicitly probe desorption, a set of 10 simulations, 50 ps each, is run with velocities from a Maxwell–Boltzmann distribution at 50 K but with the z-component (perpendicular to the ASW surface) scaled according to

$$v_z = v_{z0}(1 + \lambda a) \tag{9}$$

with $\lambda \in [0,\ldots,50]$ in increments of 1, and $a = 0.1$. With increasing λ the velocity orthogonal to the surface increases and desorption becomes more probable. For each value of λ the average probability for desorption was determined.

Open Access Article. Published on 26 February 2019. Downloaded on 6/6/2019 10:53:06 AM.
This article is licensed under a Creative Commons Attribution-NonCommercial 3.0 Unported Licence.

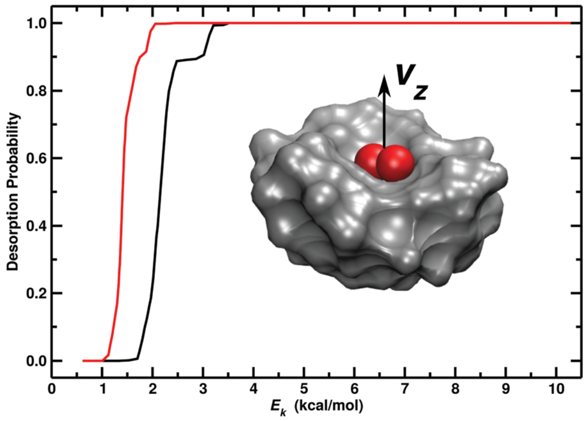

Fig. 8 Probability for desorption from an average over 10 independent simulations with different *z* components perpendicular to the ASW surface. Black trace: simulations with rigid (TIP3P) water; red trace: simulations with the flexible KKY model. Desorption occurs for a vertical component of the kinetic energy of ~1.7 kcal mol^{-1} and for ~1.2 kcal mol^{-1}, for TIP3P and KKY, respectively. The process is illustrated in the schematic.

For a rigid water model, desorption is observed for an average perpendicular kinetic energy of 2.0 kcal mol^{-1} (see Fig. 8 black curve). If desorption occurs it takes place within 0.5 ps. Similar results are obtained when using a flexible water model but the energy for desorption is reduced to 1.5 kcal mol^{-1} (see Fig. 8) because the O_2 stretch can now couple to the water deformation modes. Such energies for desorption are consistent with those determined from laboratory experiments of 1.8 kcal mol^{-1}.[47]

4 Discussion and conclusion

In this work formation of molecular oxygen on cold ASW surfaces is examined both inside amorphous solid water and on its surface. Oxygen (^{3}P) migration in and on ASW has been found from simulations[4] and in experiments using neon matrices.[21] If two oxygen atoms O(^{3}P) approach one another sufficiently closely the process is rapid as it is barrierless. Once O_2 has formed, relaxation of the highly excited molecule takes place on the 10 to 100 ns time scale with full relaxation requiring considerably longer, though, well beyond the current simulation times. The rate limiting step for vibrational relaxation is coupling to the water phonon modes. For O_2 recombination on ASW it is found that even the highly vibrationally excited molecule does usually not desorb which also occurs due to inefficient coupling of the O_2 stretch to the water-phonon modes. With a flexible water model the desorption energy decreases by 25% compared to rigid water and vibrational energy relaxation speeds up by a factor of ~4.

Experimentally, vibrational energy transfer has been found to be very inefficient for NO near the surface of an insulator. For NO(ν = 1) the survival probability of scattering from LiF is 70% to 100%, with error bars up to 100% at all energies.[48] More recently, high survival probabilities (small probabilities for vibrational relaxation) have also been found for NO(ν = 12) on LiF(001).[49] Similarly, the probability for vibrational excitation of NO scattered from diamond was found to be only 5×10^{-3} and the vibrational relaxation probability of CO(ν = 1) on LiF is of comparable magnitude (10^{-3}).[50] Finally, on NaCl(100), CO vibrational energy relaxation occurs on the ms time scale.[51] Relaxation on insulators (mainly by phonons) is inefficient due to the large mismatch in the frequencies of the diatomic and the phonons which leads to small coupling between these degrees of freedom. Conversely, for a conductive solid, coupling of intramolecular vibrations with phonons and electron–hole pairs accelerates energy transfer such as for vibrational relaxation of CO on Cu(111) which occurs on the ps timescale.[52]

Photolysis of adsorbed SO_2 onto ASW and recombination of O(^{3}P), which is the process considered here, leads exclusively to $O_2(^3\Sigma_g^-)$, predominantly in vibrationally excited states $\nu \leq 3$. The time of flight in these experiments is on the order of μs which agrees quite well with results from the present simulations. Extrapolating the stretched exponential decay from the [KKY/RKHS] simulations from recombination on the ASW surface (see Table 1) to 1 μs yields r_{OO} = 1.2386 Å which corresponds to ν = 2, consistent with experiment.[17] Formation of electronically excited $O_2(^1\Delta_g$ and $^1\Sigma_g^+)$ has been found from OH + O(^{3}P) involving a barrierless and an activated process, respectively.[17] The fraction of O_2 in its $^1\Delta_g$ state was 2.5%.[53] Given that the $^3\Sigma_g^-$, $^1\Delta_g$, and $^1\Sigma_g^+$ of O_2 dissociate to the same asymptote (O(^{3}P) + O(^{3}P)) it will be interesting to include electronically excited states in future work. For these states PESs of similar quality are available.[35] The recombination dynamics can be treated with trajectory surface hopping (TSH)[54] including nonadiabatic transitions within the Landau–Zener[55,56] formalism. This has recently been done using multidimensional RKHS PESs for the reactive dynamics of the [CNO]-system.[57]

The long vibrational relaxation times (ns to ~μs or probably even longer) found here for O_2 on ASW are consistent with vibrational relaxation of a high-frequency diatomic on an insulating surface such as water. If the water molecules lack internal degrees of freedom (rigid, TIP3P) the relaxation times are longer by about a factor of 4 compared with simulations in which the water-bending mode is available for coupling (flexible, KKY). For more quantitative results on the vibrational relaxation times much longer MD simulations will be required, though.

The present findings suggest that diffusion of atomic species followed by collisions in and on ASW and subsequent vibrational relaxation can lead to stable molecules at low temperatures. This complements and is in agreement with laboratory experiments that find generation of O_2 and O_3.[2,13,14,17,21,58–60] Such a mechanism for O_2 formation may also be operative at conditions prevalent in the interstellar medium although there, alternative routes such as the reactive O + OH collision are considered to be important, too.[16,17]

Conflicts of interest

There are no conflicts to declare.

Acknowledgements

This work was supported by the Swiss National Science Foundation through grants 200021-117810, and the NCCR MUST.

Open Access Article. Published on 26 February 2019. Downloaded on 6/6/2019 10:53:06 AM. This article is licensed under a Creative Commons Attribution-NonCommercial 3.0 Unported Licence.

References

1 E. Matar, E. Congiu, F. Dulieu, A. Momeni and J. L. Lemaire, Mobility of D atoms on porous amorphous water ice surfaces under interstellar conditions, *Astron. Astrophys.*, 2008, **492**, L17–L20.

2 M. Minissale, E. Congiu, S. Baouche, H. Chaabouni, A. Moudens, F. Dulieu, M. Accolla, S. Cazaux, G. Manico and V. Pirronello, Quantum Tunneling of Oxygen Atoms on Very Cold Surfaces, *Phys. Rev. Lett.*, 2013, **111**, 053201.

3 M. W. Lee and M. Meuwly, Diffusion of atomic oxygen relevant to water formation in amorphous interstellar ices, *Faraday Discuss.*, 2014, **168**, 205–222.

4 M. Pezzella, O. T. Unke and M. Meuwly, Molecular Oxygen Formation in Interstellar Ices Does Not Require Tunneling, *J. Phys. Chem. Lett.*, 2018, **9**, 1822–1826.

5 A. G. G. M. Tielens and W. Hagen, Model Calculations of the Molecular Composition of Interstellar Grain Mantles, *Astron. Astrophys.*, 1982, **114**, 245–260.

6 D. Ruffle and E. Herbst, New models of interstellar gas-grain chemistry – III. Solid CO_2, *Mon. Not. R. Astron. Soc.*, 2001, **324**, 1054–1062.

7 S. B. Charnley and S. D. Rodgers, in *Astrochemistry: Recent Successes and Current Challenges*, ed. D. C. Lis, G. A. Blake, E. Herbst, International Astronomical Union, 2006, pp. 237–246.

8 H. M. Cuppen and E. Herbst, Simulation of the formation and morphology of ice mantles on interstellar grains, *Astrophys. J.*, 2007, **668**, 294–309.

9 B. Larsson, *et al.*, Molecular oxygen in the ρ Ophiuchi cloud, *Astron. Astrophys.*, 2007, **466**, 999–1003.

10 R. Liseau, *et al.*, Multi-line detection of O_2 toward ρ Opiuchi A, *Astron. Astrophys.*, 2012, **541**, A73.

11 J. He, K. Acharyya and G. Vidali, Binding Energy of Molecules on Water Ice: Laboratory Measurements and Modeling, *Astrophys. J.*, 2016, **825**, 89.

12 J. He, S. Emtiaz and G. Vidali, Measurements of Diffusion of Volatiles in Amorphous Solid Water: Application to Interstellar Medium Environments, *Astrophys. J.*, 2018, **863**, 156.

13 C. J. Bennett and R. I. Kaiser, Laboratory Studies on the Formation of Ozone (O_3) on Icy Satellites and on Interstellar and Cometary Ices, *Astrophys. J.*, 2005, **635**, 1362.

14 B. Sivaraman, C. S. Jamieson, N. J. Mason and R. I. Kaiser, Temperature-dependent Formation of Ozone in Solid Oxygen by 5 keV Electron Irradiation and Implications for Solar System Ices, *Astrophys. J.*, 2007, **669**, 1414.

15 C. Ceccarelli, D. J. Hollenbach and A. G. G. M. Tielens, Far-Infrared Line Emission from Collapsing Protostellar Envelopes, *Astrophys. J.*, 2009, **471**, 400.

16 S. Viti, E. Roueff, T. W. Hartquist, G. Pineau des Forêts and D. A. Williams, Interstellar oxygen chemistry, *Astron. Astrophys.*, 2001, **370**, 557–569.

17 T. Hama, M. Yokoyama, A. Yabushita and M. Kawasaki, Role of OH radicals in the formation of oxygen molecules following vacuum ultraviolet photodissociation of amorphous solid water, *J. Chem. Phys.*, 2010, **133**, 104504.

18 R. Atkinson, D. L. Baulch, R. A. Cox, J. N. Crowley, R. F. Hampson, R. G. Hynes, M. E. Jenkin, M. J. Rossi and J. Troe, Evaluated kinetic and photochemical data for atmospheric chemistry: volume – gas phase reactions of O_x, HO_x, NO_x and SO_x species, *Atmos. Chem. Phys.*, 2004, **4**, 1461–1738.

19 D. Quan, E. Herbst, T. J. Millar, G. E. Hassel, S. Y. Lin, H. Guo, P. Honvault and D. Xie, New Theoretical Results Concerning the Interstellar Abundance of Molecular Oxygen, *Astrophys. J.*, 2008, **681**, 1318.

20 V. Wakelam, *et al.*, A KInetic Database for Astrochemistry (KIDA), *Astrophys. J., Suppl. Ser.*, 2012, **199**, 21.

21 J.-I. Lo, S.-L. Chou, Y.-C. Peng, H.-C. Lu, J. F. Ogilvie and B.-M. Cheng, Thresholds of photolysis of O_2 and of formation of O_3 from O_2 dispersed in solid neon, *Phys. Chem. Chem. Phys.*, 2018, **20**, 13113–13117.

22 M. Minissale, E. Congiu, G. Manicò, V. Pirronello and F. Dulieu, CO_2 formation on interstellar dust grains: a detailed study of the barrier of the CO channel, *Astron. Astrophys.*, 2013, **559**, A49.

23 E. Hebrard, M. Dobrijevic, P. Pernot, N. Carrasco, A. Bergeat, K. M. Hickson, A. Canosa, S. D. Le Picard and I. R. Sims, How measurements of rate coefficients at low temperature increase the predictivity of photochemical models of Titan's atmosphere, *J. Phys. Chem. A*, 2009, **113**, 11227–11237.

24 R. T. Garrod and T. Pauly, On the Formation of CO_2 and Other Interstellar Ices, *Astrophys. J.*, 2011, **735**, 15.

25 D. A. Williams and C. Cecchi-Pestellini, *The Chemistry of Cosmic Dust*, The Royal Society of Chemistry, 2016, pp. P001–304.

26 R. Johnson, P. Cooper, T. Quickenden, G. Grieves and T. Orlando, Production of oxygen by electronically induced dissociations in ice, *J. Chem. Phys.*, 2005, **123**, 184715.

27 B. Brooks, *et al.*, CHARMM: the biomolecular simulation program, *J. Comput. Chem.*, 2009, **30**, 1545–1614.

28 T. Nagy, J. Y. Reyes and M. Meuwly, Multi-Surface Adiabatic Reactive Molecular Dynamics, *J. Chem. Theory Comput.*, 2014, **10**, 1366–1375.

29 J. Danielsson and M. Meuwly, Atomistic Simulation of Adiabatic Reactive Processes Based on Multi-State Potential Energy Surfaces, *J. Chem. Theory Comput.*, 2008, **4**, 1083.

30 D. R. Nutt and M. Meuwly, Studying Reactive Processes with Classical Dynamics: Rebinding Dynamics in MbNO, *Biophys. J.*, 2006, **90**, 1191–1201.

31 W. L. Jorgensen, J. Chandrasekhar, J. D. Madura, R. W. Impey and M. L. Klein, Comparison of simple potential functions for simulating liquid water, *J. Chem. Phys.*, 1983, **79**, 926–935.

32 N. Kumagai, K. Kawamura and T. Yokokawa, An Interatomic Potential Model for H_2O: Applications to Water and Ice Polymorphs, *Mol. Simul.*, 1994, **12**, 177–186.

33 N. Plattner and M. Meuwly, Atomistic Simulations of CO Vibrations in Ices Relevant to Astrochemistry, *ChemPhysChem*, 2008, **9**, 1271–1277.

34 J. Huang and A. D. MacKerell, CHARMM36 all-atom additive protein force field: validation based on comparison to NMR data, *J. Comput. Chem.*, 2013, **34**, 2135–2145.

Open Access Article. Published on 26 February 2019. Downloaded on 6/6/2019 10:53:06 AM. This article is licensed under a Creative Commons Attribution-NonCommercial 3.0 Unported Licence.

35 L. Bytautas, N. Matsunaga and K. Ruedenberg, Accurate *ab initio* potential energy curve of O_2. II. Core–valence correlations and relativistic contributions and vibration–rotation spectrum, *J. Chem. Phys.*, 2010, **132**, 1–15.

36 T. Hollebeek, T.-S. Ho and H. Rabitz, Constructing Multidimensional Molecular Potential Energy Surfaces from *Ab Initio* Data, *Annu. Rev. Phys. Chem.*, 1999, **50**, 537–570.

37 O. T. Unke and M. Meuwly, Toolkit for the Construction of Reproducing Kernel-Based Representations of Data: Application to Multidimensional Potential Energy Surfaces, *J. Chem. Inf. Model.*, 2017, **57**, 1923–1931.

38 T. Hama and N. Watanabe, Surface Processes on Interstellar Amorphous Solid Water: Adsorption, Diffusion, Tunneling Reactions, and Nuclear-Spin Conversion, *Chem. Rev.*, 2013, **113**, 8783–8839.

39 T. Kawabata, Detection of multiscale pockets on protein surfaces using mathematical morphology, *Proteins*, 2010, **78**, 1195–1211.

40 J. Phillips, Microscopic aspects of Stretched Exponential Relaxation (SER) in homogeneous molecular and network glasses and polymers, *J. Non-Cryst. Solids*, 2011, **357**, 3853–3865.

41 P. J. Steinbach, *et al.*, Ligand binding to heme proteins: connection between dynamics and function, *Biochemistry*, 1991, **30**, 3988–4001.

42 I. Langmuir, The mechanism of the catalytic action of platinum in the reactions $2CO + O_2 \rightarrow 2CO_2$ and $2H_2 + O_2 \rightarrow 2H_2O$, *Trans. Faraday Soc.*, 1922, **17**, 0621–0654.

43 C. N. Hinshelwood and N. V. Sidgwick, On the theory of unimolecular reactions, *Proc. R. Soc. A*, 1926, **113**, 230–233.

44 D. D. Eley, On the solubility of gases. Part I. The inert gases in water, *Trans. Faraday Soc.*, 1939, **35**, 1281–1293.

45 R. J. L. Roy, LEVEL: a computer program for solving the radial Schrödinger equation for bound and quasibound levels, *J. Quant. Spectrosc. Radiat. Transfer*, 2017, **186**, 167–178.

46 J. Phillips, Stretched exponential relaxation in molecular and electronic glasses, *Rep. Prog. Phys.*, 1996, **59**, 1133–1207.

47 J. A. Noble, E. Congiu, F. Dulieu and H. J. Fraser, Thermal desorption characteristics of CO, O_2 and CO_2 on non-porous water, crystalline water and silicate surfaces at submonolayer and multilayer coverages, *Mon. Not. R. Astron. Soc.*, 2012, **421**, 768–779.

48 J. Misewich, H. Zacharias and M. Loy, State-to-State Molecular-Beam Scattering of Vibrationally Excited NO from Cleaved LiF(100) Surfaces, *Phys. Rev. Lett.*, 1985, **55**, 1919–1922.

49 A. Wodtke, Y. Huang and D. Auerbach, Interaction of NO(ν = 12) with LiF(001): evidence for anomalously large vibrational relaxation rates, *J. Chem. Phys.*, 2003, **118**, 8033–8041.

50 R. Jongma, G. Berden, T. Rasing, H. Zacharias and G. Meijer, Scattering of vibrationally and electronically excited CO molecules from a LiF(100) surface, *Chem. Phys. Lett.*, 1997, **273**, 147–152.

51 H.-C. Chang and G. E. Ewing, Infrared fluorescence from a monolayer of CO on NaCl(100), *Phys. Rev. Lett.*, 1990, **65**, 2125–2128.

52 D. J. Auerbach and A. M. Wodtke, in *Dynamics of Gas-Surface Interactions: Atomic-level Understanding of Scattering Processes at Surfaces*, ed. R. Díez Muiño and H. F. Busnengo, Springer Berlin Heidelberg, Berlin, Heidelberg, 2013, pp. 267–297.

53 S. T. Lunt, G. Marston and R. P. Wayne, Formation of $O_2(a^1\Delta)$ and vibrationally excited OH in the reaction between O atoms and HO_x species, *J. Chem. Soc., Faraday Trans. 2*, 1988, **84**, 899–912.

54 J. R. Stine and J. T. Muckerman, *J. Chem. Phys.*, 1976, **65**, 3975.

55 L. D. Landau, Zur Theorie der Energiübertragung. II, *Phys. Z.*, 1932, **2**, 46.

56 C. Zener, Non-Adiabatic Crossing of Energy Levels, *Proc. R. Soc. London, Ser. A*, 1932, **137**, 696.

57 D. Koner, R. J. Bemish and M. Meuwly, The $C(^3P) + NO(X^2\Pi) \rightarrow O(^3P) + CN(X^2\Sigma^+)$, $N(^2D)/N(^4S) + CO(X^1\Sigma^+)$ reaction: Rates, branching ratios, and final states from 15 K to 20 000 K, *J. Chem. Phys.*, 2018, **149**, 094305.

58 B. Sivaraman, A. M. Mebel, N. J. Mason, D. Babikov and R. I. Kaiser, On the electron-induced isotope fractionation in low temperature $^{32}O_2/^{36}O_2$ ices ozone as a case study, *Phys. Chem. Chem. Phys.*, 2011, **13**, 421–427.

59 D. Jing, J. He, J. R. Brucato, G. Vidali, L. Tozzetti and A. D. Sio, Formation of Molecular Oxygen and Ozone on Amorphous Silicates, *Astrophys. J.*, 2012, **756**, 98.

60 H. M. Cuppen, S. Ioppolo, C. Romanzin and H. Linnartz, Water formation at low temperatures by surface O_2 hydrogenation II: the reaction network, *Phys. Chem. Chem. Phys.*, 2010, **12**, 12077–12088.

Electronic Supplementary Material (ESI) for Physical Chemistry Chemical Physics.
This journal is © the Owner Societies 2019

Supplementary Information: O_2 Formation in Cold Environments

Marco Pezzella and Markus Meuwly*

Department of Chemistry, University of Basel, Klingelbergstrasse 80, CH-4056 Basel, Switzerland.

E-mail: m.meuwly@unibas.ch

January 22, 2019

The supplementary information provides additional information about the energy conservation of various implementation of reactive dynamics implemented in the main report"

S1 KKY simulations

The KKY model was implemented in CHARMM c41. The implementation of the code and parameters are those used in previous work.[1] To validate the implementation, a 2 ns NVE simulation was carried out and the fluctuation in the total energy is reported in Figure S1. The normal mode frequencies from the KKY model and from experiment also agree quite favourable, see Table S1

---

[*] To whom correspondence should be addressed

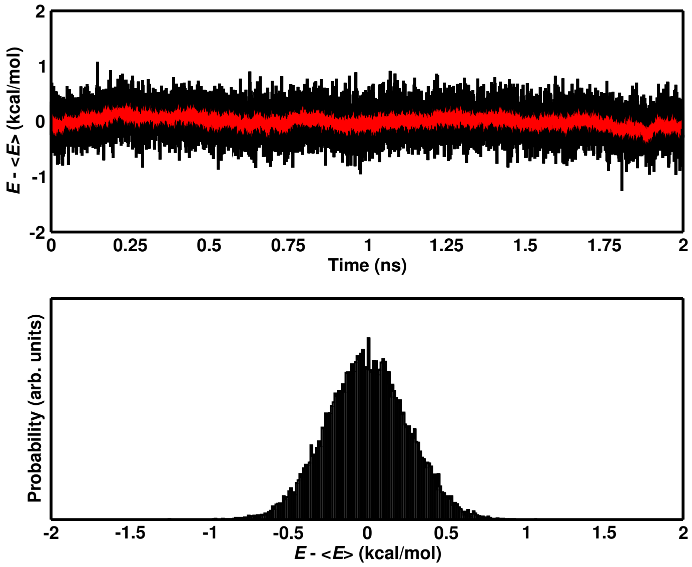

Figure S1: KKY with RKHS or Morse for O_2 Top: Total Energy time series for 2 ns simulation of relaxed O_2 with the flexible H_2O. The energy is conserved within 1 kcal/mol, and presents a Gaussian Shaped distribution (bottom panel).

MODE	NIST Database (cm^{-1})	KKY (cm^{-1})	Difference (cm^{-1})
Symmetric Stretch	3657	3682	+25
Antisymmetric Stretch	3756	3720	-36
Bending	1595	1593	-2

S2 Exponential and Stretched Exponential Fits

Additional fitts of the relaxation curves to exponential and stretched exponential models are summarized in the following.

References

(1) Plattner, N.; Meuwly, M. Atomistic Simulations of CO Vibrations in Ices Relevant to Astrochemistry. *ChemPhysChem* **2008**, *9*, 1271–1277.

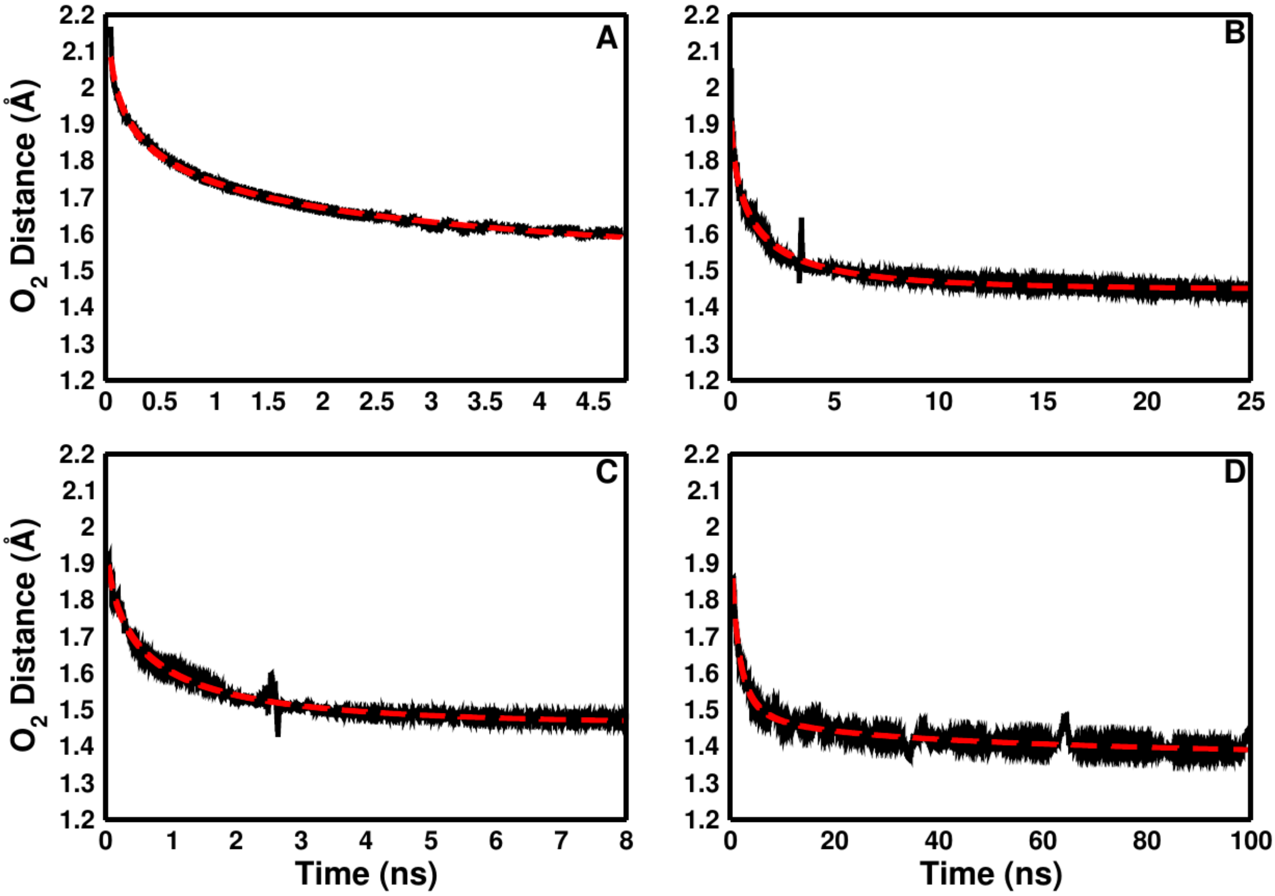

Figure S2: Vibrational relaxation for O_2 recombination inside the cavity (panel A) and on the surface of ASW (panels B to D). The 16 simulations in panel A were run with [TIP3P/RKHS]. Fitting to a double exponential decay gives relaxation times $\tau_1 = 0.5$ ns and $\tau_2 = 15$ ns. Simulations in panels B to D were run with [TIP3P/RKHS] ($\tau_1 = 1.1$ ns and $\tau_2 = 83.4$ ns), [KKY/RKHS] ($\tau_1 = 0.7$ ns and $\tau_2 = 20.7$ ns) and [TIP3P/Morse] ($\tau_1 = 3.0$ ns and $\tau_2 = 206.9$ ns). The right-hand $y-$axis label reports the vibrational quantum number from solving the 1d-Schrödinger equation using LEVEL.[2] After 20 to 80 ns of simulation time the O_2 molecule is still in a state corresponding to $v = 16$ to 20.

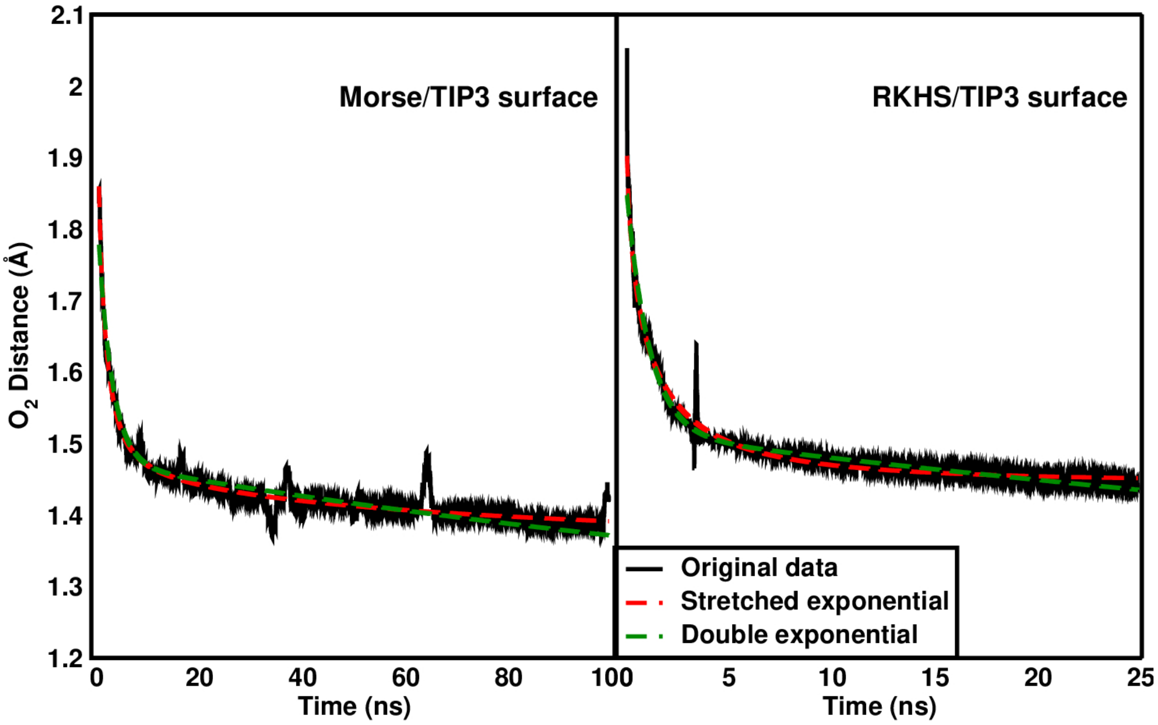

Figure S3: Comparison between the stretched exponential (red) and double exponential (green) decay between for simulations with [TIP3P/Morse] (right) and [TIP3P/RKHS] (left). A stretched exponential better captures the early time decay and the flattening out at long times. The relaxation times corresponding to this data is reported in Table 1.

(2) Roy, R. J. L. LEVEL: A computer program for solving the radial Schrdinger equation for bound and quasibound levels. *J. Quant. Spectrosc. Radiat. Transfer* **2017**, *186*, 167 – 178.

3. Recombination of O_2 in ground and excited states

O_2 recombination can lead to the production of a ground state ($^3\Sigma_g^-$) or an excited states ($^1\Delta_g$ and $^1\Sigma_g^+$) molecule. In this second case it will not remain in the excited state indefinitely and will relax back to its ground state. Relaxation can happen by different mechanism involving the absorption/desorption of a photon or nonradiative transitions (*vibrational relaxation*) (VR). O_2 can relax, emitting a photon *via fluorescence*, when both states have the same spin multiplicity, or *via posphorence*, when the spin selection rule is violated. In the case of overlap between rovibrational levels of two electronic states with different spin multiplicity, the system can undergo an *intersystem crossing* (ISC). Non radiative spins' conserving transitions are called *internal conversion.* Table 3.1 shows the possible mechanism and some of their characteristics.

Table 3.1.: Radiative and collisional process leading to the relaxation of an excited molecule.

Process	Spin Forbidden	Time scale (s)
Fluorescence	no	10^{-9}
Internal conversion	no	10^{-12} - 10^{-7}
Vibrational relaxation	both	10^{-14}
Intersystem crossing	yes	10^{-12} - 10^{-3}
Phosphorescence	yes	10^{-7} - 10^{-5}

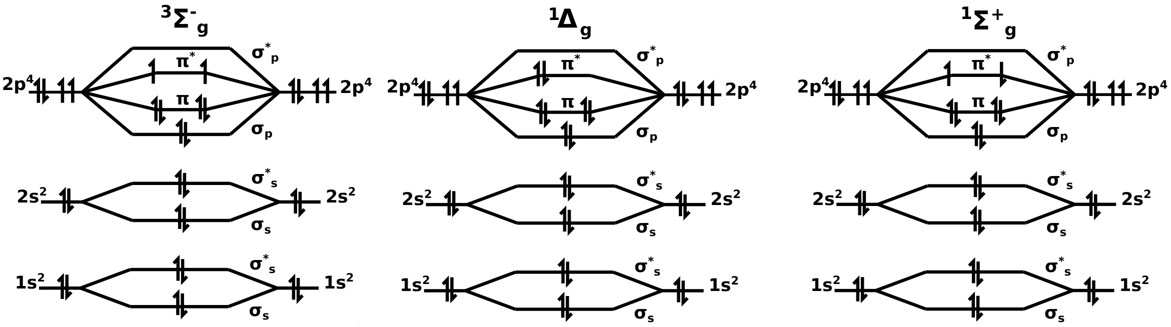

Figure 3.1.: Molecular Orbital representation for the first three states of O_2.

For the purpose of this study, fluorescence and phosphorescence are not considered due to their long time scales and their violation of the energy conservation during the simulation. The time limitation is relevant in case of phosphorescence where each single simulation needs to be carried out for an average of 10^{10} steps in order to observe this phenomenon. The energy conservation problems derives from the large energy difference between the initial and final state that would prohibit a correct temperature sampling and would require the implementation of more robust energy propagators. No internal conversion is observed, because $^1\Delta_g$ and $^1\Sigma_g^+$ states do not overlap. The only two phenomena observed are the ISC and VR. They require that the two PES describing the electronic states should couple along some points in its coordinates and they cannot be described by adiabatic PES because the coupling between nuclei and electrons is neglected. Nonadiabatic corrections are applied for including the coupling between two surfaces and then they perform nonadiabatic transitions.

The complexity of electronic transitions involving O_2 derive from their electronic configurations, illustrated in Figure 3.1 in which both π^* orbitals contains only one electron.

For nonadiabatic transitions the trajectory surface hopping (TSH) method[27] within the Landau-Zener (LZ)[28,29] formalism is used and it is described in the supporting information of the article.

For the $^1\Delta_g \rightarrow ^3\Sigma_g^-$ transition, ΔH_{jk} (the nonadiabitc coupling between the two surfaces) is simply calculated trough non adiabatic coupling, while the *spin orbit coupling* (SOC) is used for describing the $^1\Sigma_g^+ \rightarrow ^3\Sigma_g^-$ transition.

3.1. Spin orbit coupling

The Hamilitonian in Equation **??** is a good approximation of the real Hamiltonian of a molecular system but does not take into account small contributions derived from spin-spin and spin-orbit interactions. The last kind of interaction is important in all situations where states with different multiplicity cross together. The spin orbit interaction, or SOC, represent the interaction of the magnetic moment associated with the spin of an electron (s) with the magnetic field generated by the current produced by electron's own orbital motion (l). Its contribution, $\hat{H}_{\mathrm{SO}}$, can be considered a perturbation of the Hamiltionan in Equation **??** $\hat{H}_0$. The total Hamiltionan $\hat{H}$ can be rewritten as:

$$\hat{H} = \hat{H}_0 + \hat{H}_{\mathrm{SO}} \tag{3.1}$$

with $\hat{H}_{\mathrm{SO}}$ expression derived by relativistic treatment of the electron. For an $N-$electron system the expression is equal to:

$$\hat{H}_{\mathrm{SO}} = \frac{1}{2m_e c^2}\left(\sum_i \frac{\partial V_i}{r_i \partial r_i}\left(\mathbf{L}_i \cdot \mathbf{S}_i\right)\right) \tag{3.2}$$

m_e is the electron mass, c is the speed of light, r_i is the distance of the i^{th} electron from the electric field that this electron crosses, $\frac{\partial V_i}{\partial r_i}$ the Coulomb interaction gradient, $\mathbf{L}_i$ and $\mathbf{S}_i$ are the total orbital angular momentum and the total spin moment of the electron.

The term $\mathbf{L} \cdot \mathbf{S}$ can be defined using the total angular momentum of an electron ($\mathbf{J}$):

$$\mathbf{J} = \mathbf{L} + \mathbf{S} \tag{3.3}$$

more specifically its square modulus:

$$J^2 = L^2 + S^2 + 2\left(\mathbf{L} \cdot \mathbf{S}\right) \tag{3.4}$$

leading to:

$$\mathbf{L} \cdot \mathbf{S} = \frac{1}{2}\left(\mathbf{J}^2 - \mathbf{L}^2 - \mathbf{S}^2\right) \tag{3.5}$$

For systems composed of light atoms, $\mathbf{J}$ is evaluated using the Russell-Saunders coupling, in which all electron spin momenta are summed together, the same for the angular momenta:

$$\mathbf{J} = \sum_i \mathbf{l}_i + \sum_i \mathbf{s}_i \tag{3.6}$$

The idea that SOC is only effective for electron-rich systems is known in the scientific community[30]. In systems like atomic fluorine, the SO splitting of the ground state is 404.1 cm^{-1}[31], and ignoring SOC would result in a mismatch between experimental and computed spectra. In organic systems, SOC is a primary decay process for metastable triplet states, through ISC[32].

In case of O_2, SOC is important in the context of high vibrational levels self-relaxation. A perfect agreement between experiments and *ab-initio* calculations is found below $\nu = 25$[33] but not for higher levels[34]. The explanation of this mismatch is found in the crossing between $O_2(^3\Sigma_g^-, \nu = 28)$ and $O_2(^1\Sigma_g^+, \nu = 19)$ and its inclusion recovers the agreements between experiments and computation[35].

The Journal of Physical Chemistry Letters

pubs.acs.org/JPCL Letter

Formation and Stabilization of Ground and Excited-State Singlet O_2 upon Recombination of ^3P Oxygen on Amorphous Solid Water

Marco Pezzella, Debasish Koner, and Markus Meuwly*

Cite This: *J. Phys. Chem. Lett.* 2020, 11, 2171−2176

Read Online

ACCESS | Metrics & More | Article Recommendations | Supporting Information

ABSTRACT: The recombination dynamics of ^3P oxygen atoms on cold amorphous solid water to form triplet and singlet molecular oxygen (O_2) is investigated under conditions representative of cold clouds. Reactive molecular dynamics simulations including Landau−Zener-based hopping to account for nonadiabatic transitions find that both ground-state ($X^3\Sigma_g^-$) O_2 and molecular oxygen in the two lowest singlet states ($a^1\Delta_g$ and $b^1\Sigma_g^+$) can be formed and the molecular species stabilize through vibrational relaxation. The relative populations of the species are approximately 1:1:1. These results also agree qualitatively with a kinetic model based on simplified wavepacket simulations. The presence and stabilization of higher electronic states of O_2 are expected to modify the chemical evolution of cold interstellar ($T \sim 10−50$ K) and warmer noctilucent ($T \sim 100$ K) clouds.

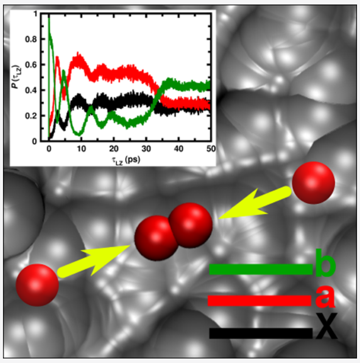

Downloaded via UNIV OF BASEL on March 6, 2020 at 15:05:25 (UTC).
See https://pubs.acs.org/sharingguidelines for options on how to legitimately share published articles.

The role of electronically excited states of oxygen, in particular, that of singlet O_2, is well established in biological, atmospheric,[1,2] and combustion chemistry.[3−5] Combustion processes involving H_2, CO, or CH_4 are accelerated in the presence of O_2 in its $a^1\Delta_g$ and $b^1\Sigma_g^+$ states, compared to reactions with O_2 in the $X^3\Sigma_g^-$ ground state.[4] No such effects are observed for the combustion of N_2.[4] Computational studies[2] on $CH_2 + O_2$ and thiophene[1] probe different aspects of O_2 excited-state reactivity: in the first case, no difference between the ground state and the second excited state is encountered, while for thiophene, the singlet oxygen channel seems to be dominant.

Recently, the possibility of oxygen diffusion and recombination of two ^3P oxygen to form ground-state O_2 in dark molecular clouds was established.[6,7] Given this, it is also of interest to explore the possibility that O_2 can be formed in low-lying electronically excited states under interstellar conditions. The oxygen chemistry network on grain surfaces leads to formation of O_3, HO_2, and eventually H_2O and OH.[8] In essence, O_2 has been ascribed a "catalytic" role in H_2O formation, which makes it one of the essential species in this process. Another potentially relevant process involving oxygen ^3P on ASW is the abstraction of a hydrogen atom to form OH+OH. However, this process has been found to involve a barrier of ∼17 kcal/mol and is therefore not expected to play a role under cold conditions.[9]

Experimental spectroscopic observations show that recombination of two oxygen atoms (^3P) generated from photolysis of $^{16}O_2$ using far-ultraviolet light in neon matrices at low temperature ($T \sim 5$ K) leads to formation of O_2 in its $X^3\Sigma_g^-$, $a^1\Delta_g$, $b^1\Sigma_g^+$, and additionally, more highly excited electronic states,[10] although the relative populations of the states were not reported. The first ($^1\Delta_g$) and second ($^1\Sigma_g^+$) excited states are of particular interest, due to their higher reactivity compared to the ground state. In the gas phase and in isolation, the two transitions $a^1\Delta_g \rightarrow X^3\Sigma_g^-$ and $b^1\Sigma_g^+ \rightarrow X^3\Sigma_g^-$ are symmetry forbidden with radiative lifetimes of 4000 and 150 s, induced by magnetic−dipole and electric−quadrupole interactions,[11] respectively. A major contributor to the $b^1\Sigma_g^+ \rightarrow X^3\Sigma_g^-$ transition is the first-order spin−orbit coupling close to the ($\nu = 28, N = 5$) of the ground state.[12] Collision induced emission has been reported to accelerate the $a^1\Delta_g \rightarrow X^3\Sigma_g^-$ transition, being 9 orders of magnitude faster (500 μs vs 4000 s) than the radiative emission.[13] However, in the presence of a symmetry-breaking environment such as amorphous solid water, these transitions can occur due to the perturbations induced by the surface. Relaxation from the $^1\Sigma_g^+$ state to $^3\Sigma_g^-$ occurs via inter system crossing (ISC), governed by spin orbit coupling (SOC) that can be described using the Landau−Zener (LZ) formalism.[14,15]

Here, the possibility is explored that upon O(^{3}P) + O(^{3}P) recombination on amorphous solid water (ASW), see Figure 1, not only the ground ($X^3\Sigma_g^-$) but also the electronically excited states of molecular oxygen, i.e., O_2 ($b^1\Delta_g$ and $a^1\Sigma_g^+$) are formed, stabilized, and populated. ASW, which is a form of glassy water, is considered to be the main component of ices on top of the small grains present in interstellar clouds.[16,17] The high porosity of ASW[18−20] makes it a good catalyst for gas−surface reactions

Received: January 14, 2020
Accepted: February 14, 2020
Published: February 14, 2020

© XXXX American Chemical Society

https://dx.doi.org/10.1021/acs.jpclett.0c00130
J. Phys. Chem. Lett. 2020, 11, 2171−2176

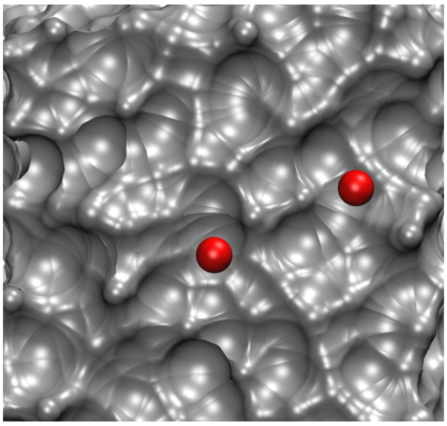

Figure 1. Simulation system with water bulk represented in gray, with the two oxygen atoms on top of the surface in red.

involving oxygen,[6,7,21−25] hydrogen,[26] carbonaceous,[27,28] and nitrogen-containing[29] species and helps maintaining those species on the surface.[30,31] Using reactive molecular dynamics simulations[32] with nonadiabatic transitions, the dynamics, relaxation, and population distribution after partial vibrational equilibration of O_2 in the three lowest electronic states are characterized in the following.

Here, a two- and a three-state model is explored. The two-state model characterizes the dynamics for one electronic transition which becomes allowed in the presence of an environment. For the more complete three-state model, only two out of the three transitions occur (see below). These models are described in the Supporting Information.

For the two-state model involving the $X^3\Sigma_g^-$ and $b^1\Sigma_g^+$ states of O_2, different types of simulations were carried out: (a) 2 ns simulations with both oxygen atoms inside bulk ASW; (b) five 8 ns simulations with the two oxygen atoms on the surface and rebinding into the $^3\Sigma_g^-$ state initially; (c) 2200 simulations run for 400 ps on the surface (1100 recombining into the $^3\Sigma_g^-$ state and 1100 into the $^1\Sigma_g^+$ state).

For the analysis, two quantities are considered: the average time between two consecutive transitions τ_c and the total crossing time from the first to the last transition, τ_{LZ}. Per definition, after τ_{LZ} no further transitions between the states are observed. For simulations inside ASW bulk (see Figure S1), O_2 is formed in its $b^1\Sigma_g^+$ state after ∼750 ps and stabilized after two scattering events at 103.5 and 670 ps, with $\tau_{LZ} = 30$ ps. This time interval is characterized by the abrupt change in the kinetic energy by ∼40 kcal/mol due to the difference in potential energy between the two states (see Figure S2). After this time, no further transitions are encountered during the simulation and the molecule vibrationally relaxes and is stabilized in the $b^1\Sigma_g^+$ state. Similar to simulations on the electronic ground state,[7] vibrational relaxation of the highly excited molecule takes place on the 10−100 ns time scale with full relaxation requiring considerably longer times, well beyond the current simulation times.

Results for a simulation on the ASW surface are shown in Figure 2. Starting from an initial separation of 4.8 Å, recombination occurs after 20 ps with the molecule forming in the $b^1\Sigma_g^+$ state followed by an extended time ($\tau_{LZ} = 70$ ps) during which crossings between the two states occur with final relaxation in the $b^1\Sigma_g^+$ state. The identity of the state is followed explicitly in the simulations. This also allows one to trace the kinetic energy of the O_2 molecule during the time it samples one or the other state; see green and black traces in Figure 2.

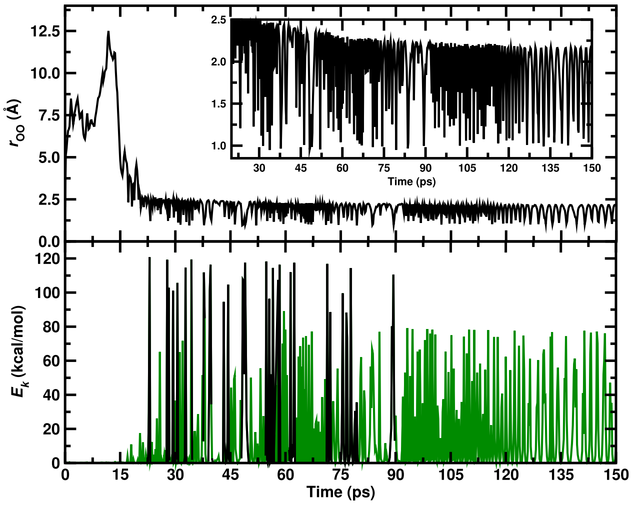

Figure 2. Top: time evolution of the interatomic distance between two oxygen atoms on top of ASW. Recombination occurs after 16 ps. Bottom: kinetic energy for O_2 system during 150 ps. Formation of the bound state is reflected by the sharp increase of the kinetic energy of the two oxygen atoms at 16 ps. Transitions between the $X^3\Sigma_g^-$ (black) and $b^1\Sigma_g^+$ (green) are observed between 17 and 100 ps. After this, the system localizes on the $b^1\Sigma_g^+$ state. The average over the green and black traces also reflects the different binding energy (38.7 kcal/mol) for the two electronic states (see Figure S2).

Five simulations were run by rebinding into the $b^1\Sigma_g^+$ state for a total of 8 ns to determine whether further transitions are observed after the molecule relaxes below the crossing point after τ_{LZ}. Three trajectories lead to bound O_2, one in the $X^3\Sigma_g^-$ and the other two in the $b^1\Sigma_g^+$ state, and transitions occur with a sharp distribution peaked at the crossing point (2.209 Å). In the other two simulations, the two atoms do not recombine within 8 ns but rather continue to sample an unbound state. The time interval between the first and last transition (i.e., τ_{LZ}) and between two single transitions (i.e., τ_c) is consistent with results in Figure S3 discussed further below. The time series of two of those simulations are reported in Figure S4.

Next, the results from the 2200 rebinding simulations on the surface are analyzed. Initially, the two O atoms are separated by 6.07 ± 2.13 Å. For ∼80% of the simulations, O_2 is formed, consistent with previous work.[6] Half of these simulations initially recombine into the $X^3\Sigma_g^-$ state and the other half into $b^1\Sigma_g^+$. The average time interval between two consecutive transitions ($\langle\tau_c\rangle$) is 47.4 ± 11.7 fs, for an average number of 1224 ± 537 transitions per trajectory, independent of the initial state into which rebinding takes place. The distribution $p(\tau_c)$ is shown in Figure S3. On average, one crossing every two vibrational periods is observed before sufficient vibrational energy has been dissipated and the crossing point cannot be reached anymore energetically. After this, vibrational relaxation on the final electronic state takes place on considerably longer time scales.

Out of the 1100 trajectories which recombine into one of the two electronic states, 903 and 859 simulations localize either in $X^3\Sigma_g^-$ or in $b^1\Sigma_g^+$ (see Figure 3). The distribution of O−O separations r at which changes in the electronic state occur is shown in Figure S5A. From all 2200 trajectories, ∼66% (1756 trajectories) recombine into the $^1\Sigma_g^+$ state, while 33% lead to the

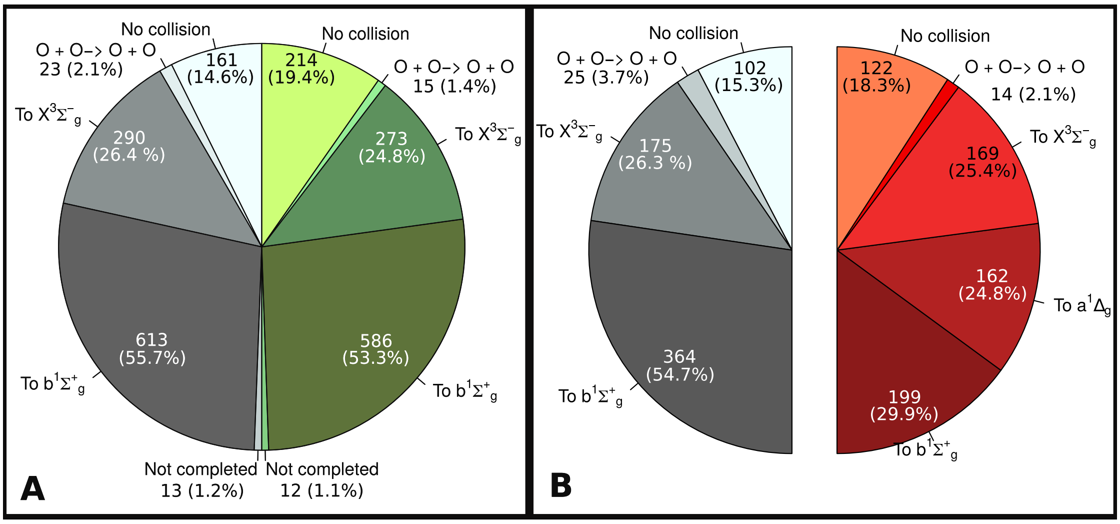

Figure 3. Panel A: Classification of outcome of the simulations: in black, those rebinding into the $X^3\Sigma_g^-$ state; and in green, those initially rebinding into the $b^1\Sigma_g^+$ state. Within 400 ps, 82.1% of them lead to the O_2 recombination. In both sets, the majority of simulations leads to the $b^1\Sigma_g^+$, while ∼1/3 reaches the ground state. Panel B: comparison between the two-state model (left, gray) and the three-state model (right, red). For the two-state model, 666 random simulations from the two-state models were sampled. The population of the $X^3\Sigma_g^-$ is similar for the two models, whereas the population of the $b^1\Sigma_g^+$ state from the two-state model splits into two similar fractions for the three-state model which includes two excited states, $b^1\Sigma_g^+$ and $a^1\Delta_g$. The remaining channels are similarly populated.

electronic ground-state $X^3\Sigma_g^-$. These fractions are independent of the initial condition, i.e., whether initially recombination into the $X^3\Sigma_g^-$ or $b^1\Sigma_g^+$ state occurs, which indicates that the simulations are converged.

Of all simulations, a fraction of 14% and 19% for the $X^3\Sigma_g^-$ and $b^1\Sigma_g^+$ states, respectively, does not lead to recombination and stabilization of O_2. Instead, the two oxygen atoms remain separated on the surface (see Figure 3A). For a small number of trajectories (2% and 1%, respectively) a single collision leads to O_2 with subsequent scattering and dissociation back into two separated oxygen atoms. Finally, there is also a small number of trajectories (13 which initially recombine into $X^3\Sigma_g^-$ and 12 that recombine into $b^1\Sigma_g^+$), which have not settled into a final electronic state after 400 ps, and exploration of the electronic manifold continues on longer time scales.

The two-state model indicates that recombination of two ^{3}P oxygen atoms into O_2 in both electronic states is possible. Furthermore, vibrational relaxation and stabilization in these two states occur on considerably longer time scales than a few hundred picoseconds.[7]

As a more realistic scenario, a three-state model that includes the first three electronic states ($X^3\Sigma_g^-$, $a^1\Delta_g$, and $b^1\Sigma_g^+$) is considered. The transition between the $X^3\Sigma_g^-$ and the $b^1\Sigma_g^+$ state is treated in the same way as for the two-state model. For transitions between $X^3\Sigma_g^-$ and $a^1\Delta_g$, it is noted that the *ab initio* calculations show that the spin−orbit coupling is different from zero only in the coupling region (see Figure S7), whereas no transitions between the $a^1\Delta_g$ and $b^1\Sigma_g^+$ states are considered, because the two potential energy curves do not cross and SOC and NAC matrix elements are zero. Overall, $^3\Sigma_g^- \leftrightarrow {}^1\Delta_g$ and $^3\Sigma_g^- \leftrightarrow {}^1\Sigma_g^+$ are included in this model.

For the three-state model, 666 simulations were run. While O_2 is in one of the two excited singlet states, the only possible transition leads to the ground state. This reflects the fact that the SOC and NAC matrix elements between the two excited states is zero. For a transition from the ground state to both excited states, the more probable of the two is chosen. To determine which transition takes place, $P_{LZ}^{j\to k}$ is evaluated for both transitions and compared with a random number (z). If $P_{LZ}^{j\to k} > z$ for both transitions, the one with the larger value of $P_{LZ}^{j\to k}$ is chosen.

Transitions $^3\Sigma_g^- \to a^1\Delta_g$ occur at smaller interatomic distances (2.09 Å, see Figure S2), compared to an average value of 2.21 Å for the $^3\Sigma_g^- \to b^1\Sigma_g^+$ transition (Figure S5B). Including the $^3\Sigma_g^- \to a^1\Delta_g$ transition in the reaction model leads to an increase of τ_{LZ} to 326.8 ± 226.2 ps (see Figure 4). While the population on the highest $b^1\Sigma_g^+$ state stabilizes after ∼200 ps, transitions between the $X^3\Sigma_g^+$ and $a^1\Delta_g^+$ states continue out to ∼700 ps. Thus, the value of τ_c represents an average over the total population distribution for the two states ($^3\Sigma_g^- \to a^1\Delta_g$, around

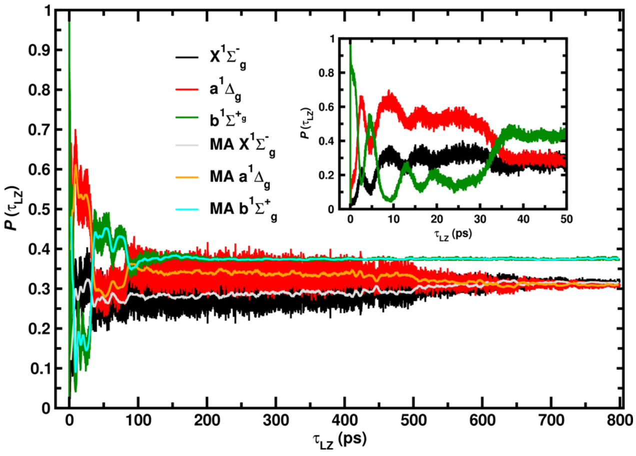

Figure 4. Population of the three electronic states and their moving average (MA) as a function of time (main panel) and a magnification of the first 50 ps in the inset. The zero along the x-axis is defined as the first transition in each of the 222 trajectories that initially rebind into $b^1\Sigma_g^+$. All the population will be initially on the $b^1\Sigma_g^+$ state. As the dynamics proceeds, the population of the $b^1\Sigma_g^+$ state stabilizes at ∼38% within ∼200 ps. The population dynamics for the $X^3\Sigma_g^-$ and $a^1\Delta_g$ states continues until >500 ps.

500 ps; and ${}^3\Sigma_g^- \rightarrow b^1\Sigma_g^+$, 100 ps). Including a third state with a crossing point at shorter O−O separation makes the transition time longer. As a consequence, transitions involving $a^1\Delta_g$ are more prevalent than those involving $b^1\Sigma_g^+$. The $X^3\Sigma_g^- \rightarrow a^1\Delta_g$ transition occurs with a probability of 76%, whereas the $X^3\Sigma_g^- \rightarrow b^1\Sigma_g^+$ occurs for 24% with fluctuations of 22%.

Figure 4 shows how the populations of the three states differ after the first transition. After recombination on the ground state, the first transition leads to $b^1\Sigma_g^+$, common for all simulations. The first 200 ps is characterized by population dynamics between the three states. After this time, population on $b^1\Sigma_g^+$ reaches its equilibrium value. A slower exchange of population occurs between the two lower states (${}^3\Sigma_g^-$ and $a^1\Delta_g$) for a longer period of time (~500 ps) before reaching the equilibrium population.

The final state distributions for the three-state model are summarized in Figure 3B. For the two-state model, population of the $b^1\Sigma_g^+$ state is twice as probable than the ground-state $X^3\Sigma_g^-$. For the three-state model, the $b^1\Sigma_g^+$ state is still most probable, with the $X^3\Sigma_g^-$ and $a^1\Delta_g$ states equally probable. Probabilities for individual events are comparable to those found for the two-state model: the final ground-state population is ~25%, trajectories without collision of atomic oxygen occur for <20%, and the population at the excited state assumes values greater than 50%.

A final question concerns the validity of classical MD simulations to follow the population dynamics between two or multiple states. For this, a wave packet with a translational energy of 2.1 kcal/mol was initialized on the $X^3\Sigma_g^-$ PES and propagated with a time step of 0.125 fs allowing for transitions between the $X^3\Sigma_g^-$ and $b^1\Sigma_g^+$ states. The Fourier transformation of the initial wave function as a function of energy (see Figure S10) shows that an energy range of 0.03−5.0 kcal/mol is covered, which is required to capture the low-energy part of the motion, characteristic for a surface temperature of 10 to 50 K.

The time evolution of the wave function is shown in Figure 5 (black for $X^3\Sigma_g^-$ and green for $b^1\Sigma_g^+$). Initially ($t = 0$, $r = 8.0$ Å), the system is on the $X^3\Sigma_g^-$ surface. The radial grid consists of 1250 evenly spaced points from 0.35 to 26.8 Å and the damping function starts at 15.0 Å. After ~250 fs, the wavepacket has passed the crossing region, splits into two parts, and the amplitude on the $b^1\Sigma_g^+$ PES starts to increase. The distribution of population as a function of time is shown in Figure S9. A significant amount of population transfer from the $X^3\Sigma_g^-$ state to the $b^1\Sigma_g^+$ state occurs up to 380 fs, although some of the WP transfers back to the $X^3\Sigma_g^-$ state due to the coupling of the two states. Since the QM simulations are carried out in the gas phase, only one single collision can be followed. However, in the condensed phase, vibrational relaxation can form a bound O_2 molecule. Multiple crossings are thus possible for the high-lying vibrational states of O_2 molecule.

To account for the recurrences, a kinetic model has been constructed for multiple crossings of the WP (see Figure S11). In the gas phase, the transition probabilities from one state to another starting from any of the states are equal. Hence, the kinetic model for two states leads to a stationary population of 50% on each of the $X^3\Sigma_g^-$ and $b^1\Sigma_g^+$ states. Here, it is worth mentioning that this ratio is 66% on $b^1\Sigma_g^+$ and 34% on $X^3\Sigma_g^-$ obtained from the condensed-phase classical MD simulations. A possible explanation for this observation is the different coupling between the O_2 motion and the surrounding water matrix due to the different curvatures of the potential energy curves for the two electronic states. A similar kinetic model for the three-state model leads to a stationary statistical population of 1/3 on each state, which is close to the classical MD simulations (31%, 31%, and 38% for the $X^3\Sigma_g^-$, $a^1\Delta_g$, and $b^1\Sigma_g^+$ states, respectively).

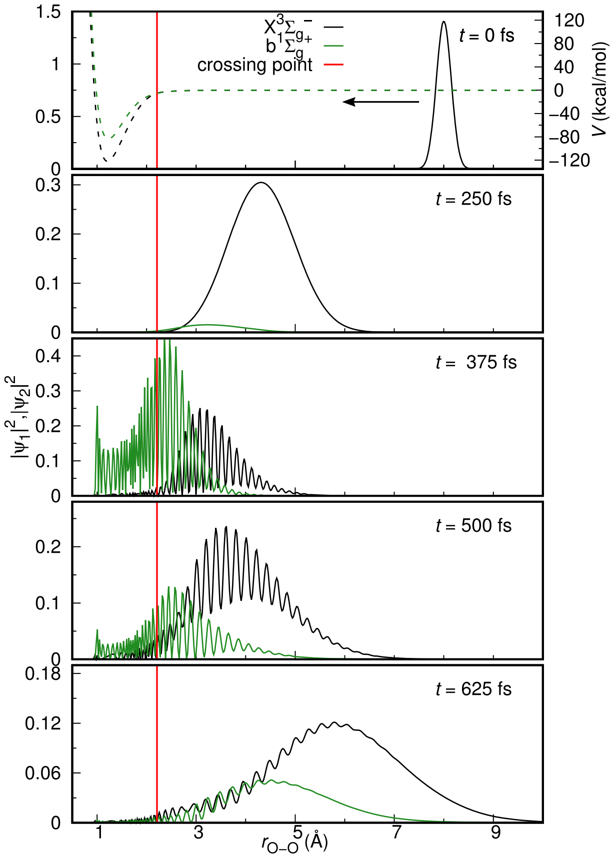

Figure 5. Probability distribution of the wave function $|\Psi|^2$ (solid black and green lines) at different simulation times for both states. The potential energies along the diatomic separation are also plotted by dashed lines for the corresponding states. Crossing point is shown on X axis as red lines.

The present work establishes that upon recombination of ^{3}P atomic oxygen on ASW, molecular oxygen (O_2) in its ground and lower electronically excited states can be formed and stabilized. As the chemical reactivity of triplet and singlet O_2 with carbon- and hydrogen-containing compounds differs substantially,[4] the presence of singlet ($a^1\Delta_g$ and $b^1\Sigma_g^+$) oxygen is expected to influence and modify the chemical evolution of cold and noctilucent[33,34] clouds. It should be emphasized that desorption of O_2 after formation through association of atomic oxygen, although energetically feasible, was not observed, which is consistent with earlier work.[7]

For singlet oxygen, the radiative decay lifetimes have been determined in the gas phase. They range from ~1 min to ~100 min for the $a^1\Delta_g$ and $b^1\Sigma_g$ states and also depend on the vibrational level.[35,36] On the other hand, the radiationless conversion of the $b^1\Sigma_g$ state to the $a^1\Delta_g$ state has been determined to occur with an interconversion rate of ~10^9 M^{-1} s^{-1} for water.[37] Nevertheless, the reactivity of $b^1\Sigma_g$ O_2 has been studied[38] for H, H_2, H_2O, and CH_4. Furthermore, the reactivity of the $b^1\Sigma_g$ state has also been considered in collisions with methylene (CH_2) in its X^3B_1 state.[2] Thus, the actual fraction available for chemical processes will depend on how the radiative and nonradiative lifetimes change when O_2 is adsorbed on ASW.

https://dx.doi.org/10.1021/acs.jpclett.0c00130
J. Phys. Chem. Lett. 2020, 11, 2171−2176

Because the reactivity of the $a^1\Delta_g$ and $b^1\Sigma_g^+$ states can be considerably larger than that of the $X^3\Sigma_g^-$ ground state depending on the reaction partner, including electronically excited states of O_2 (and other molecules formed on ASW) will be important for a comprehensive modeling and understanding of the chemistry of interstellar matter under such conditions. Experimental and computational studies between singlet excited O_2 and typical ASW-adsorbates including H, O, or H_2 will provide valuable insights into the reaction pathways, their rates, and the final state species composition. Computational studies in particular will benefit from more recent developments such as neural network-based interaction potentials for studying chemical reactions.[39−41]

■ ASSOCIATED CONTENT

Supporting Information

The Supporting Information is available free of charge at https://pubs.acs.org/doi/10.1021/acs.jpclett.0c00130.

Methods section (PDF)

■ AUTHOR INFORMATION

Corresponding Author

Markus Meuwly − *Department of Chemistry, University of Basel CH-4056 Basel, Switzerland;* orcid.org/0000-0001-7930-8806; Email: m.meuwly@unibas.ch

Authors

Marco Pezzella − *Department of Chemistry, University of Basel CH-4056 Basel, Switzerland*

Debasish Koner − *Department of Chemistry, University of Basel CH-4056 Basel, Switzerland*

Complete contact information is available at: https://pubs.acs.org/10.1021/acs.jpclett.0c00130

Notes

The authors declare no competing financial interest.

■ ACKNOWLEDGMENTS

This work was supported by the Swiss National Science Foundation through grants 200021-117810, 200020-188724, and the NCCR MUST.

■ REFERENCES

(1) Song, X.; Fanelli, M. G.; Cook, J. M.; Bai, F.; Parish, C. A. Mechanisms for the Reaction of Thiophene and Methylthiophene with Singlet and Triplet Molecular Oxygen. *J. Phys. Chem. A* **2012**, *116*, 4934−4946.

(2) Lakshmanan, S.; Pratihar, S.; Hase, W. L. Direct Dynamics Simulations of the CH_2 + O_2 Reaction on the Ground- and Excited-State Singlet Surfaces. *J. Phys. Chem. A* **2019**, *123*, 4360−4369.

(3) Chukalovsky, A. A.; Klopovsky, K. S.; Liberman, M. A.; Mankelevich, Y. A.; Popov, N. A.; Proshina, O. V.; Rakhimova, T. V. Study of Singlet Delta Oxygen $O_2(1\Delta_g)$ Impact on H_2−O_2 Mixture Ignition in Flow Reactor: 2D Modeling. *Combust. Sci. Technol.* **2012**, *184*, 1768−1786.

(4) Starik, A. M.; Loukhovitski, B. I.; Sharipov, A. S.; Titova, N. S. Physics and chemistry of the influence of excited molecules on combustion enhancement. *Philos. Trans. R. Soc., A* **2015**, *373*, 20140341.

(5) Chukalovsky, A. A.; Klopovsky, K. S.; Palov, A. P.; Mankelevich, Y. A.; Rakhimova, T. V. Reaction of hydrogen atoms with singlet delta oxygen ($O_2(a^1\Delta_g)$). Is everything completely clear? *J. Phys. D: Appl. Phys.* **2016**, *49*, 485202.

(6) Pezzella, M.; Unke, O. T.; Meuwly, M. Molecular Oxygen Formation in Interstellar Ices Does Not Require Tunneling. *J. Phys. Chem. Lett.* **2018**, *9*, 1822−1826.

(7) Pezzella, M.; Meuwly, M. O_2 formation in cold environments. *Phys. Chem. Chem. Phys.* **2019**, *21*, 6247−6255.

(8) Tielens, A. G. G. M.; Hagen, W. Model Calculations of the Molecular Composition of Interstellar Grain Mantles. *Astron. Astrophys.* **1982**, *114*, 245−260.

(9) Nguyen, T. L.; Stanton, J. F. Ab Initio Thermal Rate Calculations of HO + HO = O(P-3) + H2O Reaction and Isotopologues. *J. Phys. Chem. A* **2013**, *117*, 2678−2686.

(10) Chou, S.-L.; Lo, J.-I.; Peng, Y.-C.; Lu, H.-C.; Cheng, B.-M.; Ogilvie, J. F. Photolysis of O_2 dispersed in solid neon with far-ultraviolet radiation. *Phys. Chem. Chem. Phys.* **2018**, *20*, 7730−7738.

(11) Farooq, Z.; Chestakov, D. A.; Yan, B.; Groenenboom, G. C.; van der Zande, W. J.; Parker, D. H. Photodissociation of singlet oxygen in the UV region. *Phys. Chem. Chem. Phys.* **2014**, *16*, 3305−3316.

(12) Jongma, R. T.; Shi, S.; Wodtke, A. M. Electronic nonadiabaticity in highly vibrationally excited $O_2(X^3\Sigma_g^-)$: Spin-orbit coupling between $X^3\Sigma_g^-$ and.$^1\Sigma_g^+$. *J. Chem. Phys.* **1999**, *111*, 2588−2594.

(13) Hidemori, T.; Akai, N.; Kawai, A.; Shibuya, K. Intensity Enhancement of Weak O_2 $a^1\Delta_g \rightarrow X^3\Sigma_g^-$ Emission at 1270 nm by Collisions with Foreign Gases. *J. Phys. Chem. A* **2012**, *116*, 2032−2038.

(14) Minaev, B. F.; Yashchuk, L. B. Spin-orbit coupling in oxygen near the dissociation limit. *Opt. Spectrosc.* **2003**, *95*, 553−559.

(15) Dayou, F.; Hernández, M. I.; Campos-Martínez, J.; Hernández-Lamoneda, R. Spin-orbit coupling in $O_2(\nu)$+O_2 collisions: I. Electronic structure calculations on dimer states involving the $X^3\Sigma_g^-$, $a^1\Delta_g^+$, and $b^1\Sigma_g^+$ states of O2. *J. Chem. Phys.* **2005**, *123*, 074311.

(16) Angell, C. A. Amorphous Water. *Annu. Rev. Phys. Chem.* **2004**, *55*, 559−583.

(17) Burke, D. J.; Brown, W. A. Ice in space: surface science investigations of the thermal desorption of model interstellar ices on dust grain analogue surfaces. *Phys. Chem. Chem. Phys.* **2010**, *12*, 5947−5969.

(18) Bossa, J.-B.; Isokoski, K.; Paardekooper, D. M.; Bonnin, M.; van der Linden, E. P.; Triemstra, T.; Cazaux, S.; Tielens, A. G. G. M.; Linnartz, H. Porosity measurements of interstellar ice mixtures using optical laser interference and extended effective medium approximations. *Astron. Astrophys.* **2014**, *561*, A136.

(19) Bossa, J.-B.; Maté, B.; Fransen, C.; Cazaux, S.; Pilling, S.; Rocha, W. R. M.; Ortigoso, J.; Linnartz, H. Porosity and band-strength measurements of multi-phase composite ices. *Astrophys. J.* **2015**, *814*, 47.

(20) Cazaux, S.; Bossa, J.-B.; Linnartz, H.; Tielens, A. G. G. M. Pore evolution in interstellar ice analogues - Simulating the effects of temperature increase. *Astron. Astrophys.* **2015**, *573*, A16.

(21) Ioppolo, S.; Cuppen, H. M.; Linnartz, H. Surface formation routes of interstellar molecules: hydrogenation reactions in simple ices. *Rend. Lincei.-Sci. Fis. Nat.* **2011**, *22*, 211.

(22) Romanzin, C.; Ioppolo, S.; Cuppen, H. M.; van Dishoeck, E. F.; Linnartz, H. Water formation by surface O_3 hydrogenation. *J. Chem. Phys.* **2011**, *134*, 084504.

(23) Chaabouni, H.; Minissale, M.; Manicò, G.; Congiu, E.; Noble, J. A.; Baouche, S.; Accolla, M.; Lemaire, J. L.; Pirronello, V.; Dulieu, F. Water formation through O_2 + D pathway on cold silicate and amorphous water ice surfaces of interstellar interest. *J. Chem. Phys.* **2012**, *137*, 234706.

(24) Minissale, M.; Congiu, E.; Baouche, S.; Chaabouni, H.; Moudens, A.; Dulieu, F.; Accolla, M.; Cazaux, S.; Manico, G.; Pirronello, V. Quantum Tunneling of Oxygen Atoms on Very Cold Surfaces. *Phys. Rev. Lett.* **2013**, *111*, 053201.

(25) Dulieu, F.; Minissale, M.; Bockelée-Morvan, D. Production of O_2 through dismutation of $H2O_2$ during water ice desorption: a key to understanding comet O_2 abundances. *Astron. Astrophys.* **2017**, *597*, A56.

(26) Hama, T.; Watanabe, N. Surface Processes on Interstellar Amorphous Solid Water: Adsorption, Diffusion, Tunneling Reactions, and Nuclear-Spin Conversion. *Chem. Rev.* **2013**, *113*, 8783−8839.

(27) Minissale, M.; Congiu, E.; Manicò, G.; Pirronello, V.; Dulieu, F. CO_2 formation on interstellar dust grains: a detailed study of the barrier of the CO channel. *Astron. Astrophys.* **2013**, *559*, A49.

(28) Minissale, M.; Moudens, A.; Baouche, S.; Chaabouni, H.; Dulieu, F. Hydrogenation of CO-bearing species on grains: unexpected chemical desorption of CO. *Mon. Not. R. Astron. Soc.* **2016**, *458*, 2953−2961.

(29) Minissale, M.; Fedoseev, G.; Congiu, E.; Ioppolo, S.; Dulieu, F.; Linnartz, H. Solid state chemistry of nitrogen oxides − Part I: surface consumption of NO. *Phys. Chem. Chem. Phys.* **2014**, *16*, 8257−8269.

(30) Minissale, M.; Congiu, E.; Dulieu, F. Direct measurement of desorption and diffusion energies of O and N atoms physisorbed on amorphous surfaces. *Astron. Astrophys.* **2016**, *585*, A146.

(31) Minissale, M.; Nguyen, T.; Dulieu, F. Experimental study of the penetration of oxygen and deuterium atoms into porous water ice. *Astron. Astrophys.* **2019**, *622*, A148.

(32) Nagy, T.; Yosa Reyes, J.; Meuwly, M. Multi-Surface Adiabatic Reactive Molecular Dynamics. *J. Chem. Theory Comput.* **2014**, *10*, 1366−1375.

(33) Murray, B. J.; Jensen, E. J. Homogeneous nucleation of amorphous solid water particles in the upper mesosphere. *J. Atmos. Sol.-Terr. Phys.* **2010**, *72*, 51−61.

(34) Murray, B. J.; Malkin, T. L.; Salzmann, C. G. The crystal structure of ice under mesospheric conditions. *J. Atmos. Sol.-Terr. Phys.* **2015**, *127*, 78−82.

(35) Gamache, R.; Goldman, A.; Rothman, L. Improved spectral parameters for the three most abundant isotopomers of the oxygen molecule. *J. Quant. Spectrosc. Radiat. Transfer* **1998**, *59*, 495−509.

(36) Newman, S.; Lane, I.; Orr-Ewing, A.; Newnham, D.; Ballard, J. Integrated absorption intensity and Einstein coefficients for the O_2 $a^1\Delta_g$-$X^3\Sigma_g^-$ (0,0) transition: A comparison of cavity ringdown and high resolution Fourier transform spectroscopy with a long-path absorption cell. *J. Chem. Phys.* **1999**, *110*, 10749−10757.

(37) Schmidt, R.; Bodesheim, M. Radiationless deactivation of the second excited singlet state $^1\Sigma_g^+$ of O2 in solution. *J. Phys. Chem. A* **1998**, *102*, 4769−4774.

(38) Starik, A.; Sharipov, A. Theoretical analysis of reaction kinetics with singlet oxygen molecules. *Phys. Chem. Chem. Phys.* **2011**, *13*, 16424−16436.

(39) Unke, O. T.; Meuwly, M. PhysNet: a neural network for predicting energies, forces, dipole moments and partial charges. *J. Chem. Theory Comput.* **2019**, *15*, 3678−3693.

(40) del Cueto, M.; Zhou, X.; Zhou, L.; Zhang, Y.; Jiang, B.; Guo, H. New Perspectives on CO2-Pt(111) Interaction with a High-Dimensional Neural Network Potential Energy Surface. *J. Phys. Chem. C* **2020**, 1 DOI: 10.1021/acs.jpcc.9b10883.

(41) Unke, O. T.; Koner, D.; Patra, S.; Käser, S.; Meuwly, M. High-Dimensional Potential Energy Surfaces for Molecular Simulations. *arXiv* (physics-chem-ph), October 7, **2019**, 1910.03044, ver. 1.

Supplementary Information: Formation and Stabilization of Ground and Excited State Singlet O_2 upon Recombination of ^3P Oxygen on Amorphous Solid Water

Marco Pezzella, Debasish Koner and Markus Meuwly*

Department of Chemistry, University of Basel, Klingelbergstrasse 80, CH-4056 Basel, Switzerland.

E-mail: m.meuwly@unibas.ch

S1 Methods

The simulation system consists of an equilibrated cubic box of amorphous solid water with dimension $31 \times 31 \times 31$ Å^3 containing 1000 TIP3P[1] water molecules, and two oxygen atoms, see Figure 1. The time step in all simulations was $\Delta t = 0.1$ fs which ensures conservation of total energy also during the recombination dynamics. All bonds involving hydrogen atoms were constrained using SHAKE[2] and the non-bonded cutoff was at 13 Å. Initial conditions were generated from an existing, equilibrated ASW structure[3,4] by adding two oxygen atoms, minimizing the system, heating it for 5 ps to 50 K and equilibrating for 10 ps. Data (energies, coordinates and velocities) are saved every 1,000 steps. This was followed by production simulations of various lengths, as indicated throughout this work.

All simulations are performed using the CHARMM program[5] modified for reactive MD simulations[6,7] and potential energy surfaces for O_2 based on reproducing kernels.[8,9] For treating nonadiabatic transitions a surface hopping scheme based on the Landau Zener formalism is used, see below. Three electronic states for O_2 are considered: the ground state ($X^3\Sigma_g^-$) and the next two electronically excited states ($a^1\Delta_g$ and $b^1\Sigma_g^+$) based on earlier calculations at the MRCI/aug-cc-pVTZ level of theory[10] which were accurately represented as a reproducing kernel Hilbert space (see Figure S2a).[8,9] The spin orbit coupling (SOC) matrix elements involving the $^3\Sigma_{\rm g}^-$ and $^1\Sigma_{\rm g}^+$ states were recomputed at the MRCI/aug-cc-pVTZ level of theory and can be compared with previous works at the CI/cc-pVTZ[11] and CASSCF/CASPT2/5s4p3d2f atomic natural orbital basis set[12] levels of theory, see Figure S2b. Because the $a^1\Delta_g$ and the $b^1\Sigma_g^+$ states do not cross (see inset Figure S2) and the nonadiabatic coupling (NAC) matrix element between the two states is zero, transitions between these two states will not be included.

In the gas phase all transitions between the $^3\Sigma_g^-$, $^1\Delta_g$ and $^1\Sigma_g^+$ states are strictly forbidden. Transitions from the ground state to the two excited states are spin-forbidden[13] and Laporte rule,[14] because all states have g symmetry. Due to the second rule, transitions between $a^1\Delta_g$ and $b^1\Sigma_g^+$ are also forbidden. However, because the reaction occurs on the ASW surface, no symmetry rules apply for allowed transitions. This is similar to the fact that $Q-$branches for diatomics in liquids and high pressure fluids become allowed due to symmetry breaking induced by the environment,[15] whereas such $\Delta J = 0$ transitions are forbidden in free space.[16]

For the nonadiabatic transitions the trajectory surface hopping (TSH) method[17] within the Landau-Zener (LZ)[18,19] formalism was used. The implementation follows earlier work[20,21] for which the transition probability $P_{\rm LZ}^{i \to j}$ from state j to k is

$$P_{\rm LZ}^{j \to k} = exp\left(-2\pi \frac{(\Delta H_{jk})^2}{\hbar |\dot{\vec{R}} \cdot \vec{\nabla}(\Delta E_{jk})|} \right) \tag{S1}$$

The transition probability depends on the gradient of the energy difference $\vec{\nabla}(\Delta E_{jk})$ between states j and k, the coupling ΔH_{jk}, which is the conformationally dependent spin orbit matrix element, and the velocity of the center of mass $\dot{\vec{R}}$ at the transition.

The trajectories are started from a given initial electronic state j and the electronic state is followed along the trajectory. Close to a crossing between the present state j and a neighboring state k, $P_{\mathrm{LZ}}^{j\to k}$ is calculated and compared with a random number $\xi \in [0,1]$. If $P_{\mathrm{LZ}}^{j\to k} \geq \xi$ a transition from state j to state k occurs. To ensure conservation of the total energy and total angular momentum, a momentum correction

$$\mathbf{p}' = \mathbf{p} - \hat{\mathbf{n}}\frac{\hat{\mathbf{n}}\mathbf{M}^{-1}\mathbf{p}}{\hat{\mathbf{n}}\mathbf{M}^{-1}\hat{\mathbf{n}}}\left[1 - \left(1 - 2\Delta\mathrm{E}\frac{\hat{\mathbf{n}}\mathbf{M}^{-1}\hat{\mathbf{n}}}{(\hat{\mathbf{n}}\mathbf{M}^{-1}\mathbf{p})^2}\right)^{1/2}\right], \tag{S2}$$

is applied[22] where $\mathbf{p}$ and $\mathbf{p}'$ are the momenta before and after the hop and $\mathbf{M}$ is the mass matrix and $\hat{\mathbf{n}}$ is the unit vector along the velocity direction.

In order to assess the role of quantum effects on the nuclear dynamics, time-dependent wave packet (WP) simulations were carried out for the two state model (see below), including the $X^3\Sigma_g^-$ and $b^1\Sigma_g^+$ states. For this, the time-dependent Schrödinger equation is[23–25]

$$\begin{pmatrix} \psi_1(r;t) \\ \psi_2(r;t) \end{pmatrix} = e^{-iHt/\hbar} \begin{pmatrix} \psi_1(r;0) \\ \psi_2(r;0) \end{pmatrix} \tag{S3}$$

where the Hamiltonian H is

$$\hat{H} = -\frac{\hbar^2}{2\mu}\frac{\partial^2}{\partial r^2} + \begin{pmatrix} V_{11}(r) & V_{12}(r) \\ V_{21}(r) & V_{22}(r) \end{pmatrix} \tag{S4}$$

where μ is the reduced mass of the system, V_{11}, V_{22} are the diabatic potential energies and $V_{12} = V_{21}$ is the geometry-dependent coupling matrix element between two states.

The initial wave packet is a (complex-valued) Gaussian function

$$\psi_0(r) = (1/2\pi\sigma^2)^{1/4} \exp[-1/(2\sigma^2)(r - r_0)^2) \exp[ip_0(r - r_0)], \tag{S5}$$

where σ is the width parameter, r_0 and p_0 are the initial position and momentum of the wavepacket, respectively. The time-dependent wave function is propagated[26] on the coupled $X^3\Sigma_g^+$ and $b^1\Sigma_g^+$ potentials using the split-operator method.[27] Fast Fourier transformation (FFT) is used to calculate the double differentiation $\frac{\partial^2}{\partial r^2}$ of the wave function. A sine damping function is multiplied to the wave function at the grid boundary to avoid reflection. The state population can then be calculated as the expectation value of the projection operator[25]

$$P_2(t) = \left\langle \begin{pmatrix} \psi_1(x;t) \\ \psi_2(x;t) \end{pmatrix} \middle| \begin{pmatrix} 0 & 0 \\ 0 & 1 \end{pmatrix} \middle| \begin{pmatrix} \psi_1(x;t) \\ \psi_2(x;t) \end{pmatrix} \right\rangle \tag{S6}$$

and $P_1(t) = 1 - P_2(t)$.

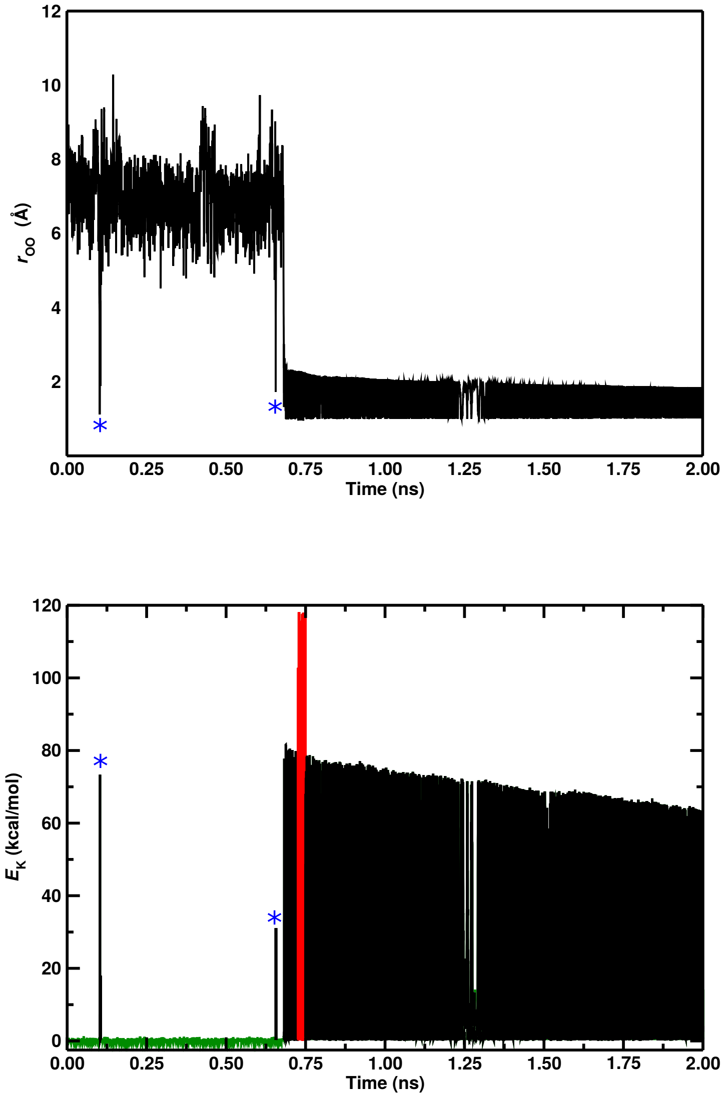

Figure S1: Top panel: Time evolution of the interatomic distance between two oxygen atoms for the simulation inside the cavity. The first time that the bound state is reached, at 103.5 ps, it suddenly dissociates due the collision of the molecule with one of the TIP3P hydrogen water. A similar situation happens near the formation time (around 670 ps). Both are shown in the graph by a blue star. Bottom panel: kinetic energy for the dioxygen system. The bound state can be recognized by the peak in kinetic energy at 103.5 ps and at 670 ps (shown with a blue star). The transition between $^1\Sigma_g^+$ and $^3\Sigma_g^+$ is observed between 720 ps and 750 ps and is characterized by the $\sim$40 kcal/mol energy increase. This energy corresponds to the energy difference between the two states. A color code here is applied in order to distinguish the three different states: the green line represents the unbound state, the red one the time interval where the triplet region is explored and the black is used when O_2 lays in the singlet state.

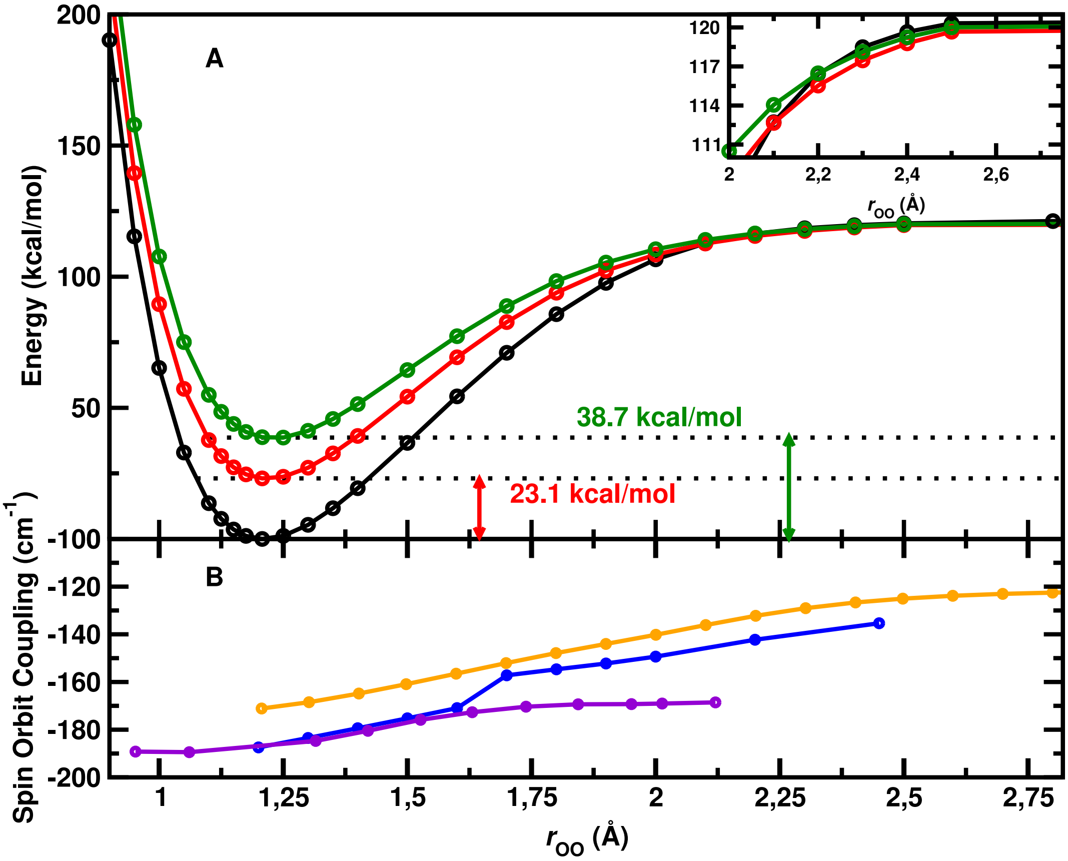

Figure S2: Panel A: Potential energy curves for the $X^3\Sigma_g^-$, $a^1\Delta_g$ and the $b^1\Sigma_g^+$ states (black, red and green, respectively) with the crossing region enlarged in the inset. Panel B: SOC between the $^3\Sigma_g^-$ and $^1\Sigma_g^+$ states from the literature (blue[11] and violet[12]) and the SOC calculated in the present work (orange). The differences can be explained by the difference in methodologies and basis set between used in the different calculations. Asymptotically, the SOC approaches twice the value of O ^3P, which is 74.182 cm^{-1} for a single oxygen atom in its ground state.

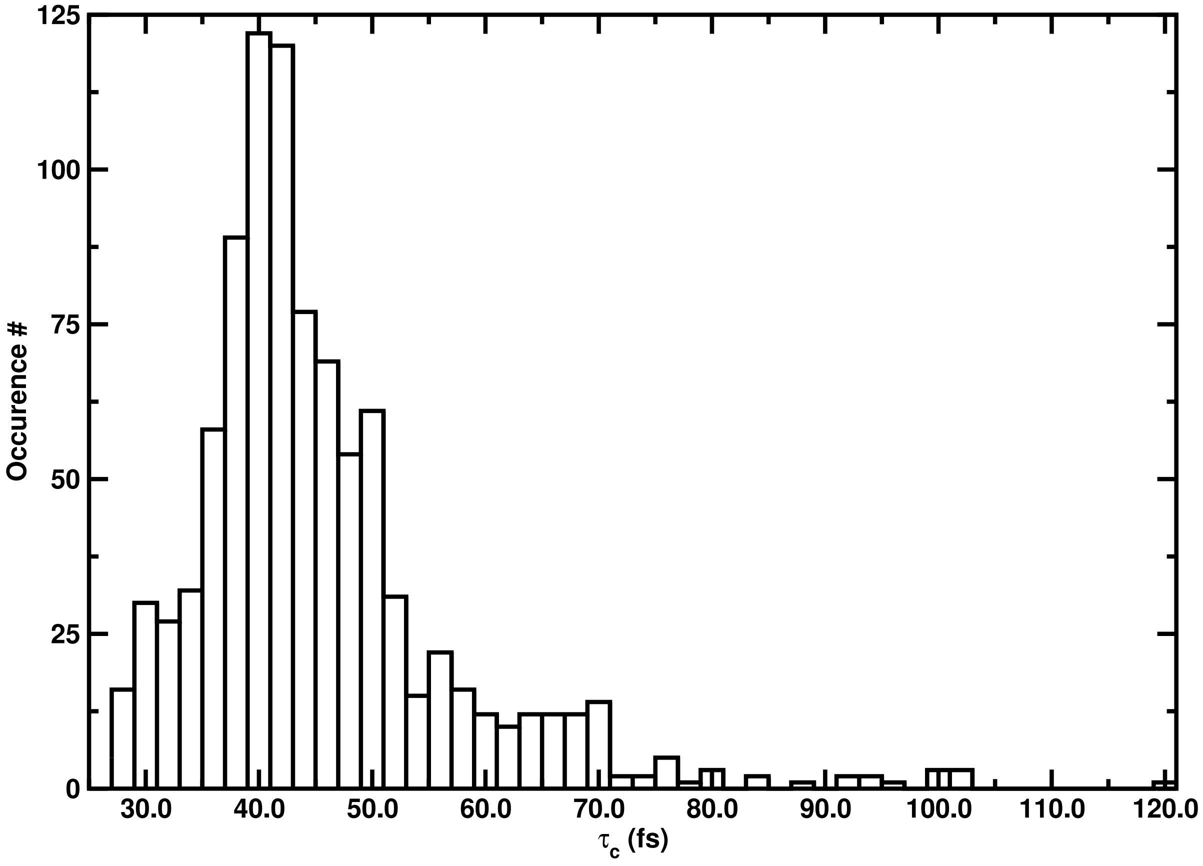

Figure S3: Probability distribution for τ_c. The average is 47.4 ± 11.7 fs. This corresponds to approximately one transition every two vibrational periods.

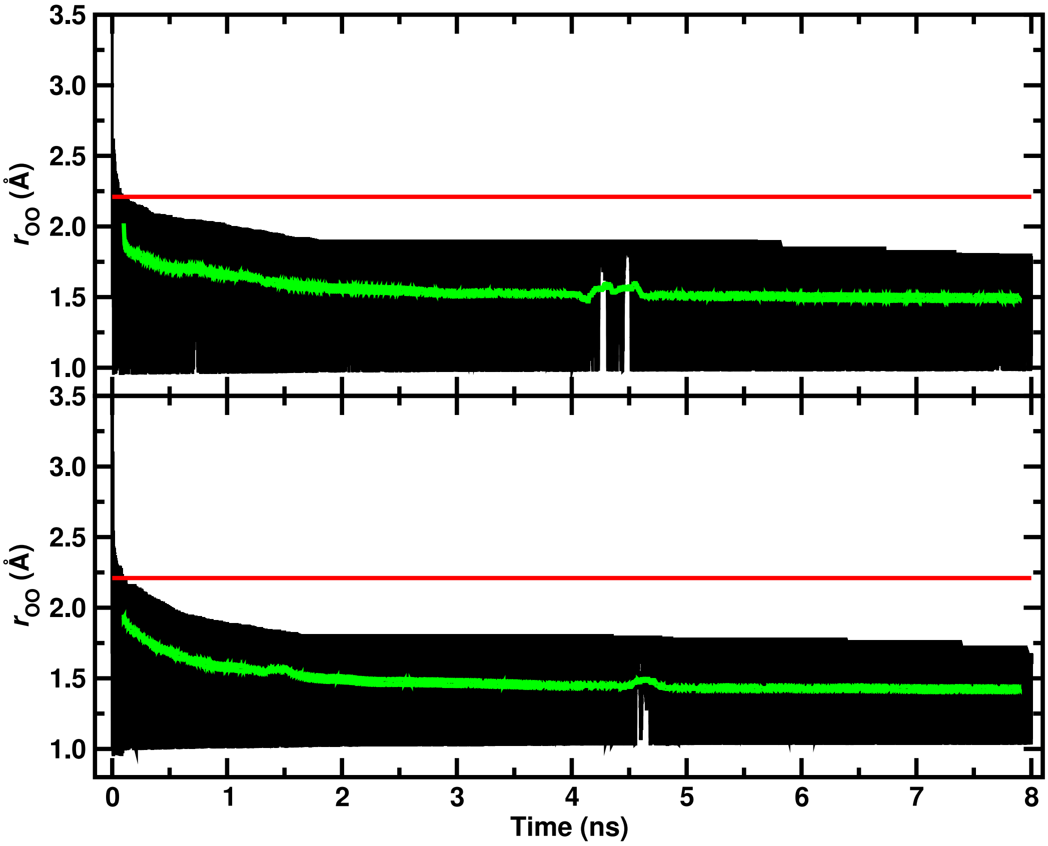

Figure S4: Relaxation of the O_2 bond length during two independent 8 ns simulation with the two states models for two simulations. Transitions are observed only in the initial steps of the simulations corresponding to the overlap between the time series and the crossing point between the two states (2.209 Å, red line). The green line represents the moving average of the time series over 0.2 ps time interval. The signatures between 4 ns and 4.5 ns are collisional re-excitation of the diatomic due to collisions with the surface.

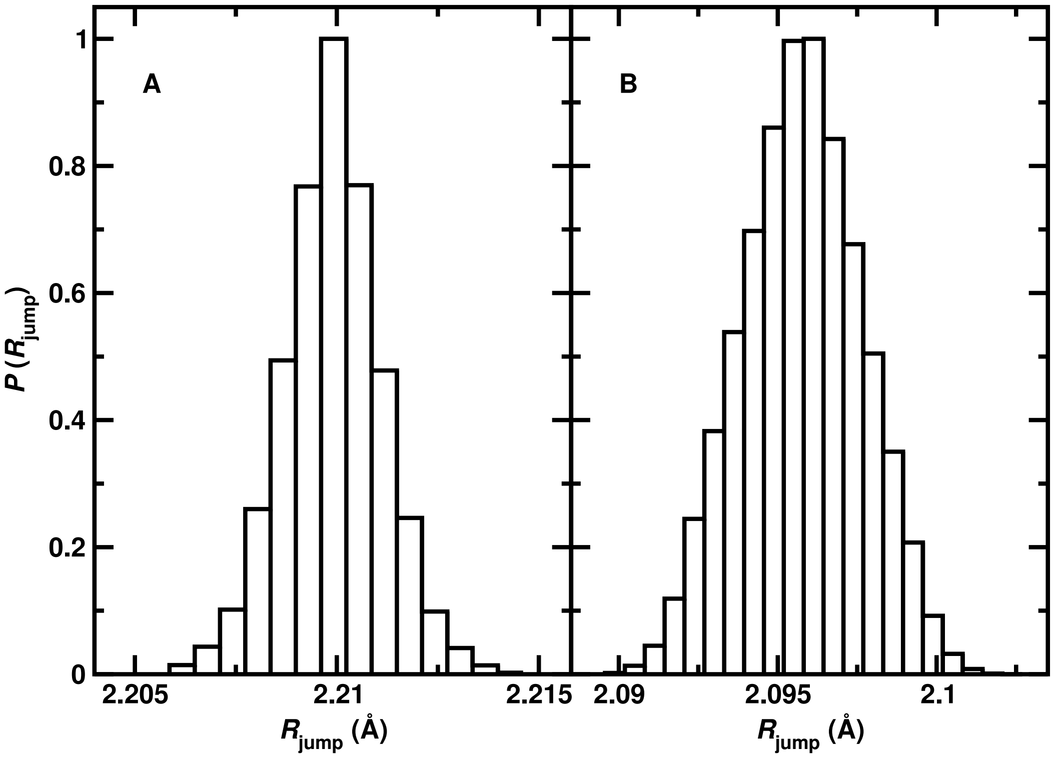

Figure S5: Probability distributions of the interatomic distance within the transition between the $a^1\Delta_g^-$ and the $X^3\Sigma_g^-$ (B), $\mathrm{b}^3\Sigma_g^-$ and the $X^3\Sigma_g^-$ (A) for an ensemble of simulations.. In the first case the interval is localized around 2.097 ± 0.003 Å and in the second case around 2.209 ± 0.003 Å.

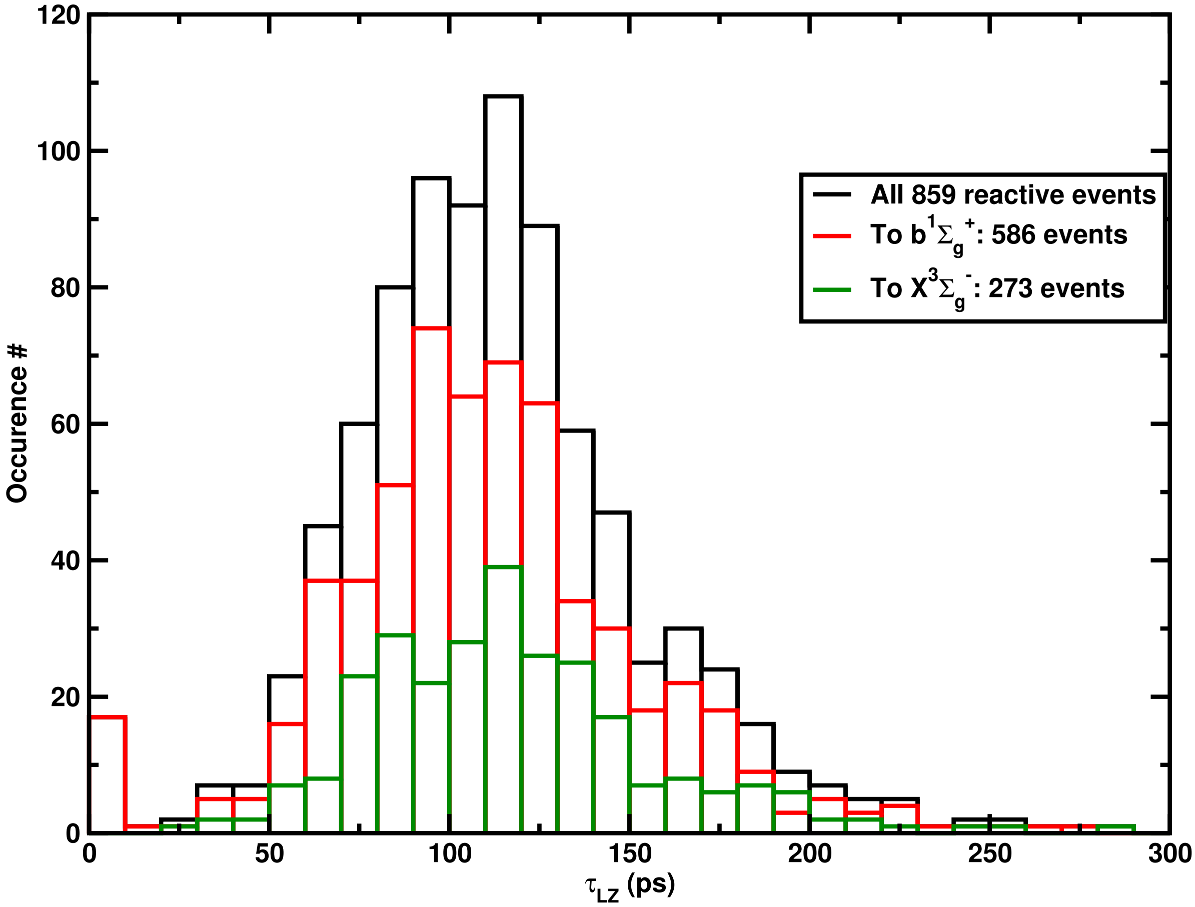

Figure S6: The time distribution for the three τ_{LZ} for the O_2 recombination from $b^3\Sigma_g^-$, in red simulations that from the initial $X^3\Sigma_g^-$state leads to final $b^1\Sigma_g^+$ state, in green simulations that have $X^3\Sigma_g^-$ as initial and final state The and in black the sum of the two previous sets.

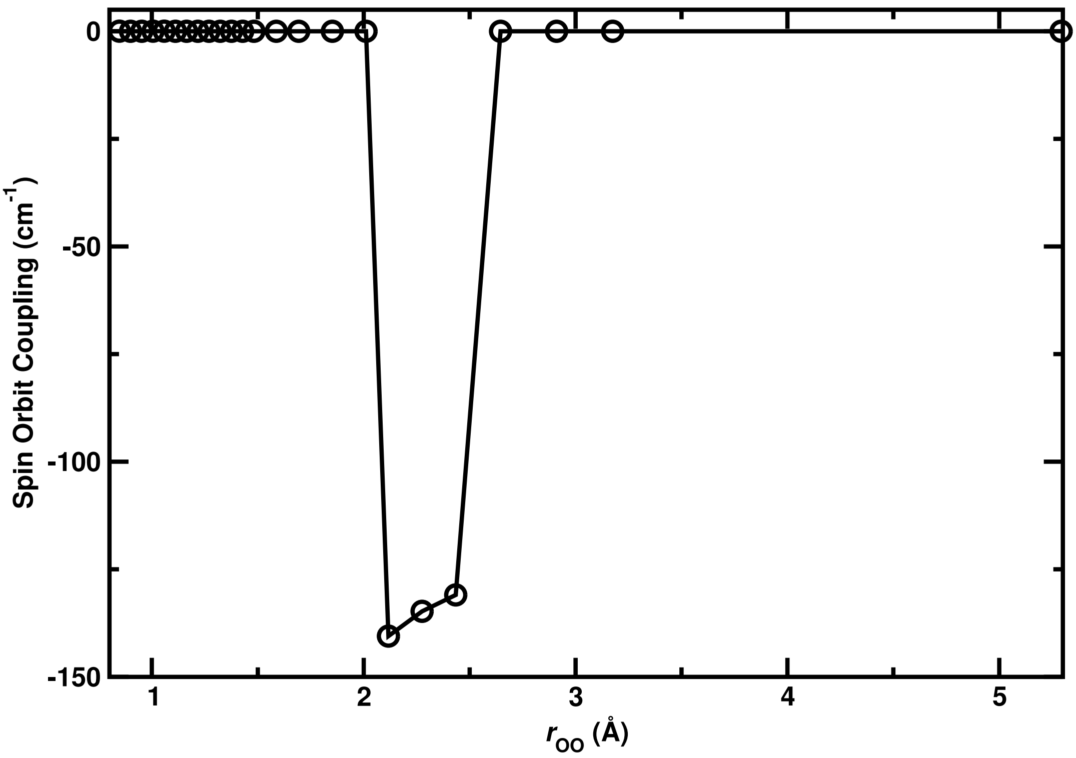

Figure S7: Computed spin orbit coupling between $X^3\Sigma_g^-$and $a^1\Delta_g$. The function is discontinuous, with values different from 0, only in the crossing regions. The two atoms are in the ^{3}P state.

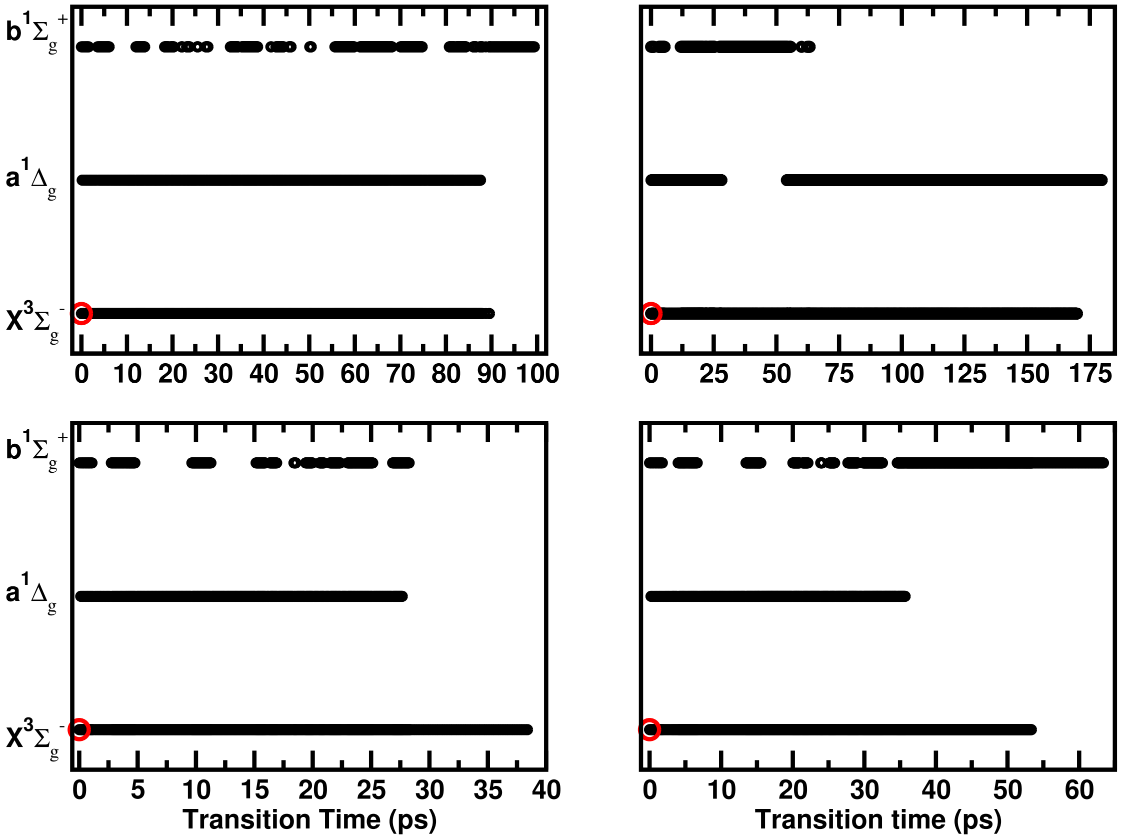

Figure S8: State dynamics for four different simulations during the τ_{LZ} interval. All simulations start from the $X^3\Sigma_g^-$ state (red dot).

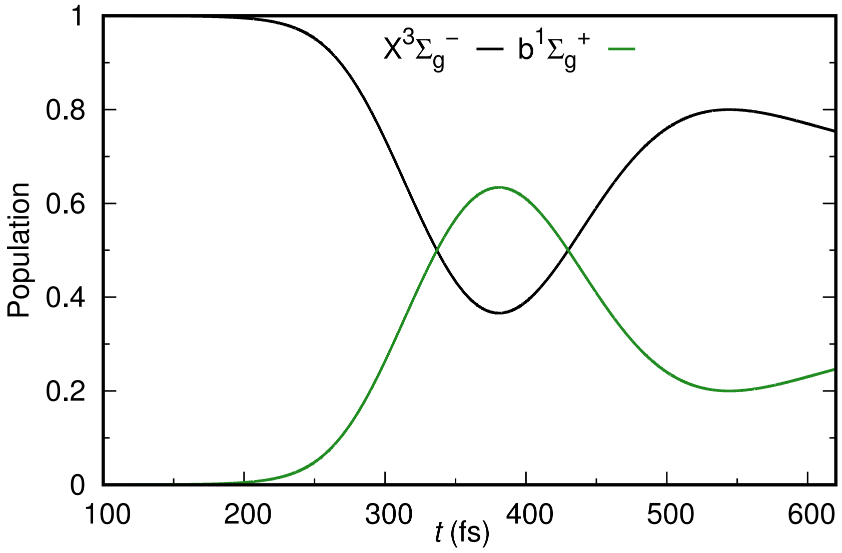

Figure S9: Population on each state as a function of time.

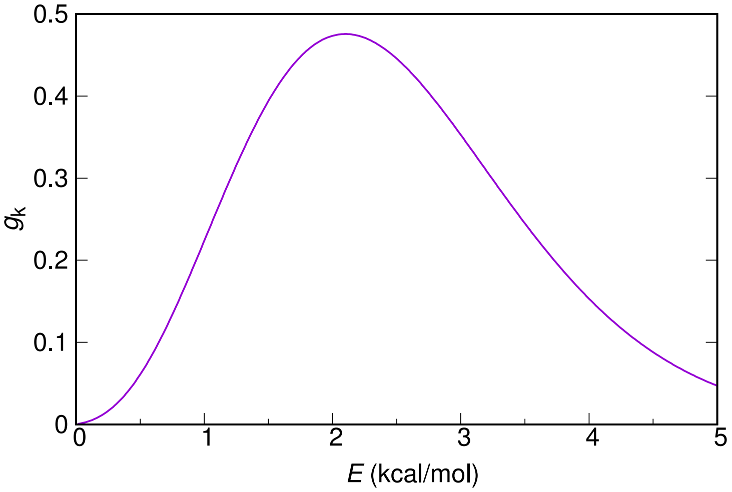

Figure S10: Fourier transform of the initial wave packet on $X^3\Sigma_g^-$ state as a function of energy. The initial wave packet is a Gaussian function defined in Eq. 5 and $g(k) = \frac{\sqrt{2\sigma}}{(2\pi)^{1/4}}\exp[-\sigma^2(k-p_0)^2)\exp(ir_0k)$. where, $k = \sqrt{2\mu E}$ and $p_0 = \sqrt{2\mu E_0}$.

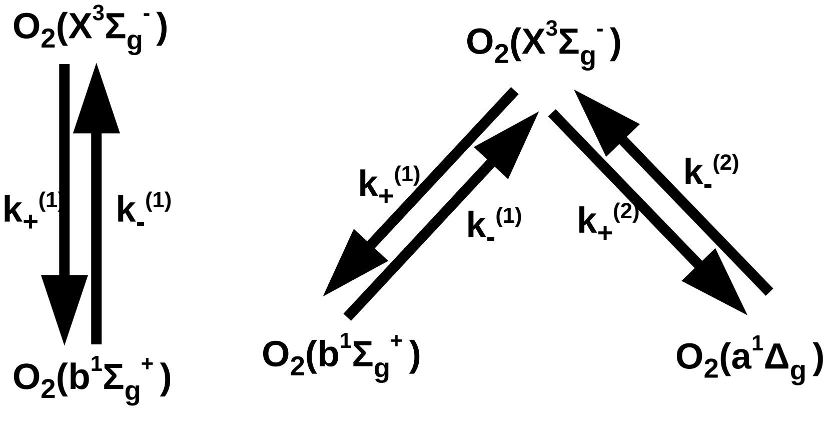
$O_2(X^3\Sigma_g^-)$
$k_+^{(1)}$
$k_-^{(1)}$
$O_2(b^1\Sigma_g^+)$
$O_2(X^3\Sigma_g^-)$
$k_+^{(1)}$
$k_-^{(1)}$
$k_+^{(2)}$
$k_-^{(2)}$
$O_2(b^1\Sigma_g^+)$
$O_2(a^1\Delta_g)$

Figure S11: Kinetic model for multiple crossing. Left: 2-state model, right: 3-state model. Here, ks are the probabilities for the transition from one state to another.

References

(1) Jorgensen, W. L.; Chandrasekhar, J.; Madura, J. D.; Impey, R. W.; Klein, M. L. Comparison of simple potential functions for simulating liquid water. *J. Chem. Phys.* **1983**, *79*, 926–935.

(2) van Gunsteren, W.; Berendsen, H. Algorithms for Macromolecular Dynamics and Constraint Dynamics. *Mol. Phys.* **1977**, *34*, 1311–1327.

(3) Pezzella, M.; Unke, O. T.; Meuwly, M. Molecular Oxygen Formation in Interstellar Ices Does Not Require Tunneling. *J. Phys. Chem. Lett.* **2018**, *9*, 1822–1826.

(4) Pezzella, M.; Meuwly, M. O_2 formation in cold environments. *Phys. Chem. Chem. Phys.* **2019**, *21*, 6247–6255.

(5) Brooks, B. et al. CHARMM: the biomolecular simulation program. *J. Comp. Chem.* **2009**, *30*, 1545–614.

(6) Meuwly, M. Reactive molecular dynamics: From small molecules to proteins. *Wiley Interdiscip. Rev.-Comput. Mol. Sci.* **2019**, *9*, e1386.

(7) T. Nagy, J. Y. R.; Meuwly, M. Multi-Surface Adiabatic Reactive Molecular Dynamics. *J. Chem. Theo. Comp.* **2014**, *10*, 1366–1375.

(8) Hollebeek, T.; Ho, T.-S.; Rabitz, H. Constructing Multidimensional Molecular Potential Energy Surfaces from ab Initio Data. *Ann. Rev. Phys. Chem.* **1999**, *50*, 537–570.

(9) Unke, O. T.; Meuwly, M. Toolkit for the Construction of Reproducing Kernel-Based Representations of Data: Application to Multidimensional Potential Energy Surfaces. *J. Chem. Inf. Model.* **2017**, *57*, 1923–1931.

(10) Bytautas, L.; Matsunaga, N.; Ruedenberg, K. Accurate ab initio potential energy curve of O_2. II. Core-valence correlations and relativistic contributions and vibration-rotation spectrum. *J. Chem. Phys.* **2010**, *132*, 1–15.

(11) Minaev, B. F.; Yashchuk, L. B. Spin-orbit coupling in oxygen near the dissociation limit. *Opt. Spectrosc* **2003**, *95*, 553–559.

(12) Dayou, F.; Hernndez, M. I.; Campos-Martnez, J.; Hernndez-Lamoneda, R. Spin-orbit coupling in $O_2(\nu)$+O_2 collisions: I. Electronic structure calculations on dimer states involving the $X^3\Sigma_g^-$, $a^1\Delta_g^+$, and $b^1\Sigma_g^+$ states of O_2. *J. Chem. Phys.* **2005**, *123*, 074311.

(13) Herzberg, G.; Huber, K.-P. *Molecular Spectra and molecular structures*; Van Nostrand, 1950.

(14) Laporte, O.; Meggers, W. F. Some Rules of Spectral Structure∗. *J. Opt. Soc. Am.* **1925**, *11*, 459–463.

(15) Turrell, G. C.; Vu, H.; Vodar, B. Induced Q Branch in the VibrationRotation Spectrum of HCl Pressurized with Ar. *J. Chem. Phys.* **1960**, *33*, 315–316.

(16) Herzberg, G. *Infrared and Raman Spectroscopy of Polyatomic Molecules*; Van Nostrand, 1954.

(17) Stine, J. R.; Muckerman, J. T. On the multidimensional surface intersection problem and classical trajectory surface hopping. *J. Chem. Phys.* **1976**, *65*, 3975–3984.

(18) Landau, L. D. Assotsiatsiya dvukhatomnykh molekul. *Phys. Z* **1932**, *2*, 46–52.

(19) Zener, C. Non−adiabatic crossing of energy levels. *Proc. R. Soc. London A* **1932**, *137*, 696–702.

(20) Belyaev, A. K.; Lebedev, O. V. Nonadiabatic nuclear dynamics of atomic collisions based on branching classical trajectories. *Phys. Rev. A* **2011**, *84*, 014701.

(21) Belyaev, A. K.; Lasser, C.; Trigila, G. Landau−Zener type surface hopping algorithms. *J. Chem. Phys.* **2014**, *140*, 224108.

(22) Miller, W. H.; George, T. F. Semiclassical Theory of Electronic Transitions in Low Energy Atomic and Molecular Collisions Involving Several Nuclear Degrees of Freedom. *J. Chem. Phys.* **1972**, *56*, 5637–5652.

(23) Prudente, F. V.; Riganelli, A.; Marques, J. M. C. Time dependent wave packet study of the electronically non-adiabatic Cl + H_2 reaction using a one-dimensional model. *Phys. Chem. Chem. Phys.* **2003**, *5*, 2354–2359.

(24) Mahapatra, S.; Köppel, H.; Cederbaum, L. S. Reactive Scattering Dynamics on Conically Intersecting Potential Energy Surfaces: The H + H_2 Exchange Reaction. *J. Phys. Chem. A* **2001**, *105*, 2321–2329.

(25) Köppel, H.; Domcke, W.; Cederbaum, L. S. *Advances in Chemical Physics*; 2007; pp 59–246.

(26) Koner, D.; Panda, A. N. Quantum Dynamical Study of the He + NeH^+ Reaction on a New Analytical Potential Energy Surface. *J. Phys. Chem. A* **2013**, *117*, 13070–13078.

(27) Feit, M. D.; J. A. Fleck, J.; Steiger, A. Solution of the Schödinger Equation by a Spectral Method. *J. Comp. Phys.* **1982**, *47*, 412 – 433.

Part III.

Hydrophobicity

4. Water Dynamics Around Proteins: T- and R-States of Hemoglobin and Melittin

In this part of the thesis an investigation on the decay of the T_0 state of Hb and on the hydrophobic pocket of melittin is performed in terms of change of hydrophobicity of the instantaneous interface, using the recently developed algorithm by Shin *et* al[36]. The algorithm evaluates $\delta\lambda_{\mathrm{phob}}$, the local hydrophocity, as function of time. For $\delta\lambda_{\mathrm{phob}} = 0$ the interfacial water behaves like an ideal hydrophobic surface, whereas $\delta\lambda_{\mathrm{phob}} > 0$ the interfacial response as an hydrophilic surface[36]). This project is in collaboration with Professor Adam P. Willard, Doctor Michiel J.M. Niesen and Doctor Sucheol Shin from MIT, that made their analysis code available and enriched the work with more detailed analysis (Figure 4.2), Doctor Krystel El Hage who analysed the intermediate structures of Hb (Figures 4.1, 4.6, 4.7 and 4.8), and under the supervision of Professor Martin Karplus from Harvard University.

Along the chapter, the expression N Å box, with N as a positive number, refers to the length of the box edge.

4.1. Simulation set-up and analysis

Simulations of Hemoglobin: The Hb-simulations were described previously,[37] and only the necessary points without technical details are reported here. The molecular dynamics trajectories were run in cubic water boxes with box edges 90 Å, 120 Å, and 150 Å which were analyzed in the following. Each simulation was run at least 1 μs. The trajectories analyzed in the present work are those from Ref.[37] and the reader should refer to that manuscript for additional details on the production runs.

In case of melittin new simulations were carried out using CHARMM[38] c45a1 and the CHARMM36 force field[13]. The TIP3P water and the melittin dimer structure (PDB:2MLT)[39] were used as the starting structure. The system was solvated with two different simulation sets with box edge of 51 Å and 60 Å in order to observe whether box size effects on the stability, dynamics and water structuring of melittin dimer were present. A 16 Å cutoff was applied with a Particle Mesh Ewald scheme[40] and a 1 fs time step was used in the MD simulations. The following protocol was applied. Two steps of minimization were performed: 50 steps with the Steepest Descent algorithm, followed by 50 steps with the Newton-Raphson algorithm. The system waa then equilibrated using the velocity Verlet algorithm for 25 ps with a Nose Hoover thermostat at 300 K. This was followed by a 100 ns NVT production simulation, whose coordinates were recorded every 1 ps. Two sets of simulations were performed: in the first, the protein dimer was fixed and only the solvent water was allowed to move, allowing a direct comparison with the work of Cheng and Rossky[41]; in the second the protein was allowed to move and only bonds involving hydrogen atoms were constrained using SHAKE[42].

The hydration structure of a simulated protein was characterized following a recently developed computational method[36]. This method is based on the concept that deformations in water's collective interfacial molecular structure encode information about the details of surface-water interactions[36]. These deformations are quantified in terms of the probability distribution of molecular configurations, as specified by the three-dimensional vector, $\kappa = (a, \cos\theta_{OH_1}, \cos\theta_{OH_2})$, where a is the distance to the water molecule from the nearest point on the instantaneous water interface, as defined in Ref.[43] and θ_{OH_1} and θ_{OH_2} are the angles between the water OH bonds and the interface normal. Local water structure for a given protein surface residue, r, is reported using the time-dependent quantity, $\delta\lambda^{(r)}_{\mathrm{phob}}(t)$, which is the log-likelihood (referred to as "local hydrophobicity" (LH) in the following) of the observed water orientational distribution near that residue given a hydrophobic reference system. Equation 4.1 defines $\delta\lambda^{(r)}_{\mathrm{phob}}(t)$:

$$\delta\lambda^{(r)}_{\mathrm{phob}}(t) = -\frac{1}{N_\tau}\sum_{t'=t}^{t+\tau}\frac{1}{N_w(t)}\sum_{i=0}^{N_w(t)} \ln\left[\frac{\alpha P(\vec{\kappa}^{(i)}(t)|\mathrm{phob})}{P(\vec{\kappa}^{(i)}(t)|\mathrm{bulk})}\right] \tag{4.1}$$

where $P(\kappa^{(i)}(t)|\mathrm{ref})$ is the probability of the observed water molecular configuration for water molecule i at time t, given a reference system. The reference distribution $P(\kappa|\mathrm{phob})$, was obtained by sampling the orientational distribution of water at an ideal planar hydrophobic silica surface[36] and the reference distribution $P(\kappa|\mathrm{bulk})$ was obtained from a simulation of bulk water. The first sum in Equation 4.1 is over all N_τ MD timesteps within an evaluation window of length $\tau = 10$ ps; the second sum is over all $N_w(t)$ water molecules that are within a cutoff of 6 Å of protein residue r, at time t. α is a normalization constant that is set so that $\langle\delta\lambda_{\mathrm{phob}}\rangle = 0$ when sampling from the reference hydrophobic distribution itself.

Values of $\delta\lambda^{(r)}_{\mathrm{phob}}$ near zero indicate that water observed near residue r exhibits orientations that correspond to those found at an ideal hydrophobic surface. Hydrophilic surfaces interact with interfacial water molecules and lead to configurational distributions that differ from that of an ideal hydrophobic surface. These differences are typically reflected as a positive deviation in $\delta\lambda^{(r)}_{\mathrm{phob}}$, with larger differences giving rise to larger positive deviations in $\delta\lambda^{(r)}_{\text{phob}}$. For the configurational sample sizes used to compute $\delta\lambda^{(r)}_{\text{phob}}$ here, we use values of $\delta\lambda_{\text{phob}}(r) \geq 0.5$ as indicative of hydrophilicity. The fluctuations in $\delta\lambda^{(r)}_{\text{phob}}$ as a function of time provide information about changes in the local solvation environment.

4.2. Hydration Dynamics around Hemoglibin

Figure 4.1 shows the structure of Hb with the C_α atoms of the residues analyzed specifically shown as van der Waals spheres. residues that were studies were the ones in Perutz' stereochemical model[44], which are involved in the salt bridges and the α/β shearing motion (Table 4.1). The shearing motion involves a change in the H-bonds at the α_1/β_2 interface. In the T_0 structure the side chain of Thr41α_1 occupies a notch formed by the main chain of Val98β_2 and a hydrogen bond is present between Tyr42α1 and Asp 99β_2. After the transition to the R_4 state, the same notch is occupied instead by Thr38α_1 and the previous hydrogen bond is substituted by one between Asp94α_1 and Asn102β_2. The same conformational change occurs at the α_2/β_1 interface.

The conformational differences between the T and R states affect the hydration environment in a manner that can be detected with $\delta\lambda^{(r)}_{\text{phob}}$. Based on the previous simulation[37], the set of residues for which $\delta\lambda_{\text{phob}}$ changes most across the transitions was selected. Figure 4.3 (top panel) reports the C_α His146β_1–His146β_2 separation, which serves as an indicator of the T-to-R transition for the simulations in the 90, 120, and 150 Å boxes. For the simulations in the two smaller boxes, three steps between the T_0 state (at early times) and the R_0 state (at late times, see Figure 1 in Ref.[37]; the R_0 state has the same quaternary structure as R_4 but with no ligands bound to the heme groups, see Figure 4.3) are evident and they indicated by red dashed lines. Structural changes are accompanied by changes in the number of hydration waters. For the simulation in the largest (150 Å) box, the C_α His146β_1–His146β_2 separation is constant and the average hydration is larger than 0.95, see bottom row in Figure 4.3.

As previous results have shown, the relative stability of the T_0 state depends on the size of the simulation cell[37]. Analysis of hydration structure via $\delta\lambda^{(r)}_{\mathrm{phob}}$ has the ability to reveal when and where protein hydration properties differ between differently sized simulation cells. To highlight this ability, the statistics and dynamics of $\delta\lambda^{(r)}_{\mathrm{phob}}$ for Hb in the T_0 state in simulation cells of 90 Å and 150 Å side length were compared. Figure 4.2 contains a plot of the probability distribution, $P(\delta\lambda^{(r)}_{\mathrm{phob}})$ taken over all water-exposed residues of the T_0 state in the two different simulation boxes. From these results it is observed that the distribution of the water's interfacial structure around hemoglobin depends on the simulation box size. Based on this analysis, the T_0 state presents as slightly more hydrophobic in the smaller 90 Å box. The difference in these distributions indicates that protein hydration structure can be artificially modified through changes in the simulation cell. To probe the dynamics of water's interfacial structure the time correlation function is computed, $C_r(t) = \langle \delta\lambda^{(r)}_{\mathrm{phob}}(0)\delta\lambda^{(r)}_{\mathrm{phob}}(t)\rangle$, where the angle brackets indicate an average over time segments where Hb remains in the T_0 state. We then define a correlation time, τ_r, for each residue by fitting $C_r(t)$ to a single exponential decay. The distribution of τ_r values for different surface residues is plotted in Fig. 4.2B. It is observed that the hydration dynamics differ significantly between the 90 Å and 150 Å simulation cells. In particular, the larger simulate cell has a distribution of local relaxation times that are shifted to longer times. Notably, the 150 Å box exhibits enhanced tails corresponding to residues with long correlation times. There is no apparent correlation between the value of τ_r and $\delta\lambda^{(r)}_{\mathrm{phob}}$ across the surface residues.

The residues that were analyzed in detail are summarized in Table 4.1 and include those previously identified in the Perutz stereochemical model[44].

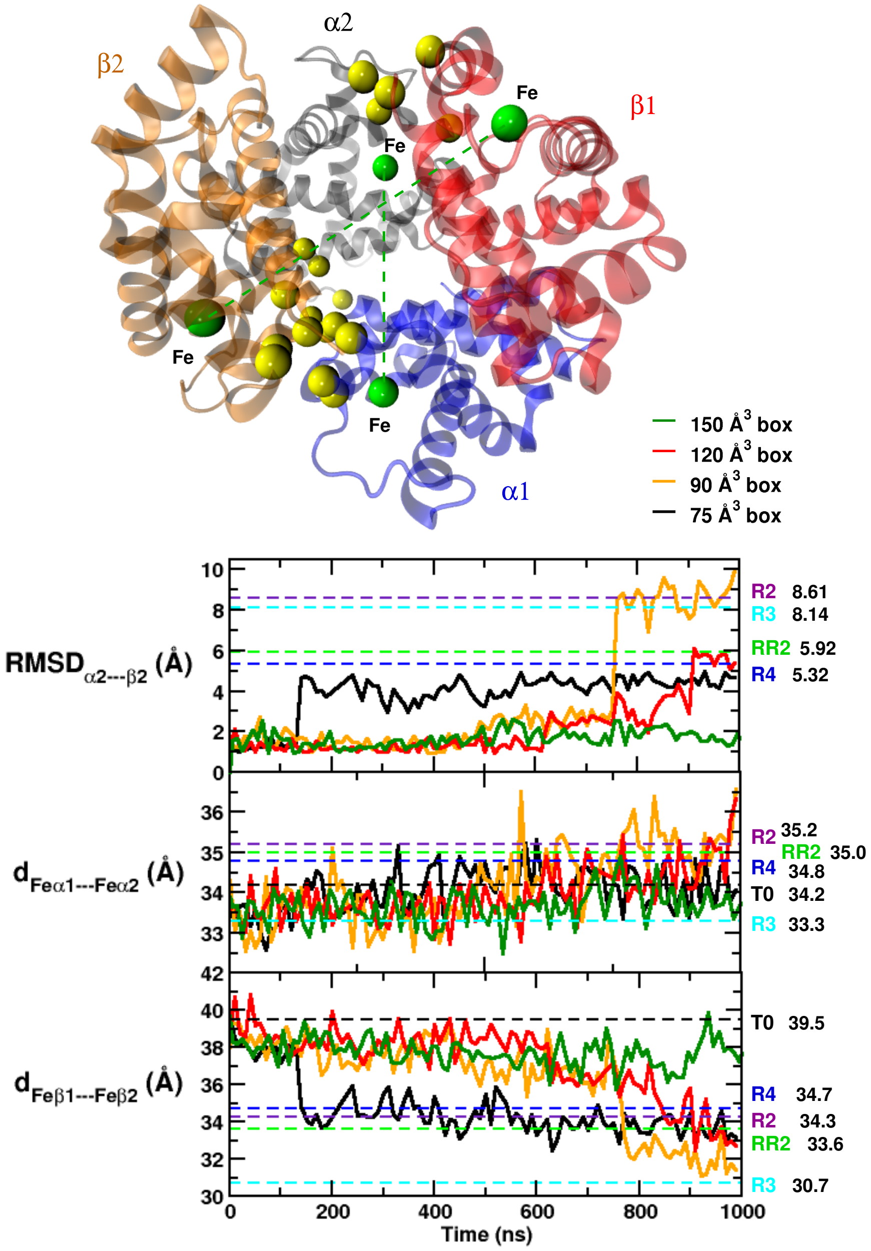

Figure 4.1.: Top: Representation of the Hb with the Cα atoms of the residues relevant to Perutz' stereochemical mechanism as yellow spheres. The iron atoms (Fe, green spheres) are specifically indicated, and the green dashed lines indicate the distances calculated. Bottom: Quaternary structure differences of Hb structures found in our simulations, based on the structural comparison of the $\alpha_1\beta_1$ and $\alpha_2\beta_2$ subunits. From top to bottom: RMSD of the nonsuperimposed $\alpha_2\beta_2$ subunit after superimposing the $\alpha_1\beta_1$ subunit (Cα carbons were used for both superposition and RMSD calculation); Fe-Fe distances between the α and β of each subunit. Horizontal dashed lines indicate the corresponding values from all known Hb structures T_0, R_2, RR_2, R_3 and R_4). Information for the T_0 state are in black, for the R_2 in maroon, for the RR_2 in green and for R4 in blue

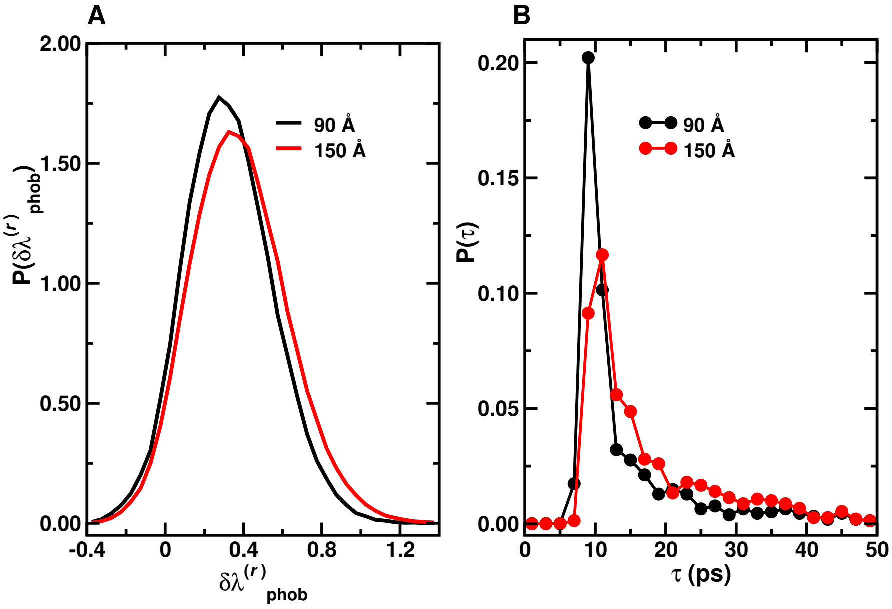

Figure 4.2.: (**A**) The distribution of $\delta\lambda^{(r)}_{\text{phob}}$ for water exposed residues of Hb in the T_0 state. The black and red lines correspond to simulations carried out in 90Å and 150Å solvent boxes, respectively. (**B**) The distribution of hydration structure relaxation times evaluated for surface residues of the T_0 state in the 90Å and 150Å simulation cell.

(a) Results for Hb 90 Å box: The LH analysis for the 1 μs simulation is carried out with a time resolution of 0.5 ns. A cut off of 6 Å from the protein is chosen to distinguish between interfacial and bulk water. The structural transitions for the 90 Å box occur at $t = 470$ ns, $t = 770$ ns, and $t = 891$ ns, as indicated by the distance r_{His146} between the C_α atoms of the two His146 residues in the β_1 and β_2 chains. The total number of interfacial water is found to correlate with this distance (see bottom row of Figure 4.3). Whenever the distance between the two His146 residues (see Reference[37]) decreases abruptly (as indicated by the red dashed lines), the relative number of water molecules r_w within the 6 Å cutoff increases. The value of $r_w = N_{\text{max}}/N_{\text{max}}$ was determined as the instantaneous number N_{max} of water molecules for a specific snapshot and the maximum N_{max} encountered along the entire trajectory.

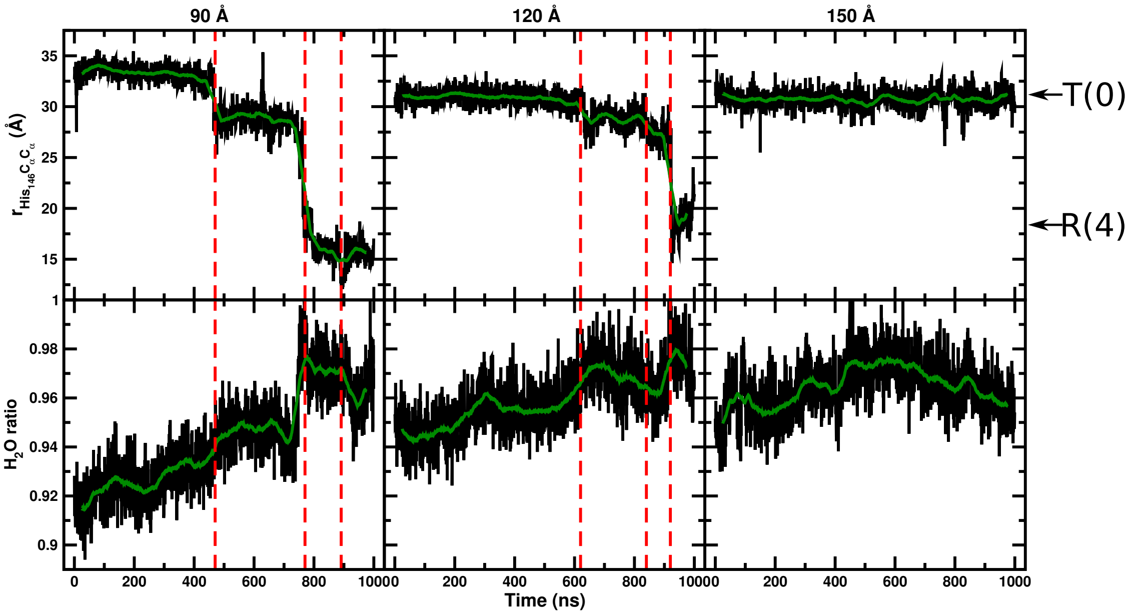

Figure 4.3.: Top: The C_α His146β_1–His146β_2 separation as a function of time for the 90, 120 and 150 Å box. The arrows on the right-hand side indicate the His146β_1–His146β_2 separation from the 2DN2 (T_0) and 2DN3 (R_4) crystal structures[45]. Bottom: The hydration ("H_2O ratio") of the entire protein, expressed in terms of $\frac{N_{\text{wat}}}{\max(N_{\text{wat}})}$. The vertical red dashed lines indicate the transition times.

To obtain more detailed information, $\delta\lambda_{\text{phob}}(t)$ was analyzed for the residues listed in Table 4.1, see Figure 4.4. For certain residues, structural transitions (at $t = 470$ ns, $t = 770$ ns, and $t = 891$ ns) are accompanied by abrupt rather than by gradual changes in local hydrophobicity of individual residues. Examples include Val98β_1, Thr41α_1, and Asp94α_1. By contrast, Tyr42α_1 shows a gradual decrease in $\delta\lambda_{\text{phob}}$ over most of the 1 μs simulation. Except for Val98β_1 all residues that show a substantial increase in their hydrophilic ($\delta\lambda_{\text{phob}} \sim 0.5$) versus hydrophobic ($\delta\lambda_{\text{phob}} \sim 0$) character [Thr41$\alpha_1$, Tyr42$\alpha_1$] or a decrease [Thr38$\alpha_1$, Asp94$\alpha_1$, Asp99$\beta_2$] are at the α_1/β_2 interface. This suggests that the decay for the 90 Å box is triggered primarily by the hydration around residues that are involved in the $\alpha_1 - \beta_2$ contacts.

Based on the data shown in Figure 4.4, the $T_0 \rightarrow R_0$ transition in the 90 Å box is accompa-

Table 4.1.: The residues of Hb for which the local hydrophobicity $\delta\lambda_{\mathrm{phob}}$ is specifically analyzed from the Perutz' stereochemical model[44]. For each residue its involvement in specific contacts is reported.

Residue	Role in the protein
Arg141α_1	α C-terminal salt bridge
Val1α_2	α C-terminal salt bridge
Asp126α_2	α C-terminal salt bridge
Lys127α_2	α C-terminal salt bridge
Tyr140α_1	α proximity to the C-terminal residue
His146β_1	β C-terminal salt bridge
Lys40α_2	β C-terminal salt bridge
Asp94β_1	β C-terminal salt bridge
Tyr145β_1	β salt bridge involved in His146β_1 motion
Val98β_1	β salt bridge involved in His146β_1 motion
Thr38α_1	$\alpha_1 - \beta_2$ shearing
Thr41α_1	$\alpha_1 - \beta_2$ shearing
Tyr42α_1	$\alpha_1 - \beta_2$ shearing
Asp94α_1	$\alpha_1 - \beta_2$ shearing
Cys93β_2	$\alpha_1 - \beta_2$ shearing
Val98β_2	$\alpha_1 - \beta_2$ shearing
Asn102β_2	$\alpha_1 - \beta_2$ shearing
Asp99β_2	$\alpha_1 - \beta_2$ shearing

nied by significant changes in the hydration environment at certain locations around the $\alpha_1\beta_2$ contact. This observation is consistent with Perutz' conclusion[44]. The significant changes in hydration properties around the $\alpha_1\beta_2$ contact indicate the possibility that the $T_0 \rightarrow R_0$ transition is driven by solvent thermodynamics.

(b) Results for Hb 120 Å box: For the simulation in the 120 Å box most of the residues involved in the salt bridges, like those in the 90 Å box, show only minor variations in $\Delta\langle\delta\lambda_{\mathrm{phob}}\rangle$ except that of Val98β_1, which is associated with the first transition (see Figure 4.5). Also, several of the residues at the α_1/β_2 interface show pronounced changes in local hydrophobicity that coincide with structural transitions. However, in contrast to the 90 Å box, several residues in column D (i.e., Val98β_2, Asp99β_2, and Asn201β_2) show

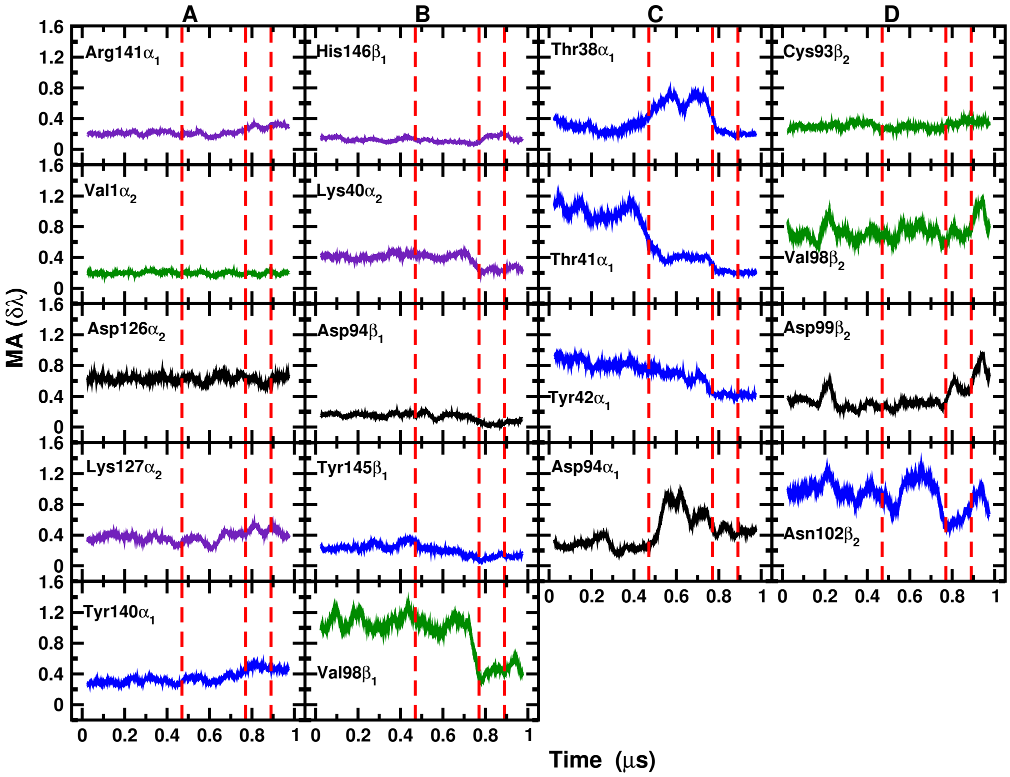

Figure 4.4.: Local hydrophobicity for the simulation in the 90 Å box. Moving average over 50 ns of $\delta\lambda_{\text{phob}}$ as a function of time for residues involved in the C-terminal salt bridges[44] (column A), additional salt bridges (column B) and the $\alpha_1\beta_2$ shearing motion. Positive charged amino acid are in violet, polar ones in blue, negative one in black and hydrophobic ones in green

local hydrophobicity changes that cannot be linked to a transition. For the second and third transition, there is again a clear change for Thr41α_1, Thr38α_1, and Asp94α_1. This may also suggest that the nature of the first transition (step1) in the 90 Å and 120 Å box is different.

Figures 4.3, and 4.6 to 4.8 show that the transition between T$_0$ and R$_4$ occurs via intermediate structures, specifically R$_2$, RR$_2$ and R$_3$, via different macromolecular properties: Figure 4.6 shows the variation of some general properties characterizing the Hb transition, details on the His146β, that are used for characterizing the T$_0$ →R$_0$

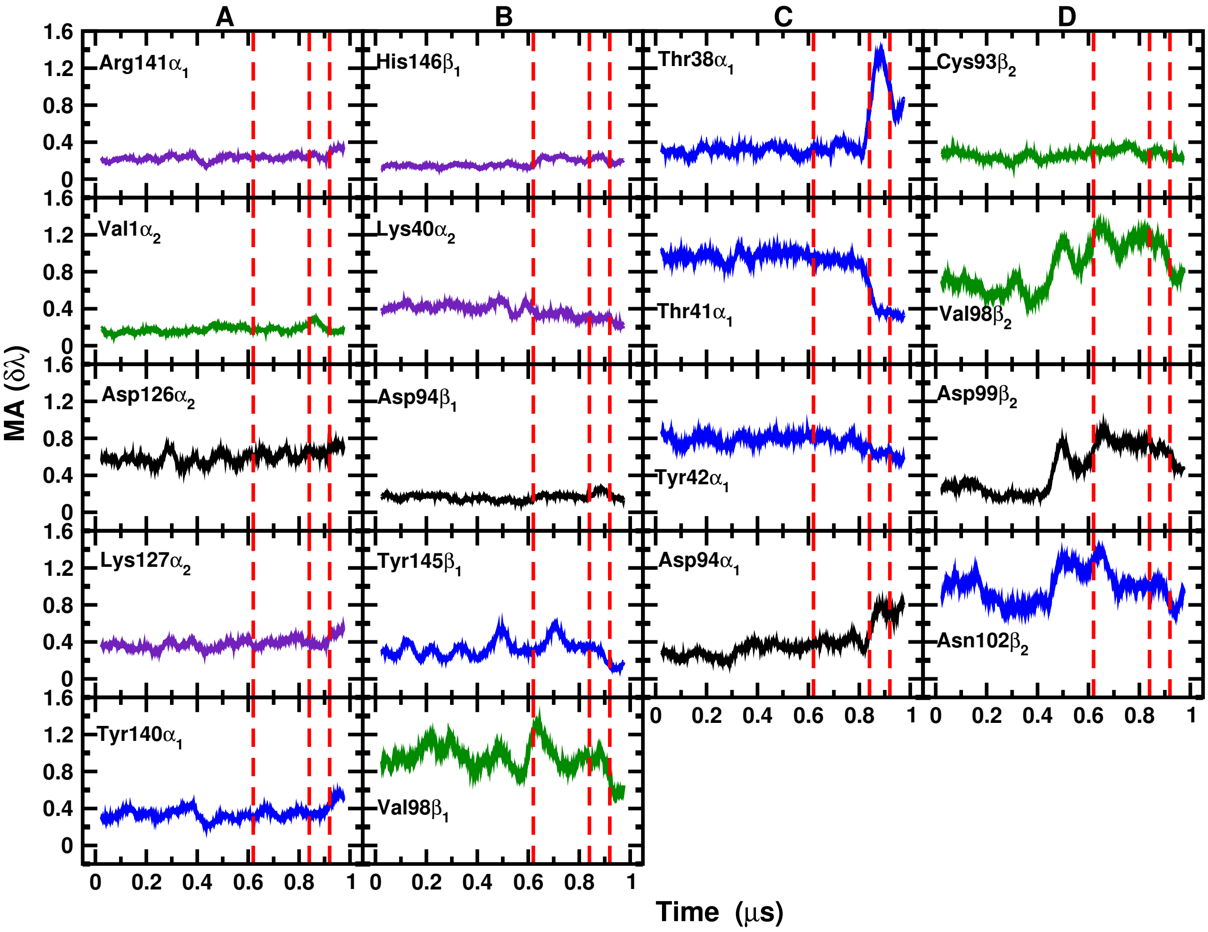

Figure 4.5.: Local hydrophobicity for the simulation in the 120 Å box. Moving average over 50 ns of $\delta\lambda_{\text{phob}}$ as a function of time for residues involved in the C-terminal salt bridges[44] (column A), additional salt bridges (column B) and the $\alpha_1\beta_2$ shearing motion (columns C and D), see Table 4.1. Positive charged amino acid are in violet, polar ones in blue, negative one in black and hydrophobic ones in green

transition in Ref.[37], are described in Figure 4.7, results on the quaternary are illustrated in Figure 4.3 and, finally, results for the $\alpha_1\beta_2$ interface are illustrated in Figure 4.8. The 3D structures of the relaxed forms of hemoglobin were taken from the following crystal structures:

- R_2-state for liganded human HbA at 1.7 Å resolution (PDB ID 1BBB)[46] for the R_2 form.

- RR_2-state embryonic human Gower II COHb at 2.2 Å (PDB ID 1AJ9)[47].
- R_3 CO-liganded Hb at 2.15 Å (PDB ID 4NI0)[48].

The iron-iron distances between the αs and βs of each subunit were also measured (Figure 4.3). Figure 4.3 shows that the large quaternary structural differences between T and R forms is accompanied by significant differences in the α_1-α_2 and β_1-β_2 iron-iron distances that are reduced in the R-states, most notably for the R_3 structure. This movement of the subunits has a large effect on the interdimer interface (as observed in the interaction distances reported in Figure 4.7) and on the central water cavity relative to the T structure. As shown in the Cα-Cα distance between His146β_1 and His146β_2 and the Cα-Cα distance between His143β_1 and His143β_2 reported in Figure 4.6 (first two panels from top), the β-cleft entrance to the central water cavity is narrowed (compared to the T structure with the larger central cavity) thus leading to less water entering the central cavity. This decrease of the number of water molecules in the central cavity was observed in our previous paper[37] where the water molecules in the central cylinder for the different box sizes was counted.

In addition, specific H-bonds at the α_1 β_2 dimer interface were also analyzed (Figure 4.8). First, the hydrogen bond interaction between Thr38α_1 and His97β_2 observed in the R_3 structure but missing in the RR_2 and R_2 intermediate structures were sampled in our simulations. This is due to differences in the position of the β_2-subunit relative to the α_1-subunit (see RMSD in Figure 4.3). Second, the hydrogen bond between Tyr42α_1 and Asn97β_2 only present in the T structure and absent in all R-forms was observed for the stable T state simulation and was absent in all boxes with transitions. Finally, the hydrogen bond interaction between Arg92α_1 and Gln39β_2 or Glu43β_2 present in RR_2 and missing in all other states was also observed.

The radial pair distribution function $g(r)$ reflects the hydration states of each residue in

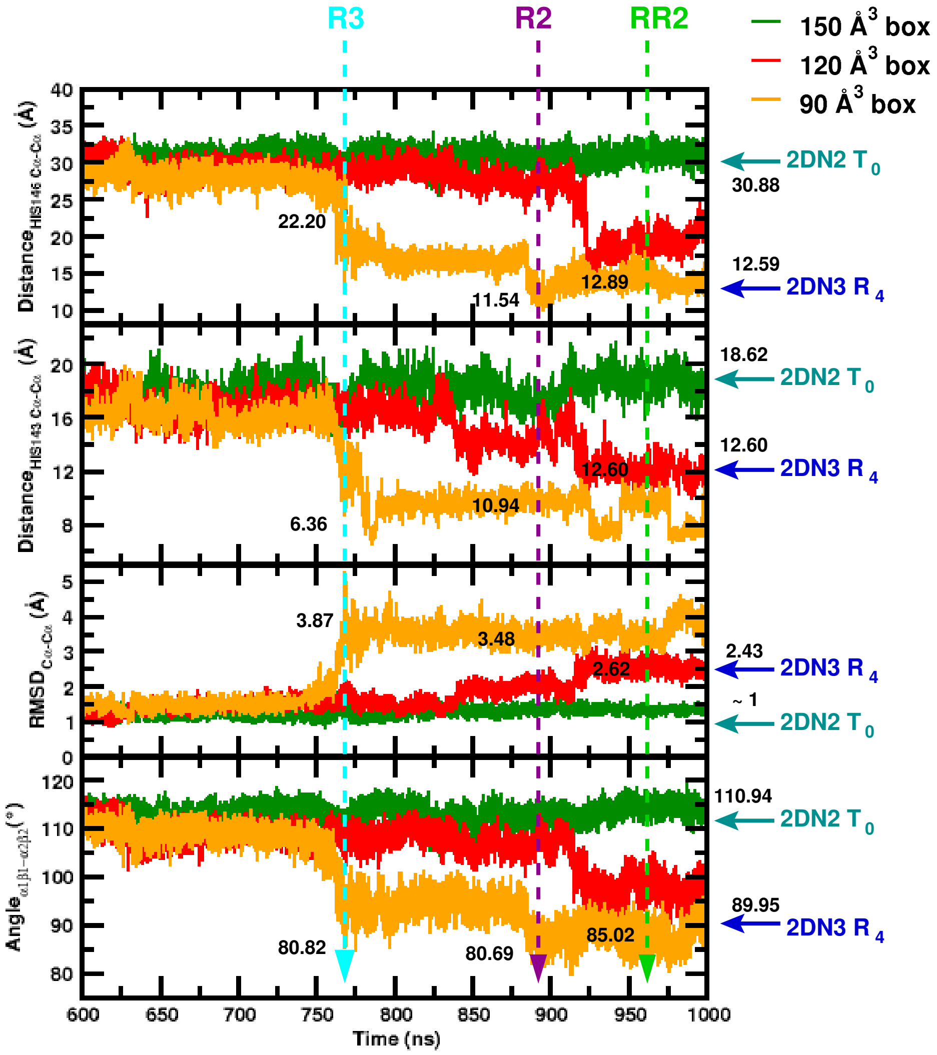

Figure 4.6.: Global structural changes of T_0 Hemoglobin tetramer depending on water box size in the [600:1000] ns interval. From top to bottom: temporal change of the $C\alpha$–$C\alpha$ distance between His146β_1 and His146β_2, the $C\alpha$–$C\alpha$ distance between His143β_1 and His143β_2, $C\alpha$ RMSD relative to the 2DN2 X-ray structure (corresponding to the T_0 state), and the theta angle between the two planes containing His146β_1-Feβ_1-Feα_1 and His146β_2-Feβ_2-Feα_2, respectively. Dark cyan and blue arrows indicate the values of the corresponding observables found for the deoxy and oxy states, respectively. Vertical dashed lines (violet, light green and light cyan) indicate observed intermediate states (R_2, RR_2 and R_3) for the boxes showing transitions from the T_0 state. The values of each intermediate state is also indicated in each panel next to the corresponding dashed line.

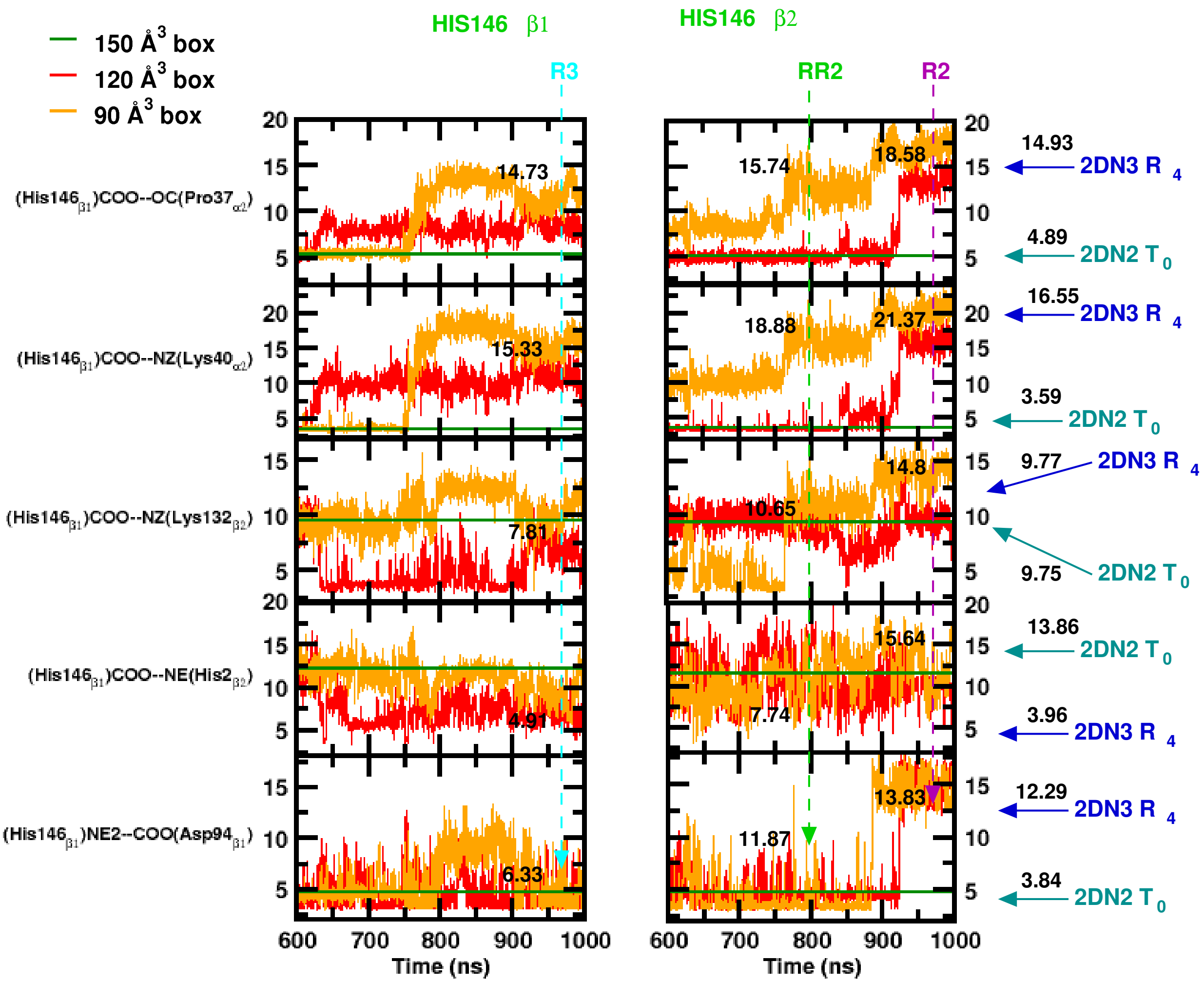

Figure 4.7.: Local structural changes around His146 in the [600:1000] ns interval, left panels: interactions involving His146β_1, right panels the interactions involving His146β_2. From top to bottom: water-mediated contact between (His146β)COO–OC(Pro37α), the salt bridge between (His146β)COO–NZ(Lys40α), the contact between (His146β)COO–NZ(Lys132β), the contact between (His146β)COO and NE(His2β) and the salt bridge between (His146β)NE2 and COO(Asp94β). The straight green line represents the averaged distance over 1 μs of MD simulation for the 150 Å box as reference of a stable T_0 state.

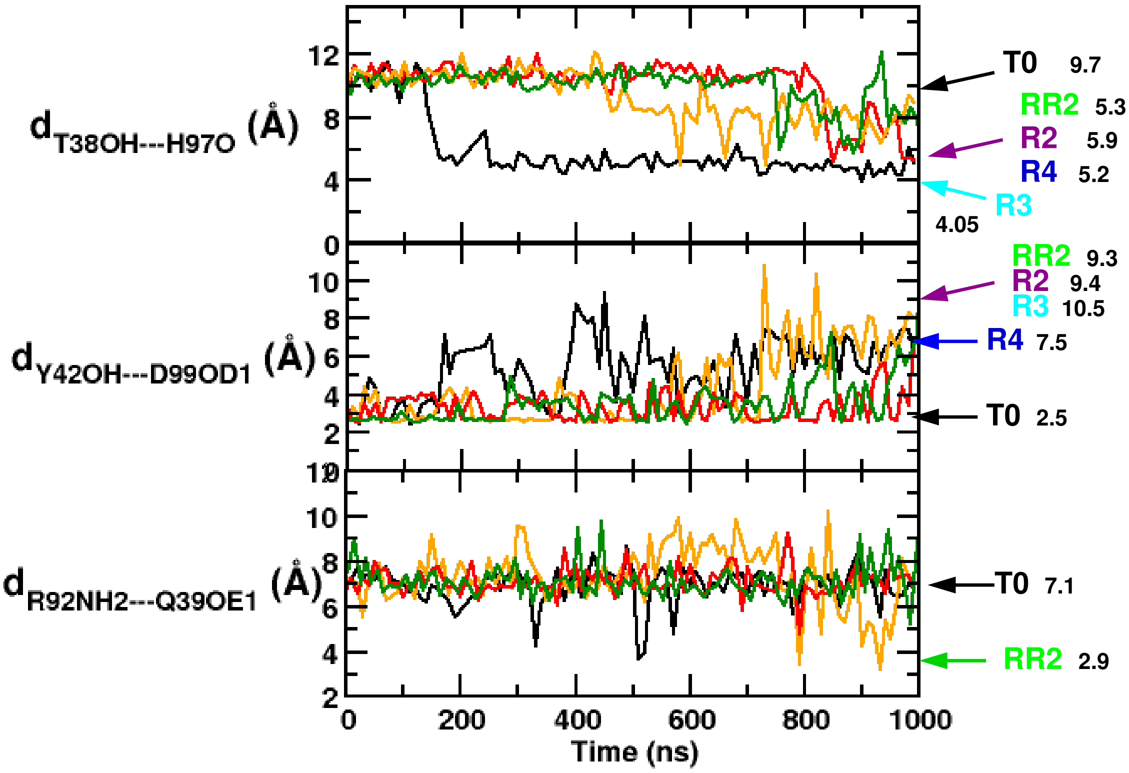

Figure 4.8.: Analysis of H-bond contacts at the $\alpha_1\beta_2$ dimer interface. The absence or presence of these contacts is indicative of the presence of intermediate states in our simulations. From top to bottom: hydrogen bond interaction between Thr38α_1 and His97β_2, Tyr42α_1 and Asp99β_2 and Arg92α_1 and Glu39β_2. Black, blue, light cyan, light green and violet arrows indicate the values of the corresponding observables found for the deoxy T_0, oxy R_4 states and the intermediate states R_3, RR_2 and R_2, respectively.

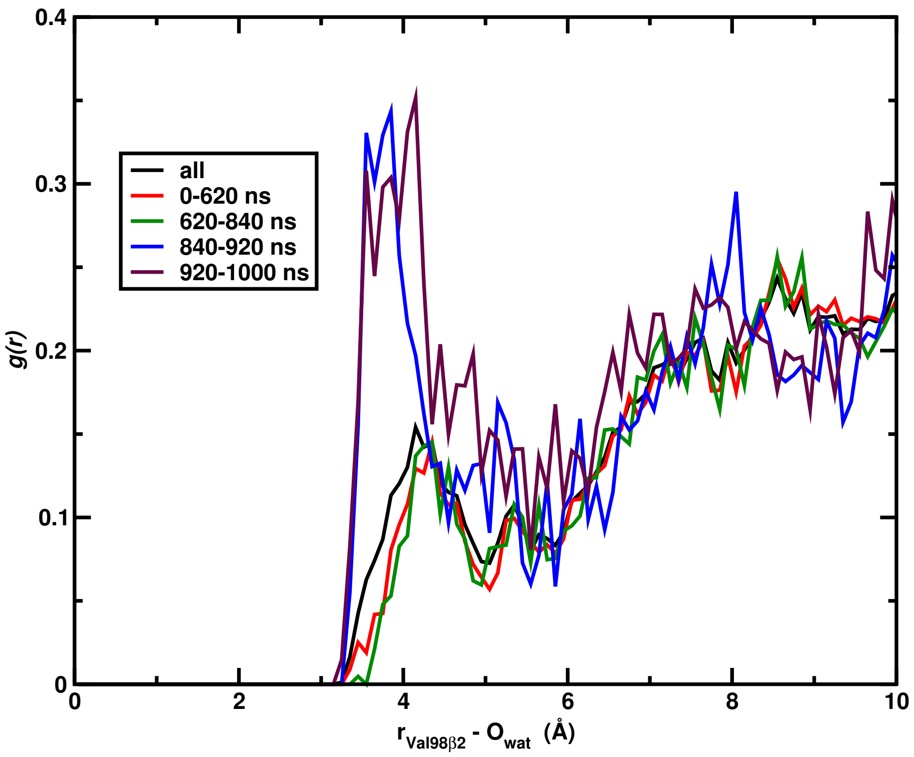

Figure 4.9.: Radial pair distribution function, $g(r)$, for the C_α of Val98β_2 and the water oxygen atoms from simulations in the 120 Å box. The distribution is reproduced for all the entire simulation (black), for step1 0-620 ns (red), step2 620-840 ns (green), step3 840-920 ns (blue) and step4 920-1000 ns (maroon). A large difference is observed before and after the transition at 840 ns. Before the last transition the C_α is "dry" and after the transition it is "wet".

each time interval of the simulation. An example is shown in Figure 4.9 for Val98β_2 C_α. A strong variation of the $g(r)$ is observed during the second step ($\sim$ 840 ns): the intensity of the first peak increases by a factor of two and its position is shifted at lower distances. A similar shift is observed for the second peak with no considerable difference in the intensity.

Possible changes of the hydration of each residues can be addressed by internal motion inside a residue or by the influence of neighbouring ones. The peak in the hydrophobicity in Val98β_2 in Figure 4.5 can be addressed by the rotation of the isopropyl group of the

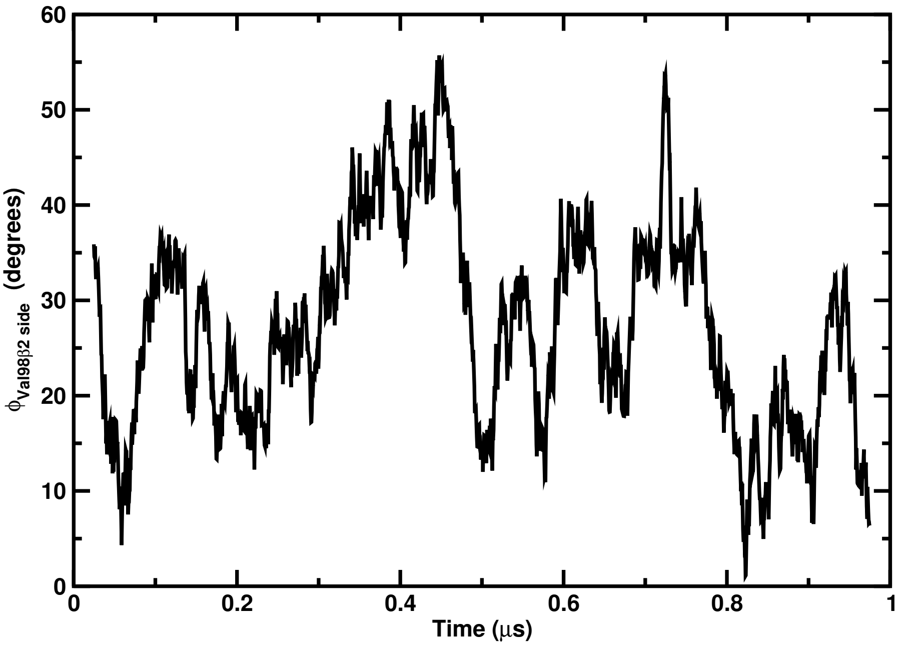

Figure 4.10.: Moving average of the time series of the torsional angle involved in the isopropyl rotation for the Val98β_2 side chain. A clear transition is observed around 500 ns.

side chain, reported in Figure 4.10. The change of hydrophobicity during the second step is a consequence of the breaking of the salt bridge between Tyr42α_1 and Asp99β_2 and consequent rearrangement of the carboxy side due the rehydration of the group (see Figure 4.11).

(c) Results for Hb 150 Å box: For the 150 Å box the previous MD simulations did not find a structural transition.[37] The values of $\delta\lambda_{\text{phob}}$ for all residues involved in the salt bridges (Figure 4.12, columns A and B) did not deviate significantly from their average value. The amplitude of the fluctuations are typically smaller than the simulations in the 90 Å and 120 Å boxes. For the residues at the $\alpha_1\beta_2$ interface there are variations for

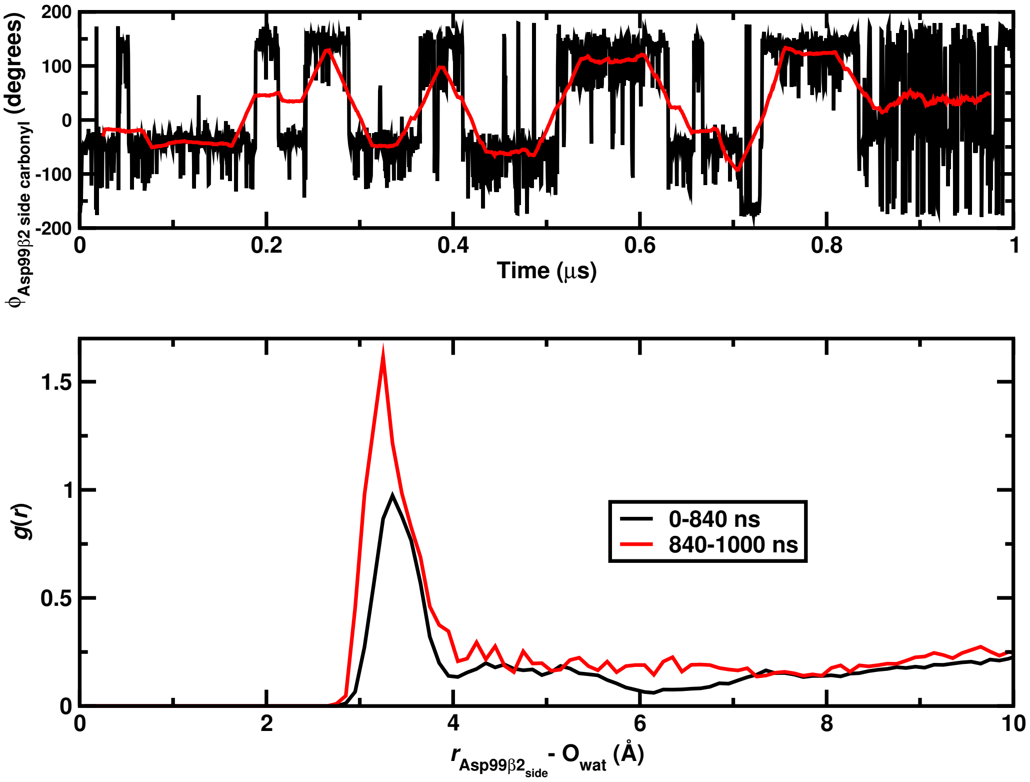

Figure 4.11.: Top: Time series of the torsional angle of the carboxy moiety of the Asp99β_2 side chain. The presence of a transition is observed after the structural transition at 840 ns: after breaking the salt bridge with the hydrogen in the tyrosine side chain, a free rotation motion is observed during dynamics. As a consequence of this rearrangement, an increase of the water coordination in the first shell is observed in the $g(r)$, as shown in the bottom panel.

Thr38α_1, Thr41α_1, Tyr42α_1, and Asp94α_1.

The most apparent difference between the simulation in the 150 Å and the two smaller boxes is, however, the behaviour for residues Val98β_2, Asp99β_2, and Asn102β_2. As an example, the water occupation around Val98β_2 is analyzed by computing the radial distribution function $g(r)$ between the C_α of the residue and the surrounding hydration water for different parts of the trajectory, see Figure 4.3.

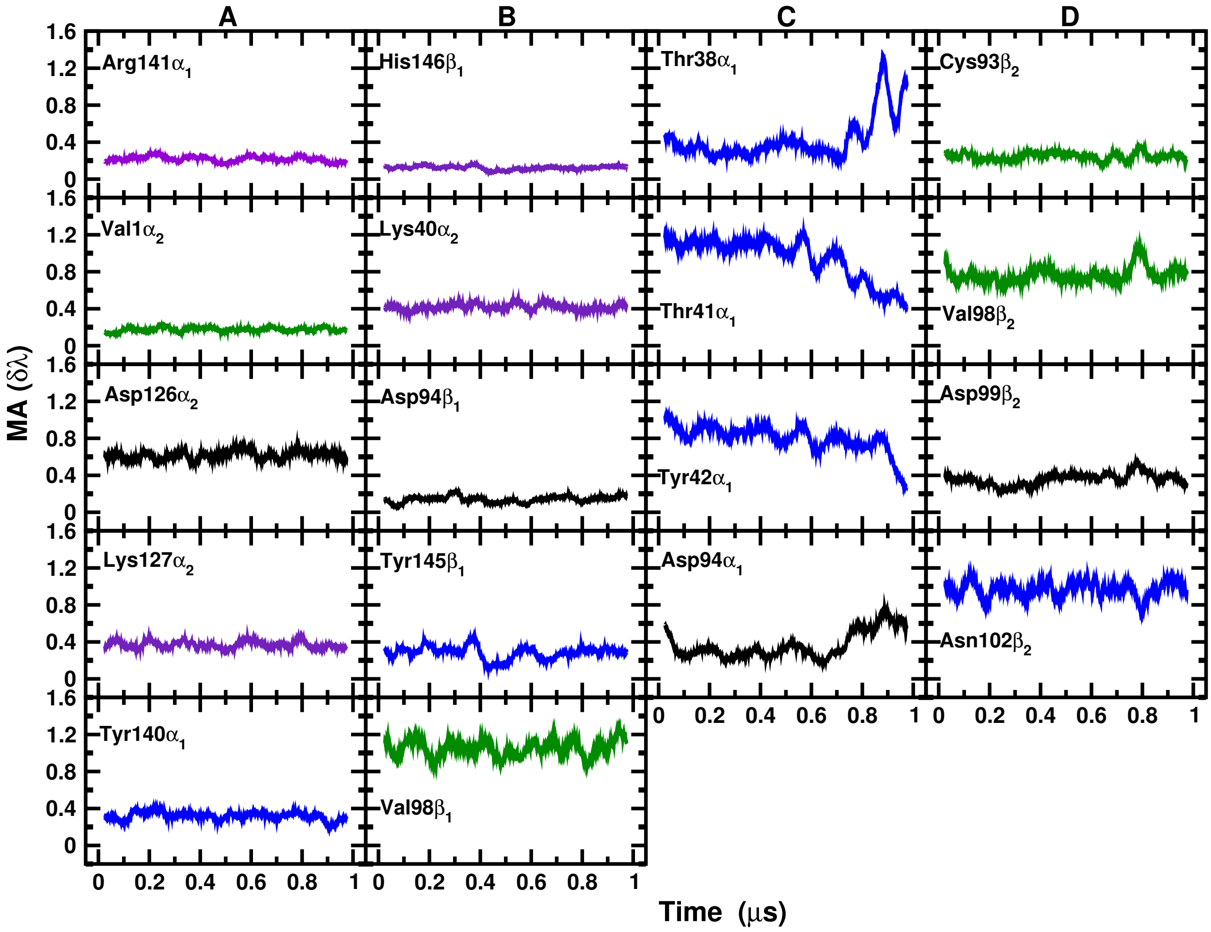

Figure 4.12.: Local hydrophobicity for the simulation of the 150 Å box. It shows moving averages over 50 ns of $\delta\lambda_{\text{phob}}$ as a function of time for residues involved in the C-terminal salt bridges[44] (column A), additional salt bridges (column B) and the $\alpha_1\beta_2$ shearing motion (columns C and D), see Table 4.1. Positive charged amino acid are in violet, polar ones in blue, negative one in black and hydrophobic ones in green

(d) Spatio-temporal analysis based on two-dimensional correlation maps: To better understand the coupling of local hydration dynamics and the structural transitions, two-dimensional correlation maps were generated as follows. Similar to dynamic cross correlation maps (DCCMs)[49,50] for residues i and j the quantity

$$C_{ij} = \frac{\langle \Delta\delta\lambda^{(i)}_{\text{phob}} \Delta\delta\lambda^{(j)}_{\text{phob}} \rangle}{\sqrt{\langle (\Delta\delta\lambda^{(i)}_{\text{phob}})^2 \rangle \langle (\Delta\delta\lambda^{(j)}_{\text{phob}})^2 \rangle}} \tag{4.2}$$

was determined for each interval where Hb was in a particular conformational state as seen in Figure 4.1.

Figure 4.14 reports the difference between the local hydrophobicity for step1 and step2 for the 120 Å box for values of $\delta\lambda_{\text{phob}} > 0.3$, see Figure 4.13. This correlation appears to depend on sequence or spatial proximity of two residues. An example of sequence proximity is the Val98β_1-Asp99β_1 region. Examples for spatial proximity of residues are the two clusters (labelled A and B in Figure 4.14) present at the α_2 β_1 shearing interface. This change in hydrophobicity in one of the two important stabilizing regions of the protein (the other being the α_1 β_2, see Figure 4.15), indicates its possible involvement in the destabilization of the T_0 structure.

A detailed view of the correlations for the $\alpha_1\beta_2$ interface is provided in Figure 4.15. The correlation is large ($C_{ij} > 0.30$) for the residues playing an active role in interface transitions between the two subunits (see top part of Figure 4.15) and for regions that are spatially close (bottom part). Figure 4.15 shows different regions influencing the α_1/β_2 shearing interaction, involved in the 840 ns transition. During the transition three salt bridges are broken (Thr41α_1 - Arg40β_2, Arg92α_1 - Gln35β_2 and Asn97α_1 - Asp99β_2), followed by the rearrangement of the Asn97α_1 - Arg40β_2 salt bridge. This figure provides a dynamic view of the stereochemical model proposed by Perutz[44]. This can, for example, be seen in the fact that all clusters (A to F) are extended instead of the usual point-to-point contacts (i.e. the salt bridges) only. All clusters (A to E) in Figure 4.15 involve correlated changes in LH at the α_1/β_2 interface, with the exception of cluster

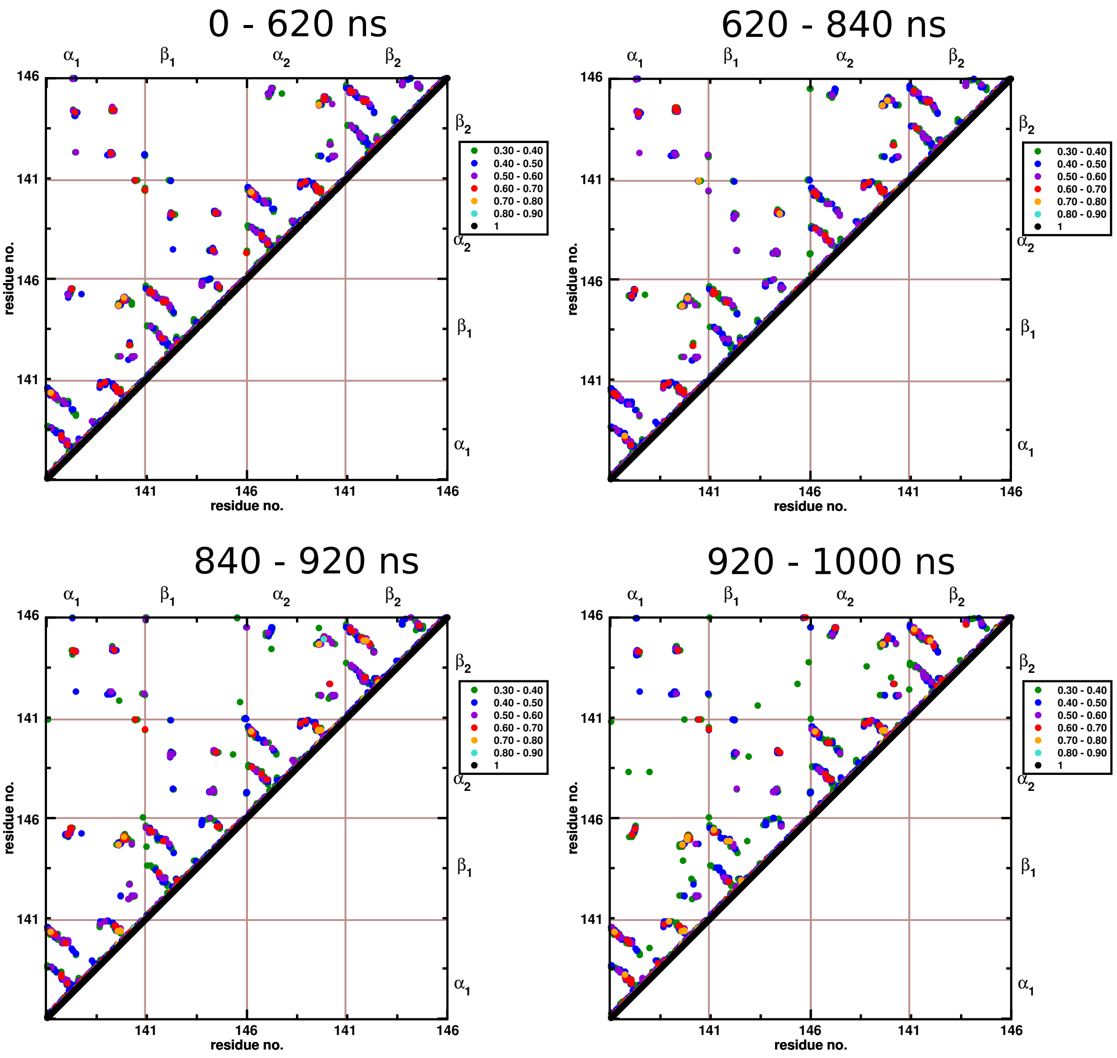

0 - 620 ns

620 - 840 ns

840 - 920 ns

920 - 1000 ns

Figure 4.13.: Local Hydrophobicity Cross Correlation Coefficients (CCC) for step1 (0 to 610 ns) and step 2 (610 ns to 820 ns) (see Figure 4.3), for the 120 Å box. The difference map is given in Figure 4.14. Only point with correlation higher than 0.30 are reported with the following color order: green $0.30 < CCC \leq 0.40$, blue $0.40 < CCC \leq 0.50$, violet $0.50 < CCC \leq 0.60$, red $0.60 < CCC \leq 0.70$, orange $0.70 < CCC \leq 0.80$, cyam $0.80 < CCC \leq 0.90$ and black $CCC = 1$

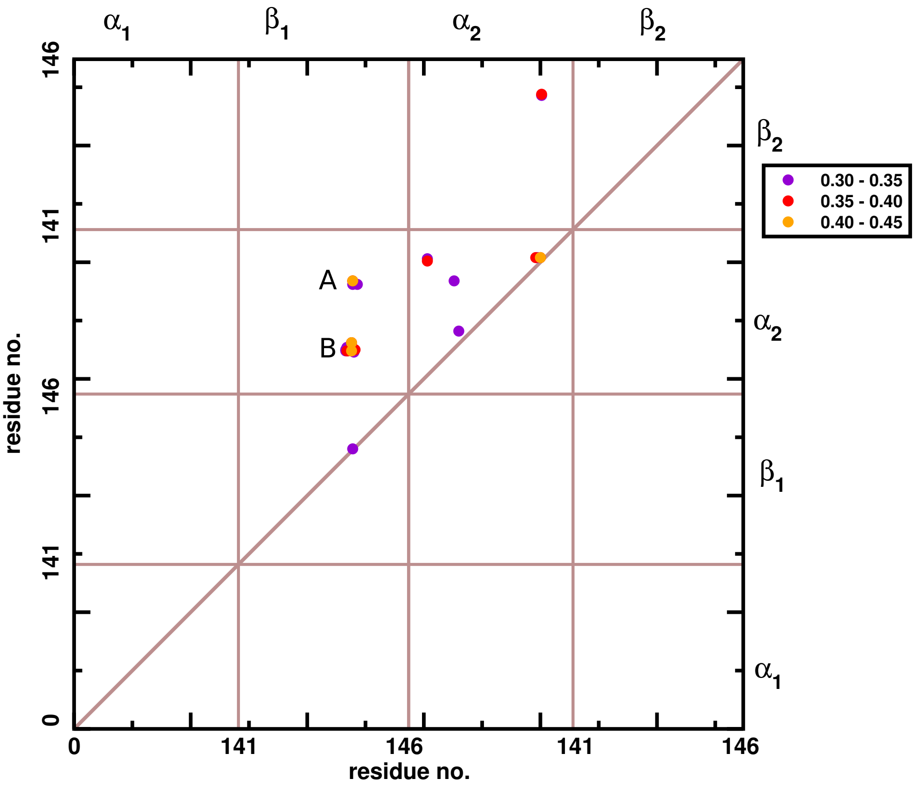

Figure 4.14.: Difference of Local Hydrophobicity Cross Correlation Map (CCM) for the 120 Å box between the structure stable up to step1 (0 to 620 ns) and the structure stable from step1 to step2 (620 ns to 820 ns) (see Figure 4.3). The CCMs for the individual states are given in Figure 4.13. Effects of the α_2 β_1 shearing are evidenced in two clusters A and B. Only point with correlation higher than 0.30 are reported with the following color order: violet $0.30 < CCC \leq 0.35$, red $0.35 < CCC \leq 0.40$, orange $0.40 < CCC \leq 0.45$

F, for which no direct contact is present. In cluster A the correlation is caused by the Thr41α_1–Arg40β_2 salt bridge present before the first transition. Cluster B is dominated by the water-mediated Asp94α_1–Arg40β_2 salt bridge before the transition at 620 ns which is a weak interaction due to the large distance of ~ 6 Å between the proton and the anion. After the transition this salt bridge becomes the dominant interaction in which Arg40β_2 is involved. The C cluster is instead dominated by the π-stacking interaction between Tyr140α_1 and Trp37β_2. A weak salt bridge between Thr38α_1 and Asp99β_2 side chains with the Thr41α_1 side chain and Asp99β_2 NH peptide bond are responsible for the D cluster. Finally the NH peptide bond of Asn97α_1 and the Asp99β_2 side chain lead to cluster E.

4.3. Hydration Dynamics around Melittin

The approach described above has been extended to the melittin protein (for sequence, see Figure **??**) since it is a well studied prototype of a protein complex that is stabilized through hydrophobic interactions. Melittin is a small, 26-amino acid protein found in honeybee venom that crystallizes as a tetramer, consisting of two dimers, related by a two-fold symmetry axis[51]. Previous work has characterized the behaviour of the hydrophobic binding surface of melittin and the solvent exposed surface residues[41]. While water molecules near the surface residues exhibit a well-defined orientation, water molecules in the hydrophobic regions are more dynamic, exploring different water configurations. Here, similar simulations with a frozen melittin dimer in different box sizes are carried out and analyzed. In additional simulations the protein is also allowed to move freely which provides information about the solvent-solute coupling.

Cheng and Rossky[41] characterized the behaviour of the hydrophobic surface of melittin and of the surrounding surface residues from simulations in which the structure of melittin dimer was frozen. They found that while the latter regions, which are hydrophilic, are

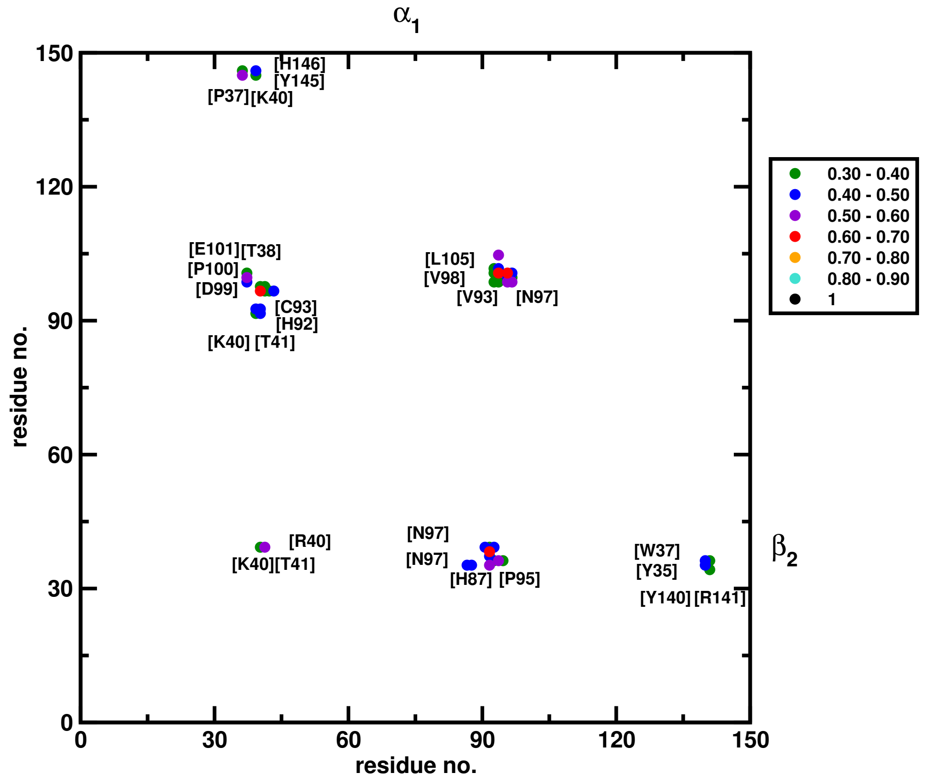

Figure 4.15.: Local Hydrophobicity Cross Correlation Coefficients (C_{ij}) for step1 (0 to 620 ns), for the 120 Å box. The complete Cross Correlation maps for the two time intervals are given in Figure 4.13. Only point with correlation higher than 0.30 are reported with the following color order: green $0.30 < CCC \leq 0.40$, blue $0.40 < CCC \leq 0.50$, violet $0.50 < CCC \leq 0.60$, red $0.60 < CCC \leq 0.70$, orange $0.70 < CCC \leq 0.80$, cyam $0.80 < CCC \leq 0.90$ and black $CCC = 1$

characterized by a well defined orientation of the water molecules, water in the hydrophobic regions are more mobile and explore different water configurations[41]. Given these differences it is of interest to analyze whether $\delta\lambda_{\mathrm{phob}}$ encapsulates similar information, and whether simulations of water around a rigid melittin dimer, as carried out in Ref.[41], and around a flexible dimer lead to qualitatively similar results. Finally, given that the results for Hb depend on the box size, simulations are also carried out with different box sizes.

The structural variations together with the overall hydration for the flexible melittin dimer in the different water box sizes are reported in Figure 4.16. In all simulations the end-to-end separation of the two helices (see Figure 4.16B) as defined by the C_α-C_α separation of the two terminal residues Gly1 and Gln26 is stable and hence the helices remain intact. Consequently, the structural transition that occurs after 80 ns in the 51 Å box (panel C) and appears to occur towards the end of the simulation in the 60 Å box involves the dimerization interface. This is also evident from panel A which reports an increase of the center-of-mass distance $r_{\text{cm-cm}}$ between the two helices at the same time as the RMSD in panel C increases. However, the degree of hydration (panel D) defined as $r_w = N_{\text{rm wat}}/N_{\max}$ (see above) remains essentially constant throughout the simulations.

The protein-water interface is analysed using the same methodology as that used for Hb. The Willard-Chandler interface is calculated setting $r_{\text{cut}} = 25.0$ Å and the likelihood ($\delta\lambda_{\mathrm{phob}}$) of the interfacial water with the reference TIP3P water model is determined with a 6 Å cutoff. Figures 4.17 and 4.18 show the time evolution of selected residues. Figure 4.17 analyses the temporal evolution, $\delta\lambda_{\mathrm{phob}}$, of glycine residues Gly1, Gly3, and Gly12 for chains A and B for both the rigid and the flexible dimers. The $\delta\lambda_{\mathrm{phob}}$ for the rigid dimer is essentially constant, as expected. All results reported are averages over 2 ns windows.

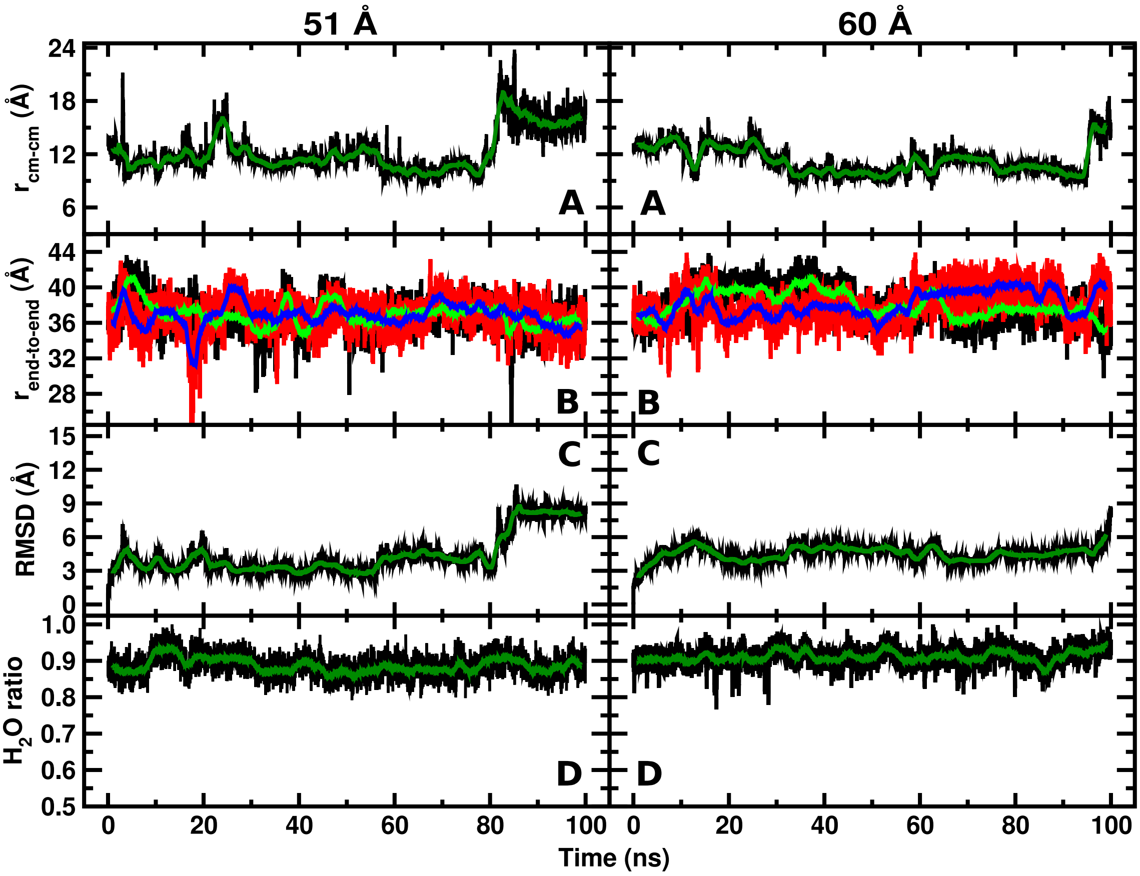

Figure 4.16.: Flexible melittin in the 51 Å and 60 Å boxes. In Panel A the center-of-mass distance between the two monomers ($r_{\text{cm-cm}}$) is reported as function of time (black: raw data; green: moving average). Around 80 nanoseconds, a rearrangement of the two monomers is associated with an increase of $r_{\text{cm-cm}}$. The chain length ($r_{\text{end-to-end}}$) for the two segments (black and red for the raw data for chain A and B, green and blue for their moving average), are illustrated in Panel B. The RMSD with respect to the initial structure for the protein is shown in Panel C. During the time evolution, the number of water surrounding the protein seems not to be influenced by the structural changes (Panel D).

For the rigid monomer (blue traces in Figure 4.17) the LH is constant along the entire 100 ns simulation for both box sizes and the averages differ by 10 % at most (Gly12A). For the flexible dimer (black traces) the instantaneous LH fluctuates around well-defined average values except for Gly12B which has a slightly increased dynamics during the early phase of

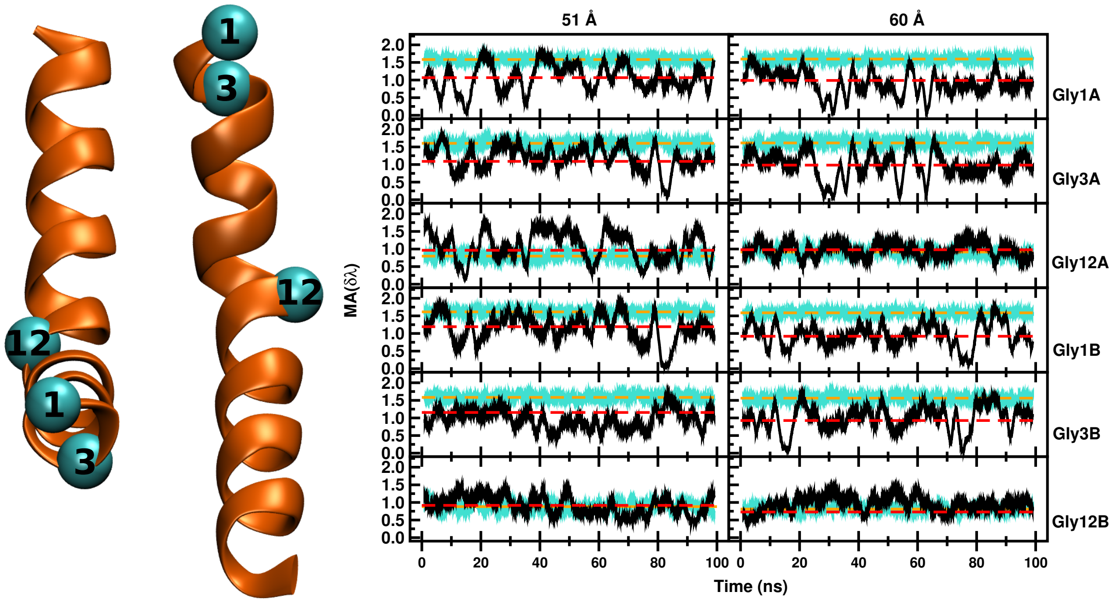

Figure 4.17.: Right: time evolution of $\delta\lambda_{\text{phob}}$ for the 6 glycine residues in the melittin dimer (represented in cyan in the left part of the figure); the left helix is slightly bent at the C-terminal end for the simulations with the rigid (cyan) and flexible (black) peptide. The orange and red line represent the average $\delta\lambda_{\text{phob}}$ for each residue during the simulation. Gly12 is less hydrophilic than the other Gly residues as it is located in the hydrophobic region of the protein. The RMSD of the two chains of the homodimer is 1.6 Å.

Table 4.2.: Average $\delta\lambda_{\text{phob}}$ for the glycine residues for the 100 ns simulation, Figure 4.17.

Residue	51 Å flexible	51 Å rigid	60 Å flexible	60 Å rigid
1A	1.068	1.583	0.989	1.598
3A	1.090	1.604	0.983	1.616
12A	0.965	0.882	0.979	0.945
1B	1.192	1.614	0.921	1.587
3B	1.156	1.584	0.927	1.568
12B	0.917	0.799	0.968	0.826

the simulation. In the simulation in both box sizes the amplitude of LH varies between 0 and 1.5, i.e. between hydrophobic and hydrophilic. As Gly is aliphatic/neutral the changing hydrophilicity must be a consequence of its embedding along the peptide chain and the water structuring around it. Overall, it is found that Gly12 (towards the middle of the helix) is less hydrophilic (see Figure 4.17 and Table 4.2) than Gly1 and Gly3 which are positioned at or near the N-terminus. This difference is more pronounced for the rigid dimer.

Figure 4.18 shows the LH for the residues investigated by Rossky et al.[41]. The average $\delta\lambda_{\text{phob}}$ are neutral or hydrophilic. Good qualitative agreement with Ref[41] is found for residues Val8A (hydrophilic), Leu9A, Ile13A, Ile13B (residues with a decreasing level of hydrophobicity), and Ile20B.

It is also of interest to compare the difference in hydrophobicity for simulations of rigid melittin in the two water boxes because all differences found must arise from the size of the water box. Figure 4.19 shows the difference in LH of the residues in the hydrophobic pocket between the 51 Å and the 60 Å boxes. The average fluctuations are of the order of 0.1 units with maximum differences of 0.4 units. The difference between simulations with rigid and flexible melittin can also be seen when comparing radial distribution functions $g(r)$ between C_α atoms of selected residues and water and the corresponding

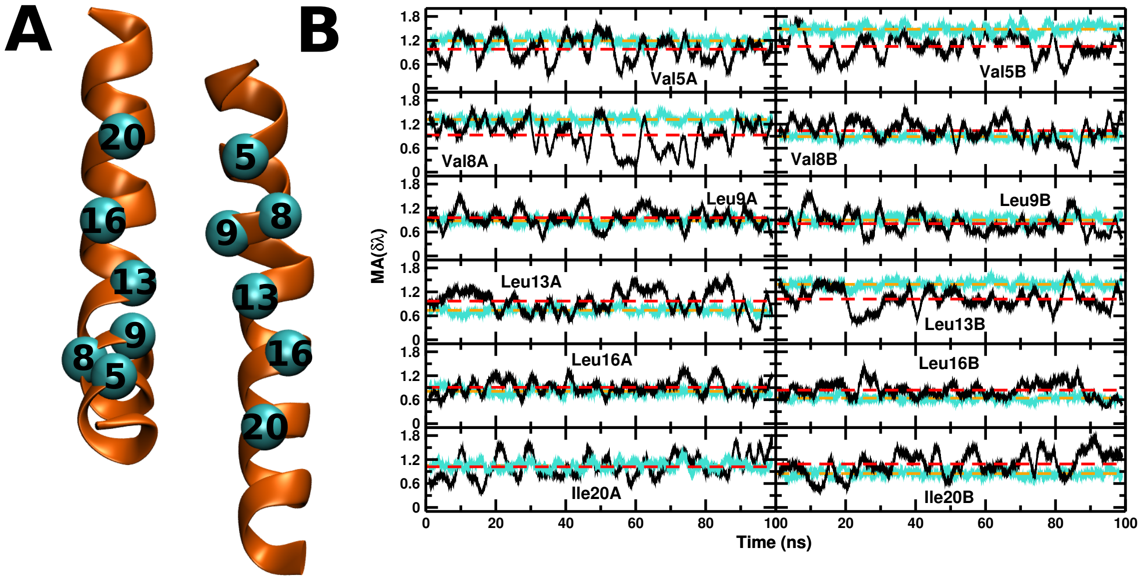

Figure 4.18.: Local hydrophobicity (LH) as a function of time for the rigid (cyan) and flexible (black) melittin in the 51 Å simulation. Left column for residues in chain A, right column in chain B. Orange and red dashed lines are averages for rigid and flexible melittin, respectively. The protein structure is represented on the left side with the studied residues in cyan.

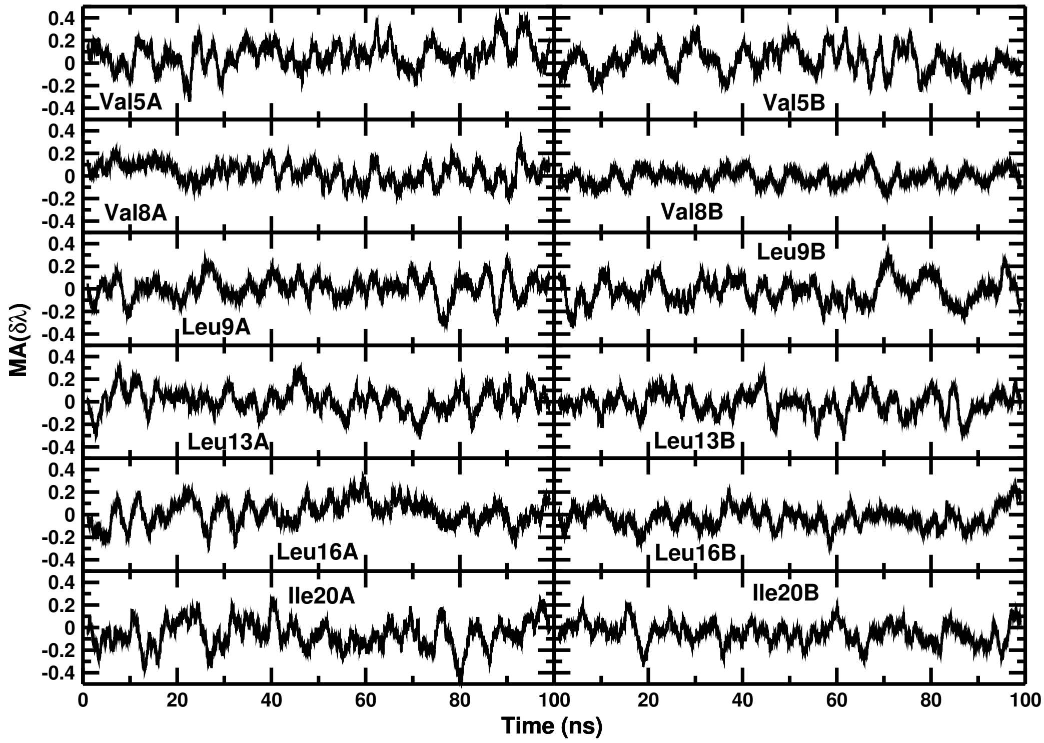

Figure 4.19.: Difference in hydrophobicity for the residues in the melittin dimer hydrophobic pocket (residues Val5, Val8, Leu13, Leu16, Ile20) for the rigid simulations in the 51 and 60 Å boxes. The data reported is $\Delta\delta\lambda = \delta\lambda_{60} - \delta\lambda_{51}$, i.e. the change in LH from the simulation in the two water boxes. The change in $\Delta\delta\lambda_{\mathrm{phob}}$ due to the box size is up to 40%.

water occupations $N(r)$, see Figures 4.20 and 4.21. The residues were chosen according to the results from Table 4.3. For example, in the 51 Å box for rigid melittin the values for Val5A and Val5B are $\delta\lambda_{\text{phob}} = 1.19$ and 1.48, respectively, which change to 1.25 and 1.49 in the larger 60 Å box, i.e. a change of 5 % at most. On the other hand, Figure 4.20A suggests that the $g(r)$ for Val5A and Val5B are very similar for both water box sizes. This suggests that the difference of ~ 0.3 for each water box must arise from the orientation of the water molecules within the 6 Å cutoff.

Conversely, for flexible melittin the differences for LH in the two water boxes can be substantial. As an example for Leu9B $\delta\lambda_{\text{phob}}^{51\text{Å}} = 0.81$ compared with $\delta\lambda_{\text{phob}}^{60\text{Å}} = 1.07$ for the two box sizes. This is also evident from Figure 4.21A and B (right panel) for which $g(r)$ and $N(r)$ have increased amplitudes for the larger water box. On the other hand, for Val5B $\lambda_{\text{phob}}^{51\text{Å}} = 1.05$ is larger than $\lambda_{\text{phob}}^{60\text{Å}} = 0.86$ whereas the amplitude of $g(r)$ up to the 6 Å cutoff in the larger box is larger than that in the smaller box. Hence, again, the difference in the two box sizes must be in the angular orientations of the water molecules relative to the protein surface.

These analyses suggest that both, the distance-dependent part (reflected in $g(r)$ and $N(r)$) and the angular orientation, as measured by λ_{phob}, may differ depending on box size and potentially influence the thermodynamic stability of the two proteins.

The average hydrophobicity for each residue during the simulation is reported in Figure 4.22A (black for chain A and red for chain B). The decreased hydrophobicity of the central part of the chains (from Val5 to Leu16) is highlighted by the lower $\delta\lambda$ (of $0.1{-}0.2$ units) compared with the C- and N-terminal parts.

The main difference between simulations of the flexible (left) and rigid (right) melittin

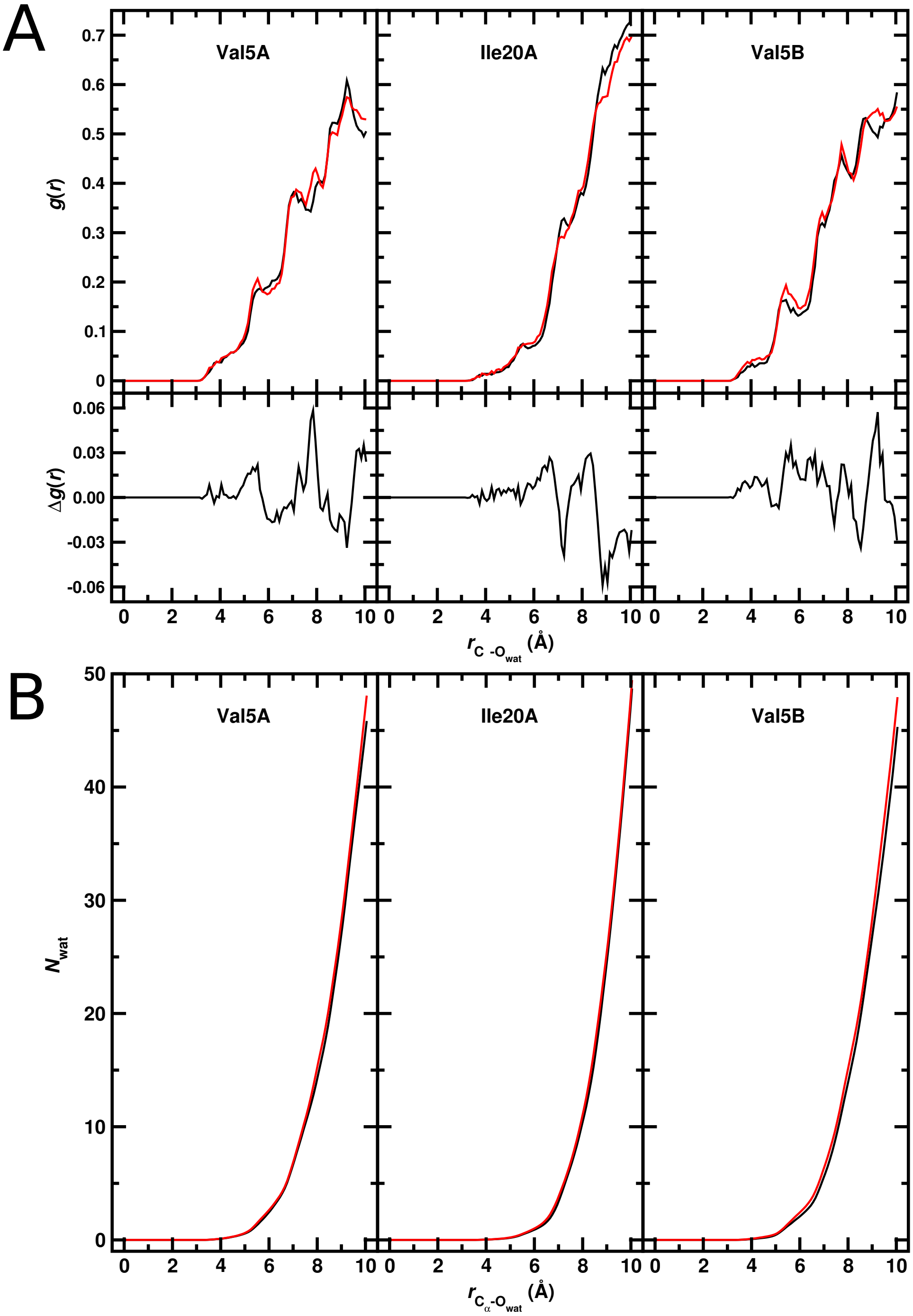

Figure 4.20.: Panel A: The radial distribution functions $g(r)$ between water-oxygen atoms and the C_α of Val5A, Ile20A and Val5B for *rigid* melittin in the two water boxes. The top panels show the $g(r)$ for the 51 Å (black) and 60 Å (red) boxes and the bottom panels show the differences between the two. Panel B: The number of water molecules up to distance r, $N(r)$, from the $g(r)$ in panel A. The same color code as in panel A is used. All differences are due to the different water box sizes.

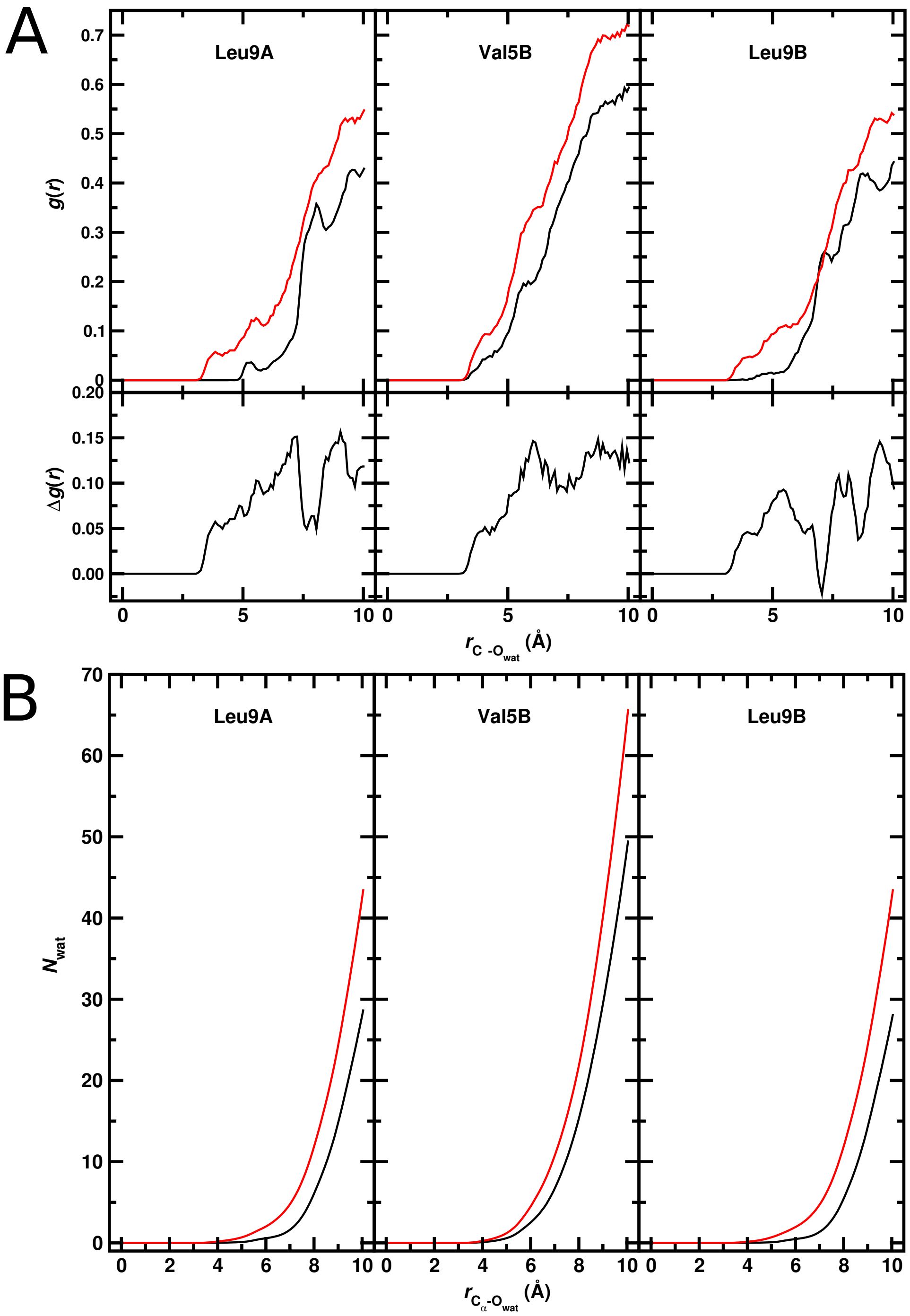

Figure 4.21.: Panel A: The radial distribution functions $g(r)$ between water-oxygen atoms and the C_α of Val5A, Ile20A and Val5B for *flexible* melittin in the two water boxes. The top panels show the $g(r)$ for the 51 Å (black) and 60 Å (red) boxes and the bottom panels show the differences between the two. Panel B: The number of water molecules up to distance r, $N(r)$, from the $g(r)$ in panel A. The same color code as in panel A is used. The differences are due to both, the different water box sizes, and the coupled protein-water dynamics.

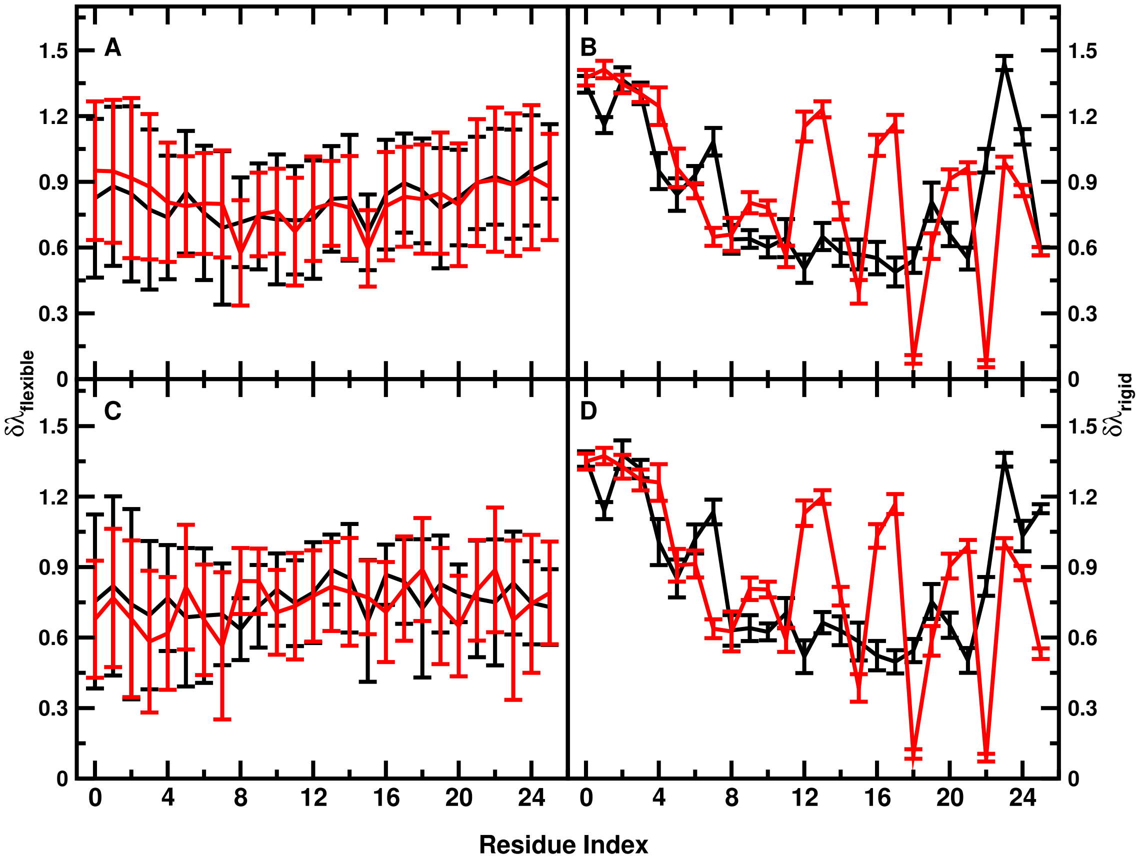

Figure 4.22.: Average $\delta\lambda$ with respective variation during the dynamics per residue for the 100 ns for chains A (black) and B (red) for flexible (panels A and C) and rigid (panels B and D) melittin dimer. The top row is for the 51 Å box and the bottom row for the 60 Å box. The value of the LH ranges from $0.50 < \delta\lambda < 1.00$ for the flexible dimer and between $0.00 < \delta\lambda < 1.50$ for the rigid dimer. For the rigid dimer, the central part of the A-helix has consistently lower values of LH compared with the C- and N-terminal parts. For chain B larger variations in LH are found for some of the residues due to its different structure. The periodicity of the red traces (panels B and D) reflects the helical structure which is apparent for monomer B but less so for monomer A. For flexible melittin the variation of LH along the sequence is much smoother than it is for rigid melittin as a consequence of dynamical averaging.

dimer is the amplitude of the fluctuation of the hydrophobicity, but not its sign. Simulations of rigid melittin in the 51 Å (panels A and B) and 60 Å boxes (panels C and D) are similar to one another but they differ along the trajectory by up to $\Delta\delta\lambda \sim 0.4$ (see Figure 4.19). There are also differences between the A (black) and B chains (red) for rigid melittin. The difference in the monomer structures (RMSD of 1.6 Å) apparently also leads to significant differences in $\delta\lambda$ (see Figures 4.22A and B. As an example, Leu13A is considerably more hydrophobic ($\delta\lambda_{\mathrm{Leu13A}} = 1.2$) than Leu13B ($\delta\lambda_{\mathrm{Leu13b}} = 0.7$). Inspection of the dimer structure shows that Leu13A points toward the dimerization interface whereas Leu13B points away from it into the solvent. For flexible melittin (panels A and C), the LH for the A and B chains is more similar to one another for both box sizes. This occurs as a consequence of averaging along the structural dynamics and also suggests that simulations on the 100 ns time scale are sufficient to largely converge $\delta\lambda$ for melittin. Nevertheless, there remain certain differences between simulations in the two water boxes for individual residues, e.g. $\langle \delta\lambda^{51}_{\mathrm{Val5B}} \rangle = 1.05$ vs $\langle \delta\lambda^{60}_{\mathrm{Val5B}} \rangle = 0.86$, see Figure 4.22 and Table 4.3.

Finally, the two-dimensional LH-CCM (see Figure 4.23) for all four systems have been determined. For the flexible dimer increasing the box size leads to more pronounced cross correlation peaks between the beginning of monomer A and the end of monomer B (upper left quadrant). A slightly less pronounced increase in the correlation is found for the end of chain A and the beginning of chain B.

With regards to the rigid dimer the differences between the two box sizes also occur as shown in the ΔCCC map (bottom panel in Figure 4.23). These differences are due to the two different box sizes. They affect the local hydrophobicity which is computed from the water structuring. Hence, the average water orientation near the (rigid) protein surface differs depending on the box size. For the simulations in which the dimer is flexible, the

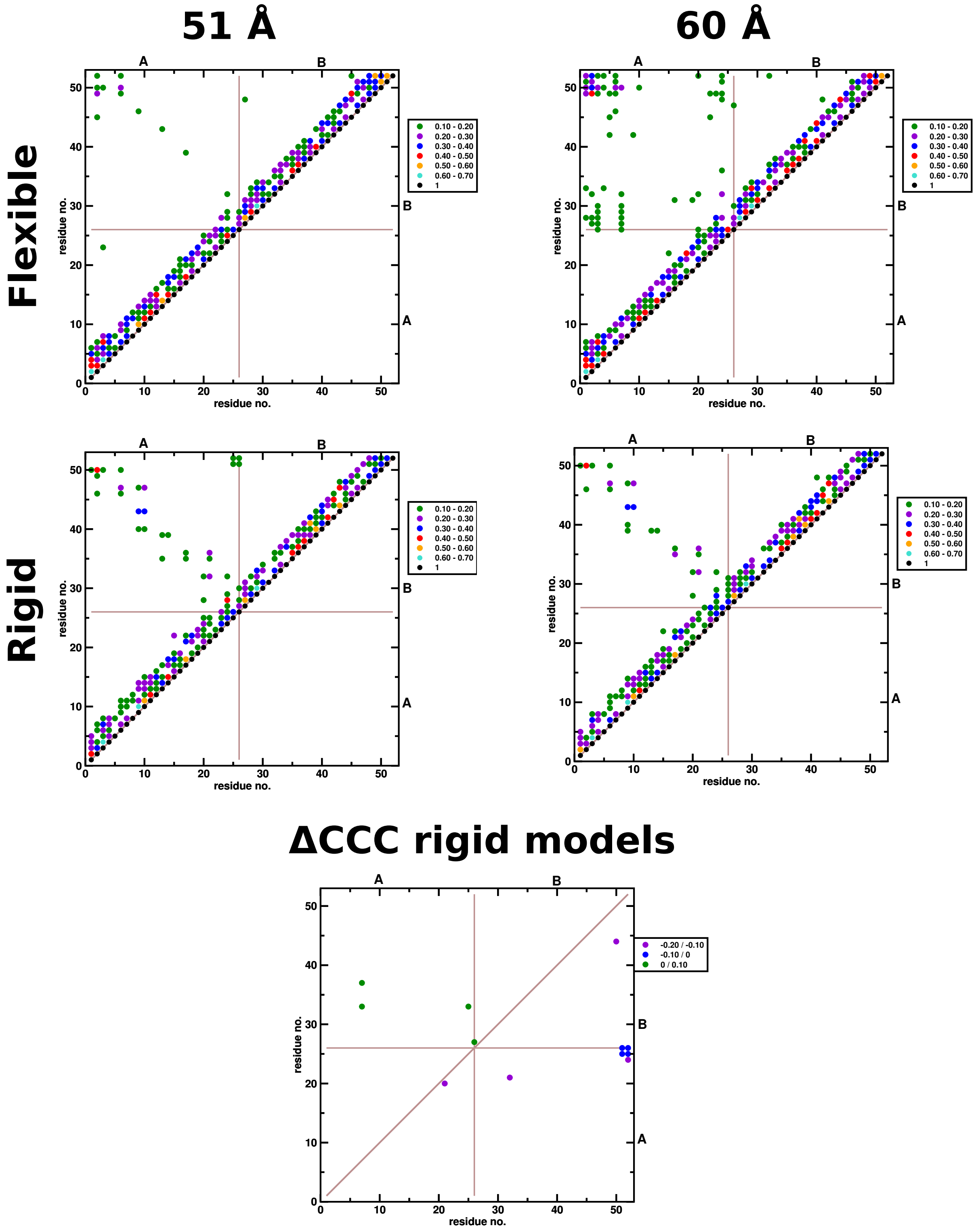

Figure 4.23.: Cross Correlation Coefficients for local hydrophobicity $\delta\lambda_{\mathrm{phob}}$ (with values larger than 0.1) for flexible (top) and rigid (bottom) melittin dimer in the 51 Å (left) and 60 Å (right) box sizes. In all plots, traces from the secondary structures are observed. In the last graph the difference between the two rigid models is shown: positive value are on top of the diagonal, while negative values are in the bottom of it.

Table 4.3.: Average $\delta\lambda_{\mathrm{phob}}$ for the hydrophobic residues from Figure 1 in Ref.[41]. The time series are shown in Figure 4.18.

Residue	51 Å flexible	51 Å rigid	60 Å flexible	60 Å rigid
Val5A	0.976	1.185	1.003	1.246
Val8A	0.929	1.322	0.941	1.375
Leu9A	0.954	0.875	0.889	0.876
Leu13A	0.967	0.741	1.030	0.756
Leu16A	0.909	0.808	0.917	0.824
Ile20A	1.019	1.049	1.071	0.992
Val5B	1.046	1.484	0.861	1.494
Val8B	1.038	0.889	0.806	0.877
Leu9B	0.814	0.900	1.071	0.867
Leu13B	1.016	1.393	1.006	1.373
Leu16B	0.835	0.637	1.012	0.626
Ile20B	1.087	0.845	0.988	0.824

situation is more complicated. There are simultaneous effects of both the water dynamics and structure and protein dynamics.

4.4. Conclusions

The present chapter analyzed the local hydrophobicity around key residues at the protein interfaces for hemoglobin and melittin. It is found that the local hydrophobicity measure provides valuable insight into the effect of different box sizes in molecular dynamics simulations of hydrated proteins.

In case of Hemoglobin, a clear association between the change of hydrophobicity and the transition between the different states is observed. The average hydrophobicity for small boxes is higher than the 150 Å box simulation, proving that a difference in the solvation exists for different box sizes. The study of the time evolution allows to identify which region of the protein is active during a transition. It can provide an important methodological tool for understanding phase transitions in protein system when change of solvation are involved.

For simulations performed on Melittin, the local hydrophobicity studies confirms the previous findings from Cheng and Rossky[41]. However simulations performed on the flexible protein show a dynamical averaging during the simulation, suggesting that the system tend to assume a conformation that tends to minimize the difference in hydrophobicity. Comparison between simulations of different size systems shows that the change in hydrophobicity can be both in the orientation of the water around a residue, as in case of Val5B in the rigid simulations for the 51 Å and 60 Å boxes, and the effective change in the box size, as in case of Leu9A for the flexible simulations.

Following studies can be performed using this characterization of local hydrophobicity for exploring how the protein is directly influenced by the solvent behaviour.

Part IV.

Conclusion and Outlook

In this thesis interactions of water interfaces behaviour at different conditions were examined. At first, conditions for oxygen formation on top of amorphous solid water were studied, constructing a complex model, and then the interaction between water and two different proteic system was studied under ambient condition.

Conditions for forming O_2 are first considered. Initially, the possible diffusion quantum effects for oxygen atoms were ruled out. Experiments have shown that atomic diffusion on top of the water surface are faster than what estimated by the Arrhenius equation. Both nuclear quantum dynamics and the use of an appropriate model for rough surface shows that diffusion is purely classical. The surface is characterized by a series of cavities with different diffusion energies, allowing multiple paths that reduce its average value. Consequently, the energetic aspects of the O_2 recombination have been studied, first inside the water ice and then on the top of the surface: the first set of simulations was used for tuning the conditions for surface formation. The timing for the relaxation is observed under different parametrizations. In all simulations, the relaxation times are expected to be under the microsecond time scale while the importance of using water flexible force fields, a factor of four of difference is observed between the two models.

The final section inspects oxygen formations from a photochemical point of view. Since O_2 recombines in three different electronic states with different reactivity, the Landau-Zener algorithm was implemented to count the redistribution of the rebound molecule between the different states. An equal redistribution within the three first electronic state was found, meaning that the $\sim 70\%$ was formed in a highly reactive state on top of the surface. Having also observed that no desorption occurs during the simulation time scales, this indicates that oxygen is available to undergo under other chemical reactions. The sapient combination between kernels and molecular dynamics allows as well to vastly explore photochemical processes at longer time scales that are allowed from *ab initio* calculations.

The stability of protein is observed at different box sizes. At first, the stability of hemoglobin, studied in Ref[37], is analyzed in terms of single amino-acid hydrophobicity. The collapse of the T_0 state in the 90 Å and 120 Å boxes is associated to the C-terminal to a gradual change of hydrophobicity positioned in key regions of the protein, precisely the C-terminal residues and the ones at the α_1/β_2 and α_2/β_1 interfaces. These changes happens on a $\sim$ 50 ns timescale. The algorithm is tested on 100 ns simulation on the melittin dimer. In this system no change of hydrophobicity is observed during simulations, even if indirect hints of box size effect are observed. Rearrangement of the chains tends to preserve the hydrophobic regions from water penetrating inside.

An important aspect that came out from this thesis is the importance of using knowledge from different fields for new problems. For example the Zwanzing equation, needed for describing the protein folding along the protein funnel, is useful for exploring the diffusion of rough surfaces, thanks to the similarities between the two problems.

The techniques explored in this thesis can be used to approach more complex chemical systems in different environments. For astrochemical-related problems, classical MD and MC simulations of adsorbate species on grain's surface will provide an extensive and inexpensive exploration of the surface itself, allowing for more correct estimations of the diffusion and desorption energies, both with classical force field or with most sophisticated models, as kernels or neural network based models. All this data will then flow on the studies of more complex systems like complex organic molecules, amino-acid and sugars, clarifying their synthetic pathways both in terms of thermodynamics and kinetics. Hydrophobicity contributions will also allow the identification of specific regions of a surface allowing the optimization of the initial conditions in patched surfaces for chemical reactions: the surface can be engineered to enhance the product state over the reactants.

The amorphous surface characterization protocol presented here can be implemented for electrochemistry by exploring morphologies using sample particles, identifying patterns associated that enhance catalytical turnover and the relative stability conditions of the species involved. This can be used to optimize the experimental conditions in which catalyst are synthesized and how do they perform.

The implementation of nonadiabatic transition in O_2 with the kernel formalism can be generalized to perform simulations on complex molecules. This will offer another important tool in atmospheric chemistry, where molecules populating the excited states are needed for having a complete vision of the reaction network. With proper modulation between the QM/MM interface the Landau-Zener formalism can be used to approach biologically relevant problems, for example when electronic transitions in chromophores are involved.

Part V.

Appendix

5. A distributed charge approach to molecular dynamics simulations models

Portability of a force field is not guaranteed from one MD engine to another, because the same interatomic interaction can be described using different functional forms. As a consequence, the comparison of the same quantity leads to different results. The electrostatic interaction is a clear example of this issue as different models, from mere point charges, multipoles and polarizabilities are implemented. The distribute and minimal distribute charge models (DCM and MDCM, shorted as (M)DCM)[52,53] are candidates to reproduce different electrostatic models thanks to its flexibility in the same MD engine.

In this piece of work, made in collaboration with Dr. Michael Devereux the (M)DCM model is tested for reproducing the water-water interaction from the iAMOEBA force field (FF) in OpenMM. The iAMOEBA FF is the state of the art force field for reproducing the thermodynamical properties of liquid water and it is implemented in Tinker[54] and OpenMM[55]. The main strength of the iAMOEBA force field is its ability to properly reproduce the electrostatic properties of water[56]. Electrostatic interaction is reproduced using a polarizable model derived from the static multipoles. Details on these methods can be found in Section **??**. Due to discrepancies between the engines (for example the implementation of Ewald summation cutoff, use of the 14-7 Lennard-Jones instead of the classical 12-6 formulation and different cut-off schemes) the direct implementation of iAMOEBA force field in CHARMM does not reproduce the dynamical results of water bulk, i.e. densities ρ and self diffusion coefficient (D). In Table 5.1 bulk properties of liquid water are reported at ambient conditions (298 K and 1 atm) for different models.

Table 5.1.: Bulk properties of liquid water at 298 K and 1 atm, for experimental, TIP3P, iAMOEBA values for DCM and iAMOEBA in OpenMM.

	ρ (g/cm^3)	D 10^{-5}cm^2/s
Exp.[a]	0.996	2.3[b]
TIP3P[c]	1.027	3.9
iAMOEBA/DCM	0.958	3.6
iAMOEBA/OpenMM[d]	0.997	2.5

[a] Ref.[57]; [b] Ref.[58]; [c] using conventional TIP3P in CHARMM; [d] Ref.[56]

5.1. iAMOEBA/(M)DCM in OpenMM

In this section the implementation of iAMOEBA FF *via* (M)DCM in OpenMM is discussed. In the first part the correspondence between the local axis system in the two models is presented, followed by comparison of this model with the original with both static calculations and molecular dynamics simulations.

As first step, the translation of the axis system from the iAMOEBA multipoles to the two (M)DCM models is established. In iAMOEBA FF, the oxygen and hydrogen of water are described by two different axis system. The water's oxygen is described by a *bisector axis system*, where the oxygen dipole moment points along the bisector of the the $\angle_{\mathrm{HOH}}$ angle[59]. The two hydrogen atoms are described by *bond axis system*, with the main axis pointing along the OH bond, the secondary axis along the hydrogen-hydrogen vector and the third perpendicular to the molecular plane[59]. All atomic dipole moments lie on the molecular plane. In the DCM module a combination of six charges per atom are used for reproducing the total quadrupole moment from iAMOEBA. The local axis system is identical for the two hydrogen atoms but not for the oxygen where a rotation is needed. In the MDCM model the electrostatic potential is reproduced using any number of charges per molecule. As a consequence an arbitrary accuracy can be reached changing the amount of charges at cost of a computational overhead. The model is built fitting the iAMOEBA electrostatic potential (ESP) using the Fitting Wizard interface[60]. In both models the limit of one charge per atom in OpenMM is overcome using dummy atoms. Their position is determined using the position of three real atoms of the system, similarly to the bond axis system. Figure 5.1 shows how charges are distributed in the two models and Figure 5.2 shows the local axis system for iAMOEBA, (M)DCM and OpenMM models.

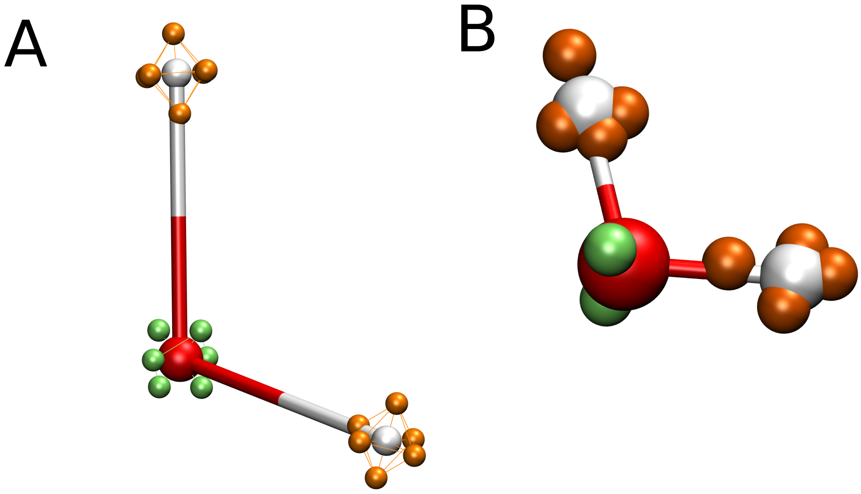

Figure 5.1.: Charge distribution in the water DCM model (A) and MDCM with 10 charges (B). Green charges are assigned to oxygen while orange charges are assigned to hydrogen.

Another necessary step was to correct the polarization (α) term in OpenMM for the distribute charge implementation, as the polarization needs to be redistributed between the charge sites. It was found that assigning $\alpha = \alpha$ for the nuclei and $\alpha = \alpha \cdot 10^{-4}$ for each virtual site properly reproduce the original iAMOEBA FF.

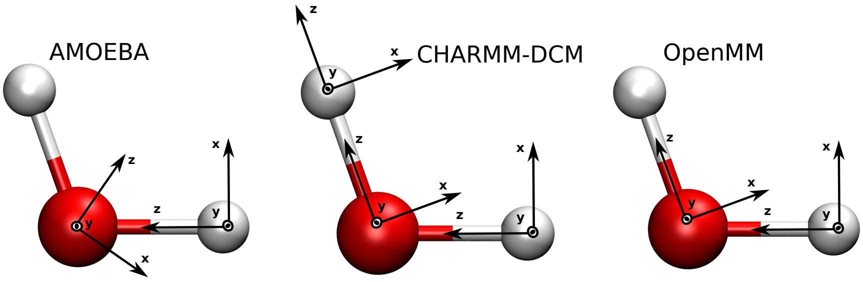

Figure 5.2.: Local reference axis sytem for iAMOEBA, (M)DCM and OpenMM models. In all cases the $z-$axis is the main axis and the molecule is in the xz-plane.

For both iAMOEBA/DCM and iAMOEBA/MDCM, the validity of the electrostatic interaction is tested using structures of water dimers from the Tschumper's dataset[61] and minimal structures from oligomers (see Figure 5.3). Table 5.2 shows the energies between the original iAMOEBA FF and iAMOEBA/DCM. A good agreement is found between the two models, with a maximum error of 0.74 kJ/mol and a mean absolute error (MAE) of 0.17 kJ/mol. Results for iAMOEBA/MDCM are in Table 5.3: the trade of using fewer charges, 10 instead of 18, leads to small increase of the errors, with a maximum error of 1.91 kJ/mol and mean absolute error of 0.45 kJ/mol. In both cases the models are within the chemical accuracy of 4.0 kJ/mol (~ 1 kcal/mol).

Thermodynamical properties are estimated performing molecular dynamics simulations at different conditions in the NPT ensemble with a Langevin integrator coupled with a Monte Carlo barostat on a 25 Å edge cubic box of 500 water molecules. A steepest descent minimization of 100 steps is followed by 5×10^4 steps of equilibration and 2×10^6 steps of dynamics with $\Delta t = 0.5$ fs. Electrostatic contributions are evaluated using the Particle Mesh Ewald algorithm with 7Å radial cutoff and 9 Å for the van der Waals interaction. Three different simulations are considered: iAMOEBA, iAMOEBA/DCM and iAMOEBA/MDCM. A perfect overlap of the radial distribution function is observed

Table 5.2.: Comparison between iAMOEBA energies and its respective DCM polarized model. In the top part of the table, energies for the 10 dimer structures are shown, while in the bottom part energies for various oligomers are presented. The mean absolute error for the dataset is within the chemical accuracy (MAE=0.173 kJ/mol).

Dimer	iAMOEBA (kJ/mol)	DCM-iAMOEBA (kJ/mol)	ΔE (kJ/mol)
1	-21.393	-21.306	0.087
2	-18.848	-18.960	-0.112
3	-18.845	-19.055	-0.207
4	-16.001	-15.768	0.233
5	-13.679	-13.458	0.221
6	-12.434	-12.413	0.021
7	-13.386	-13.274	0.112
8	-6.579	-6.608	-0.029
9	-15.874	-15.807	0.067
10	-12.619	-12.666	-0.047

Oligomer	iAMOEBA (kJ/mol)	DCM-iAMOEBA (kJ/mol)	ΔE (kJ/mol)
trimer	-57.612	-57.282	0.330
tetramer	-102.626	-102.485	0.141
pentamer	-135.228	-135.053	0.281
hexamer prism	-173.462	-173.304	0.158
heptamer	-214.633	-214.188	0.445
octamer	-270.584	-269.841	0.743
nonamer	-304.993	-305.379	-0.386
decamer	-346.670	-346.310	0.360

Table 5.3.: Comparison between iAMOEBA energies and its respective MDCM with 10 charges polarized model. In the top part of the table, energies for the 10 dimer structures are shown, while in the bottom part energies for various oligomers are presented. The mean absolute error for the dataset is within the chemical accuracy (MAE=0.451 kJ/mol).

Dimer	iAMOEBA (kJ/mol)	DCM-iAMOEBA (kJ/mol)	ΔE (kJ/mol)
1	-21.393	-21.441	-0.048
2	-18.848	-18.680	0.168
3	-18.845	-18.708	0.137
4	-16.001	-16.049	-0.048
5	-13.679	-13.306	0.373
6	-12.434	-11.979	0.455
7	-13.386	-13.373	0.013
8	-6.579	-6.638	-0.059
9	-15.874	-15.773	0.101
10	-12.619	-12.659	-0.040
Oligomer	iAMOEBA (kJ/mol)	DCM-iAMOEBA (kJ/mol)	ΔE (kJ/mol)
trimer	-57.612	-57.661	-0.049
tetramer	-102.626	-102.238	0.388
pentamer	-135.228	-134.999	0.229
hexamer prism	-173.462	-172.997	0.465
heptamer	-214.633	-213.918	0.715
octamer	-270.584	-268.768	1.816
nonamer	-304.993	-303.242	1.751
decamer	-346.670	-344.764	1.906

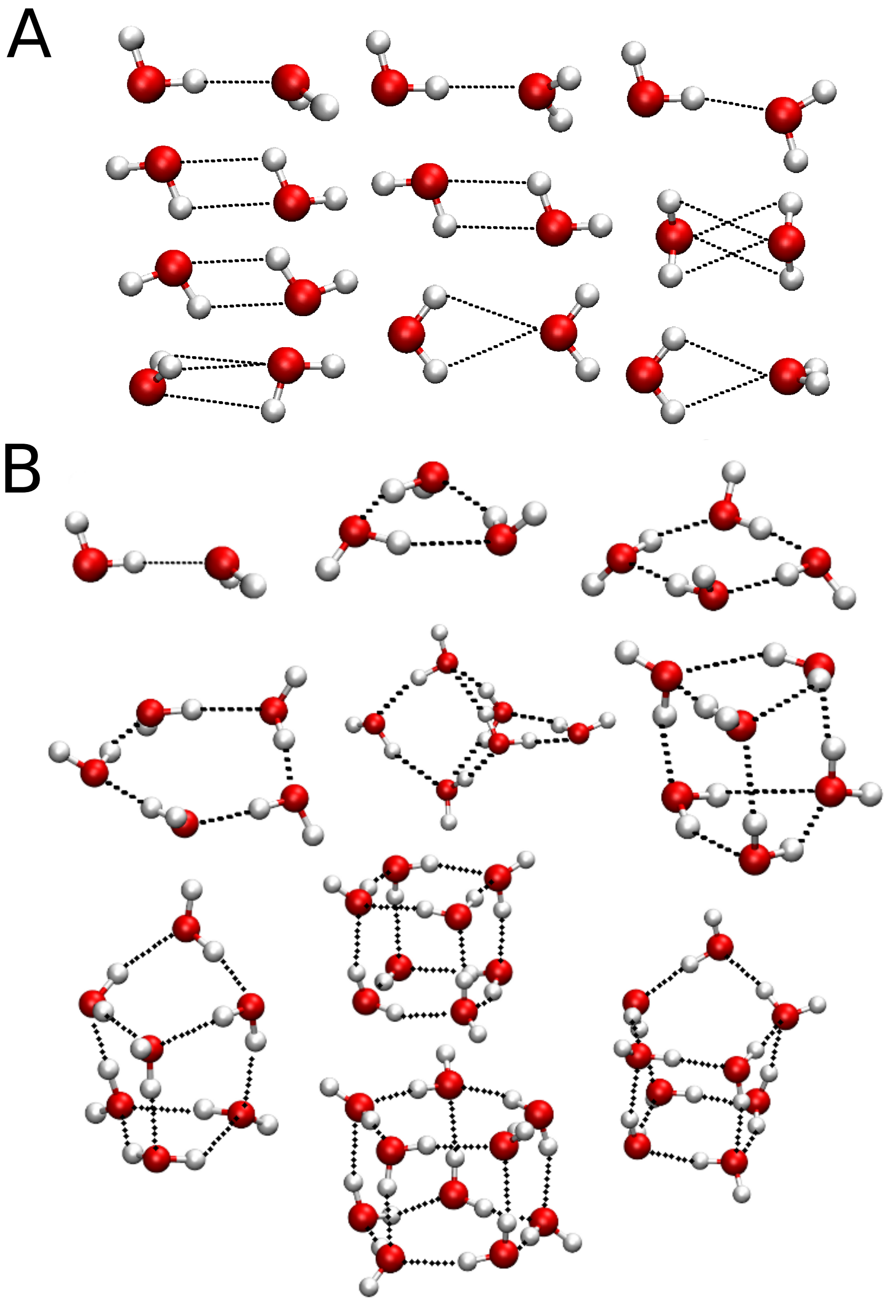

Figure 5.3.: Dimer structure from Tschumper's dataset[61] (A) and oligomers minimum structures (B).

when the constrains are active, but the activation of the constrains leads to an underestimation of the first and second peaks, see Figure 5.4.

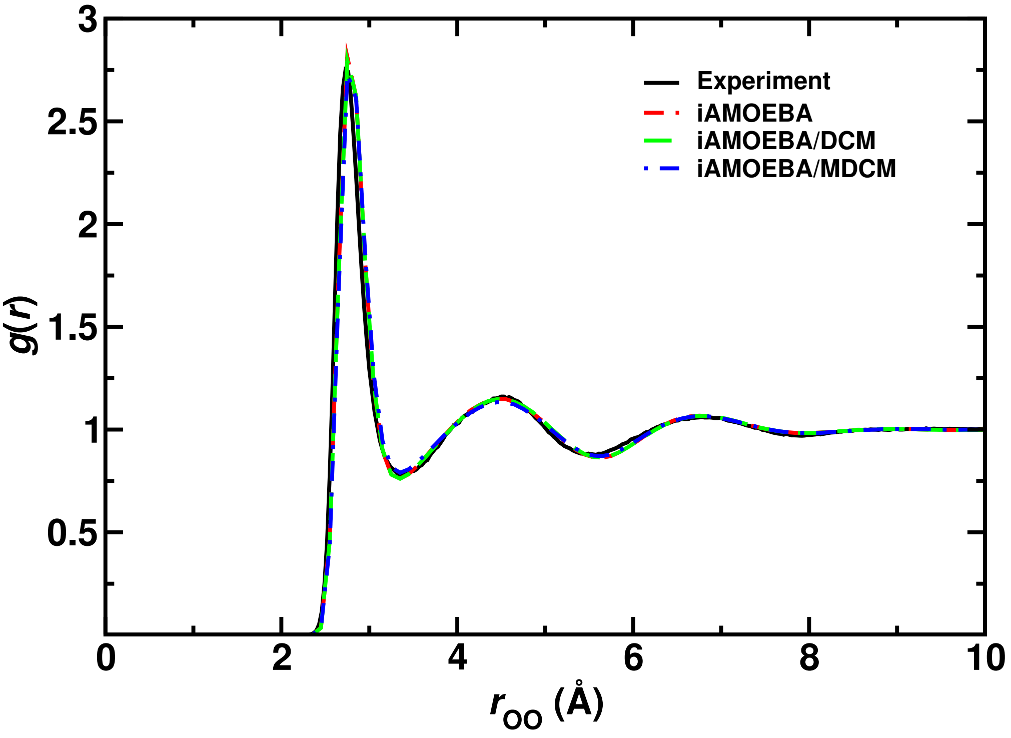

Figure 5.4.: Radial distribution function ($g(r)$) for the water bulk simulation performed in OpenMM. Showing in black the experimental data, in red the simulations with iAMOEBA FF, in green the simulations with iAoeba/DCM and in blue the iAMOEBA/MDCM model.

The agreement between simulations implies that the models are identical within the chemical accuracy. It is expected that with a proper implementation of the (M)DCM code on the OpenMM engine should improve the simulations' performances.

6. Contributions in CHARMM

In this chapter the two contribution programmed in CHARMM are presented. They can be respectively found is in the **EXTBOND** and **TRIAKERN** modules. Both methods are meant to be used as force field terms for reactive dynamics for spectroscopy purposes. For each of the implementation, the usage and some examples will be discussed. Both implementations can be found in CHARMM starting from the c45a2 version.

6.1. EXTBOND

EXTBOND provides additional bond potential forms, beside the usual harmonic one naturally implemented in CHARMM. The module works by substituting the harmonic potential of a bond defined in the force field with a new potential intended for reactive and spectroscopic applications. EXTBOND can add as well new bonds, not explicitly defined in the topology or parameter file of CHARMM which only exist for the duration of a CHARMM run.

The command is invoked using the keyword XTBD and has three possible options:

- **Addition:** A new bond between a first and second is added to the list of existing bonds. It is invoked by the ADDI keyword.
- **Replacement:** An existing bond between two atoms is substituted by one of

available potential. It is invoked by the REPL keyword.

- **Cleaning:** Remove the list of added and substituted bond previously defined. It is invoked by the CLEA keyword.

The keyword READ can be used instead of the previous ones for reading an external file containing information on the replacement and addition of new bonds.

There are five possible potentials implemented in EXTBOND. The first option, invoked by the HARM keyword allows the use of new potential of the form of classical CHARMM potential. The command MORS invokes the Morse potential, as described in Equation **??**.

The AMOE keyword invokes the MM3 anharmonic quadratic potential implemented in Amoeba[62]. The form of the potential is:

$$E_{\mathbf{b}}^{\mathbf{MM3}} = k\left(r - r_0\right)^2 \left(1 - 2.55\left(r - r_0\right)\left(1 - \frac{7}{12}\left(r - r_0\right)\right)\right) \tag{6.1}$$

r and r_0 are respectively the interatomic distance and the equilibrium distance between the two atoms and k is the equilibrium constant. This potential is useful for reproducing spectroscopic data.

The quartic potential, invoked using QUAR command, has a form similar to the MM3 potential but it is more flexible, having an user defined cubic (k_3) and a quartic constant (k_4) for the energy evaluation. The potential has the following form:

$$E_{\mathbf{b}}^{\mathbf{QUAR}} = \left(r - r_0\right)^2 \left(k + k_3\left(r - r_0\right) + k_4\left(r - r_0\right)^2\right) \tag{6.2}$$

At last the RKHS potential is implemented by the keyword RKHS. The description of the RKHS formalism is given in Section **??**. In order to perform calculations with the RKHS

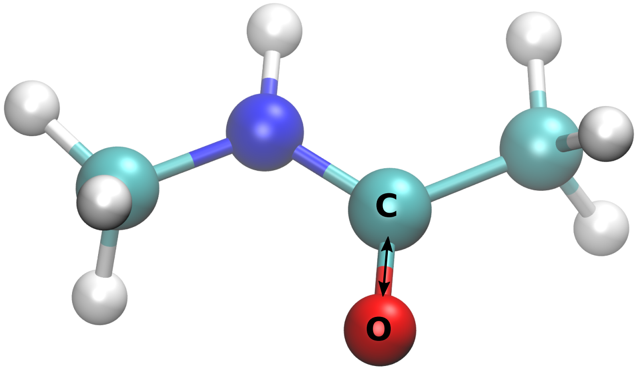

Figure 6.1.: Structure of N-methylacetamide (NMA). The arrow shows the bond treated using the EXTBOND/RKHS potential

potential, an ordered grid of distances and energies has to be given in the form of a *csv* file, together with the asymptotic energy for the bond. A possible way to obtain energies is performing an *ab-initio* scan along the bond under exam. The asymptotic energy is need for referencing the energies to the asymptote, $E - E_{asymp}$, such that $E(r_{asymp}) = 0$. This condition is required for having the correct behaviour of kernels at long distance.

The validity of the algorithm is tested for the O_2 PES tested in Chapters 2, on the N-methylacetamide (NMA, represented in Figure 6.1) and for the helium dimer (He_2). For both NMA and He_2 *ab-initio* calculations are performed using the MP2/aug-cc-pVTZ level of theory. In the case of NMA a recovery of the CO stretching respect to classic force field is recovered, passing from 1950 cm^{-1} from the CHARMM FF to 1640 cm^{-1}. The disagreement with accepted results[63] (1725 cm^{-1}) can be explained due to the lack of coupling between the molecular modes.

In case of He_2, a 50 ps simulation in gas phase at 15 K is performed and from it the vibration spectrum is reproduced. A good agreement is found between the RKHS potential and MP2/aug-cc-pVTZ frequencies with an uncertainty of 1 cm^{-1}, as seen in Figure 6.2.

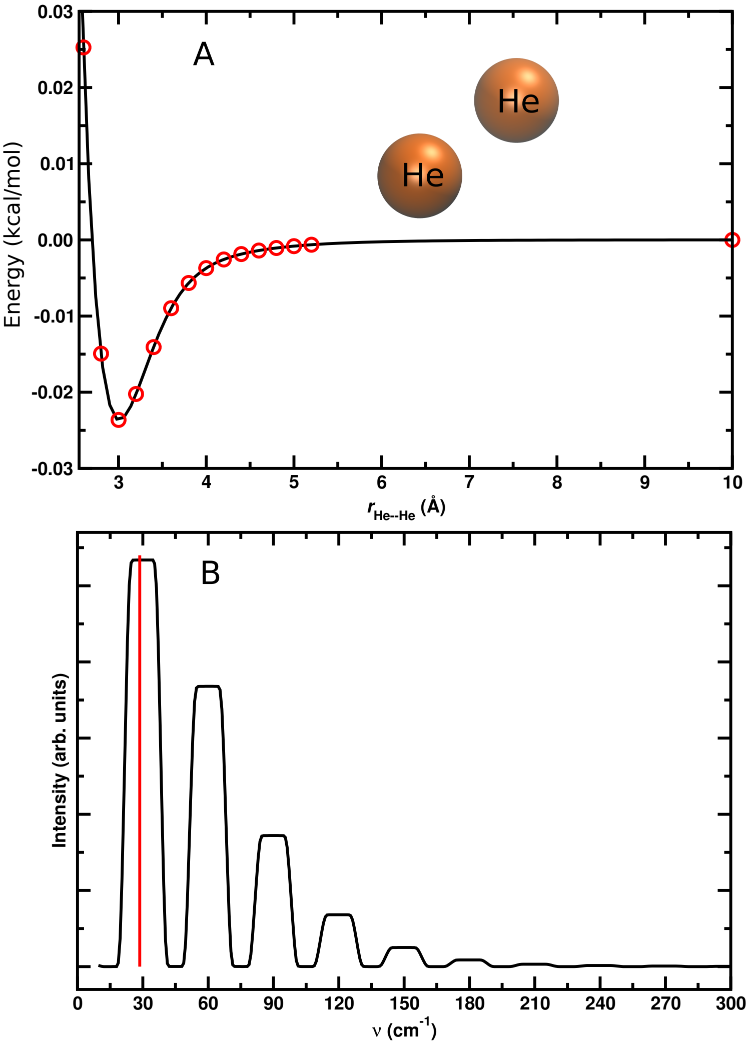

Figure 6.2.: Panel A: The interatomic potential of two helium atoms. Panel B: The vibrational progression of the He_2 cluster with the main peak at 28.6 cm^{-1}.

6.2. TRIAKERN

The TRIAKERN module provides an additional potential form for triatomic systems, beside the combination of two bonds and bending term provided in CHARMM. The main purpose of the module is to provide an high-accuracy potentials that reproducing kernels (see Section **??**) can achieve. The existing potentials are substituted with a new three body term potential. It is intended to be used for spectroscopic purposes and, in case of single reference potentials, for reactive potentials.

The command is invoked using the keyword TRKN and has the following options: adding a new three body potential between three consecutive atoms and it is invoked by the ACTI keyword. The command CLEA removes the list of added potential, reactivating the classical force field.

As in the case of EXTBOND, in order to perform calculations with this potential a grid in form of a *csv* file is needed. This file is composed by four columns, the first three are generic coordinates (x_i, y_i, z_i) along which the potential energy surface is explored in increasing order of $(x_1, y_1, z_1;x_1, y_1, z_2;...;x_1, y_2, z_1;...;x_2, y_1, z_1;...)$ and the last one is energy. Also in this case the asymptotic energy is need for referencing the energies to the asymptote, $E - E_{asymp}$, such that $E_{asymp} = 0$ for the correct behaviour of kernels at long distances.

There are three coordinates (shown in Figure 6.3) system that can be used for generating the grid file:

int1: $K(\alpha, r_1, r_2)$. This kernel uses two interatomic distances, r_1 and r_2, and the angle α defined by these two vector.

int2: $K(r_1, r_2, r_3)$. This kernel uses three interatomic distances, r_1, r_2, and r_3.

jaco: $K(\theta, R, r)$. This kernels uses the Jacobi coordinates[64], one interatomic distance r, the distance between the center of mass of the r (x_{cm}) vector and the the third atom involved in the potential and the angle θ defined by the R and the vector along x_{cm} and the second atom.

The advantage of using this module is in the implicit inclusion of coupling between the

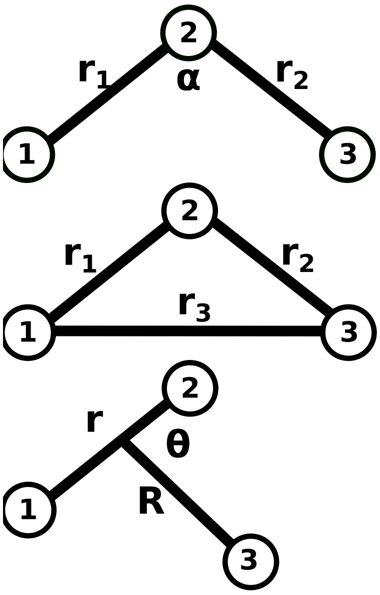

Figure 6.3.: From top to bottom: The representation of the three coordinates system implemented in triakern: int1,int2 and jaco.

normal modes of the involved atoms, recovering a good agreement with the electronic structure calculations. Figure 6.4 shows an example of a molecule described by the TRIAKERN potential.

The current implementation is tested with ${N_3}^-$ kernel, previously implemented in an home brew version of CHARMM. The kernel is stored in Jacobi coordinates with a MRCI+Q/AVQZ level of theory. Further details on the distribution of the *ab-initio* points are in Ref[65]. Simulations were carried out in gas phase for 500 ps with a $\Delta t = 0.25$ fs at 300 K and vibrational spectrum was obtained through the power spectrum technique. A disagreement of less than 10 cm^{-1} is found for the symmetric (1307 vs 1315 cm^{-1}) and asymmetric stretching (1996 vs 2005 cm^{-1}), while a more consistent discrepancy is found for the bending motion (43 cm^{-1}, 637 vs 680 cm^{-1}). It happens because the simulation was performed with a different simulation setup respect to the original simulations. Results of this example calculations are in Figure 6.5.

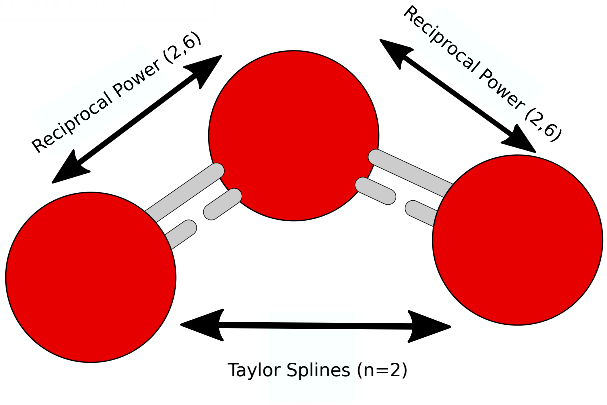
Reciprocal Power (2,6)
Reciprocal Power (2,6)
Taylor Splines (n=2)

Figure 6.4.: Example of molecule (O_3) described using the TRIAKERN potential with the int1 coordinates system. For each mode the used kernel is indicated. Their description is found in Section **??**

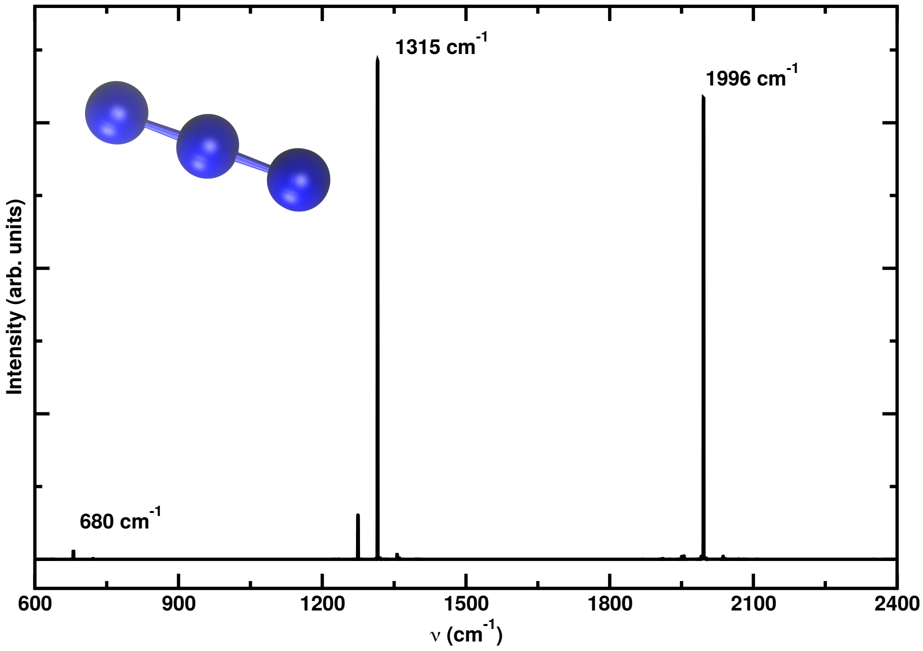

Figure 6.5.: IR spectrum of N_3^- obtained *via* power spectrum.

Bibliography

[1] T. Hama and N. Watanabe, *Chem. Rev.*, 2013, **113**, 8783–8839.

[2] K. Kuwahata, T. Hama, A. Kouchi and N. Watanabe, *Phys. Rev. Lett.*, 2015, **115**, 133201.

[3] V. Ásgeirsson, H. Jónsson and K. T. Wikfeldt, *J. Phys. Chem. C*, 2017, **121**, 1648–1657.

[4] B. Senevirathne, S. Andersson, F. Dulieu and G. Nyman, *Mol. Astrophys.*, 2017, **6**, 59 – 69.

[5] R. Smoluchowski, *J. Phys. Chem.*, 1983, **87**, 4229–4233.

[6] M. Minissale, E. Congiu, S. Baouche, H. Chaabouni, A. Moudens, F. Dulieu, M. Accolla, S. Cazaux, G. Manicó and V. Pirronello, *Phys. Rev. Lett.*, 2013, **111**, 053201.

[7] H. S. Chung, S. Piana-Agostinetti, D. E. Shaw and W. A. Eaton, *Science*, 2015, **349**, 1504–1510.

[8] F. H. Stillinger, *Science*, 1995, **267**, 1935–1939.

[9] R. Zwanzig, *Proc. Natl. Acad. Sci.*, 1988, **85**, 2029–2030.

[10] F. Dausinger and H. Schultz, *Phys. Rev. Lett.*, 1975, **35**, 1773–1775.

[11] T. D. Swinburne, P.-W. Ma and S. L. Dudarev, *New J. Phys.*, 2017, **19**, 073024.

[12] Minissale, M., Congiu, E. and Dulieu, F., *Astron. Astrophys.*, 2016, **585**, A146.

[13] J. Huang and A. D. MacKerell Jr, *J. Comp. Chem.*, 2013, **34**, 2135–2145.

[14] L. Bytautas, N. Matsunaga and K. Ruedenberg, *J. Chem. Phys.*, 2010, **132**, 074307.

[15] A. Warshel and R. M. Weiss, *J. Am. Chem. Soc.*, 1980, **102**, 6218.

[16] U. Schmitt and G. Voth, *J. Phys. Chem. B*, 1998, **102**, 5547.

[17] J. Danielsson and M. Meuwly, *J. Chem. Theory Comput.*, 2008, **4**, 1083.

[18] T. Nagy, J. Yosa Reyes and M. Meuwly, *J. Chem. Theory Comput.*, 2014, **10**, 1366–1375.

[19] N. Kumagai, K. Kawamura and T. Yokokawa, *Mol. Sim.*, 1994, **12**, 177–186.

[20] P. K. Gupta and M. Meuwly, *Faraday Discuss.*, 2013, **167**, 329–346.

[21] N. Plattner and M. Meuwly, *ChemPhysChem*, 2008, **9**, 1271–1277.

[22] M. W. Lee and M. Meuwly, *Faraday Discuss.*, 2014, **168**, 205–222.

[23] H.-C. Chang and G. E. Ewing, *Phys. Rev. Lett.*, 1990, **65**, 2125–2128.

[24] S. A. Corcelli and J. C. Tully, *J. Phys. Chem. A*, 2002, **106**, 10849–10860.

[25] Y. Yu, M. Wang, D. Zhang, B. Wang, G. Sant and M. Bauchy, *Phys. Rev. Lett.*, 2015, **115**, 165901.

[26] J. C. Phillips, *Rep. Prog. Phys.*, 1996, **59**, 1133–1207.

[27] J. R. Stine and J. T. Muckerman, *J. Chem. Phys.*, 1976, **65**, 3975–3984.

[28] L. D. Landau, *Phys. Z*, 1932, **2**, 46–52.

[29] C. Zener, *Proc. R. Soc. London A*, 1932, **137**, 696–702.

[30] D. G. Fedorov, S. Koseki, M. W. Schmidt and M. S. Gordon, *Int Rev Phys Chem*, 2003, **22**, 551–592.

[31] A. C. Stanton and C. E. Kolb, *J. Chem. Phys.*, 1980, **72**, 6637–6641.

[32] M. A. Robb, M. Garavelli, M. Olivucci and F. Bernardi, in *A Computational Strategy for Organic Photochemistry*, John Wiley & Sons, Ltd, 2007, pp. 87–146.

[33] R. Hernández, R. Toumi and D. C. Clary, *J. Chem. Phys.*, 1995, **102**, 9544–9556.

[34] J. Campos-Martìnez, E. Carmona-Novillo, J. Echave, M. Hernández, R. Hernández-Lamoneda and J. Palma, *Chem. Phys. Lett.*, 1998, **289**, 150 – 155.

[35] R. T. Jongma, S. Shi and A. M. Wodtke, *J. Chem. Phys.*, 1999, **111**, 2588–2594.

[36] S. Shin and A. P. Willard, *J. Chem. Theo. Comp.*, 2018, **14**, 461–465.

[37] K. El Hage, F. Hédin, P. K. Gupta, M. Meuwly and M. Karplus, *eLife*, 2018, **7**, e35560.

[38] B. R. Brooks, C. L. Brooks III, A. D. Mackerell Jr., L. Nilsson, R. J. Petrella, B. Roux, Y. Won, G. Archontis, C. Bartels, S. Boresch, A. Caflisch, L. Caves, Q. Cui, A. R. Dinner, M. Feig, S. Fischer, J. Gao, M. Hodoscek, W. Im, K. Kuczera, T. Lazaridis, J. Ma, V. Ovchinnikov, E. Paci, R. W. Pastor, C. B. Post, J. Z. Pu, M. Schaefer, B. Tidor, R. M. Venable, H. L. Woodcock, X. Wu, W. Yang, D. M. York and M. Karplus, *J. Comp. Chem.*, 2009, **30**, 1545–1614.

[39] D. Anderson, T. C. Terwilliger, W. Wickner and D. Eisenberg, *J. Biol. Chem.*, 1980, **255**, 2578–2582.

[40] U. Essmann, L. Perera, M. L. Berkowitz, T. Darden, H. Lee and L. G. Pedersen, *J. Chem. Phys.*, 1995, **103**, 8577–8593.

[41] Y.-K. Cheng and P. J. Rossky, *Nature*, 1998, **392**, 696.

[42] J.-P. Ryckaert, G. Ciccotti and H. J. Berendsen, *J. Comp. Phys.*, 1977, **23**, 327 – 341.

[43] A. P. Willard and D. Chandler, *J. Phys. Chem. B*, 2010, **114**, 1954–1958.

[44] M. Perutz, *Nature*, 1970, **228**, 726–734.

[45] S.-Y. Park, T. Yokoyama, N. Shibayama, Y. Shiro and J. R. Tame, *J. Mol. Biol*, 2006, **360**, 690 – 701.

[46] M. M. Silva, P. Rogers and A. Arnone, *J. Biol. Chem.*, 1992, **267**, 17248–17256.

[47] G. B. Vasquez, X. Ji, C. Fronticelli and G. L. Gilliland, *Acta Crystallogr.,Sect.D*, 1998, **54**, 355–366.

[48] A. Nakagawa, F. E. Lui, D. Wassaf, R. Yefidoff-Freedman, D. Casalena, M. A. Palmer, J. Meadows, A. Mozzarelli, L. Ronda, O. Abdulmalik, K. D. Bloch, M. K. Safo and W. M. Zapol, *ACS Chem.Biol.*, 2014, **9**, 2318–2325.

[49] T. Ichiye and M. Karplus, *Prot. Struct. Funct. Genom.*, 1991, **11**, 205–217.

[50] M. Karplus and T. Ichiye, *J. Mol. Biol.*, 1996, **263**, 120–122.

[51] T. C. Terwilliger and D. Eisenberg, *J. Biol. Chem.*, 1982, **257**, 6010–6015.

[52] M. Devereux, S. Raghunathan, D. G. Fedorov and M. Meuwly, *J. Chem. Theory Comput.*, 2014, **10**, 4229–4241.

[53] O. T. Unke, M. Devereux and M. Meuwly, *J. Chem. Phys.*, 2017, **147**, 161712.

[54] J. A. Rackers, Z. Wang, C. Lu, M. L. Laury, L. Lagardère, M. J. Schnieders, J.-P. Piquemal, P. Ren and J. W. Ponder, *J. Chem. Theory Comput.*, 2018, **14**, 5273–5289.

[55] P. Eastman, J. Swails, J. D. Chodera, R. T. McGibbon, Y. Zhao, K. A. Beauchamp, L.-P. Wang, A. C. Simmonett, M. P. Harrigan, C. D. Stern, R. P. Wiewiora, B. R. Brooks and V. S. Pande, *PLOS Comput. Biol*, 2017, **13**, 1–17.

[56] L.-P. Wang, T. Head-Gordon, J. W. Ponder, P. Ren, J. D. Chodera, P. K. Eastman, T. J. Martinez and V. S. Pande, *J. Phys. Chem. B*, 2013, **117**, 9956–9972.

[57] W. Wagner and A. Pruß, *J. Phys. Chem. Ref. Data*, 2002, **31**, 387–535.

[58] R. Mills, *J. Phys. Chem.*, 1973, **77**, 685–688.

[59] P. Ren and J. W. Ponder, *J. Phys. Chem. B*, 2003, **107**, 5933–5947.

[60] F. Hédin, K. El Hage and M. Meuwly, *J Chem Inf Model*, 2016, **56**, 1479–1489.

[61] J. A. Anderson and G. S. Tschumper, *J. Phys. Chem. A*, 2006, **110**, 7268–7271.

[62] N. L. Allinger, Y. H. Yuh and J. H. Lii, *J. Am. Chem. Soc.*, 1989, **111**, 8551–8566.

[63] P.-A. Cazade, F. Hédin, Z.-H. Xu and M. Meuwly, *J. Phys. Chem. B*, 2015, **119**, 3112–3122.

[64] M. Karplus, R. N. Porter and R. D. Sharma, *J. Chem. Phys.*, 1966, **43**, 3259–3287.

[65] S. M. Salehi, D. Koner and M. Meuwly, *J. Phys. Chem. B*, 2019, **123**, 3282–3290.

Curriculum Vitae

Personal Information

Name: Marco Pezzella

Address (CH): Rudolfstrasse 44, 4054 Basel, Switzerland

Address (IT): Viale Abruzzo 229, 66100 Chieti (CH), Italy

e-mail: marco.pezzella@unibas.ch,

Date of birth: 20.02.1989, Chieti (CH), Italy

Nationality: Italian

Education

PhD Studies Chemistry **May 2015 - May 2020**

- University of Basel, Basel, Switzerland
- Dissertation Topic: "Molecular dynamics simulations at water interface: astrochemical and biological applications"
- Advisor: Markus Meuwly
- External Referee: Jonathan Tennyson

MSc in Chemistry **September 2012 - December 2014**

- University of Rome “La Sapienza”, Rome, Italy
- Dissertation Topic: “Theroertical study on the Photochemistry of Nitroaromatic compounds: Phenols and Toluenes”
- Advisor: Enrico Bodo

BSc in Chemical and Material Science and Technologies

October 2008 - March 2012

- University of L’Aquila, L’Aquila, Italy
- Dissertation Topic: “Computational study of truxene aggregation”
- Advisor: Fabio Ramondo

Publications

- Pezzella M, El Hage K, Niesen M. J.M, Shin S, Willard A P, Meuwly M, Karplus M. **Water Dynamics Around Proteins: T- and R-States of Hemoglobin and Melittin.** *The Journal of Physical Chemistry B.* 2020 Jun 26; $XXX(XXX)$:A-O
- Pezzella M, Koner D, Meuwly M. **Formation and Stabilization of Ground and Excited-State Singlet O_2 upon Recombination of 3^P Oxygen.** *The Journal of Physical Chemistry Letters.* 2020 Feb 14;11(6):2171-6.
- Pezzella M, Meuwly M. **O_2 formation in cold environments.** *Physical Chemistry Chemical Physics.* 2019;21(11):6247-55.
- Pezzella M, Unke OT, Meuwly M. **Molecular Oxygen Formation in Interstellar Ices Does Not Require Tunneling.** *The Journal of Physical Chemistry Letters.* 2018 Mar 26;9(8):1822-6.

- Ciavardini A, Coreno M, Callegari C, Spezzani C, De Ninno G, Ressel B, Grazioli C, de Simone M, Kivimaki A, Miotti P, Frassetto F , Poletto L, Puglia C, Fornarini S, Pezzella M, Bodo E, Piccirillo, S. **Ultra-Fast-VUV Photoemission Study of UV Excited 2-Nitrophenol.** *The Journal of Physical Chemistry A*. 2019 Jan 22;123(7):1295-302.

- Gomez-Esteban S, Pezzella M, Domingo A, Hennrich G, Gómez-Lor B. **Solvent-Dependent Truxene-Based Nanostructures**. *Chemistry–A European Journal.* 2013 Nov 18;19(47):16080-6.

Publications in preparation

- Devereux M, Pezzella M, Raghunathan S, Meuwly M. **A Distributed Charge Approach to Molecular Dynamics Simulations of Atom-Centered, Off-Centered and Multipolar Polarizable Water Models**

Presentations

- **Swiss Chemical Society Fall Meeting, Zürich, Switzerland, September 2019.** "Molecular Dynamics simulations with RKHS based potentials " oral presentation.

- **Swiss Chemical Society Fall Meeting, Lausanne, Switzerland, September 2018.** " Formation of molecular oxygen in astrochemical conditions." Oral presentation.

© Gainax Co. Ltd
REC
LOCATION
UN UNDERGROUND BASE 02
AUG 15 2000 09:31:18

Keel: Scienziati... ripongono sempre eccessiva fiducia nelle proprie idee.

Gendō: Una forma di egocentrismo?

Keel: Sono uomini troppo rigidi nelle loro convinzioni, e pertanto incapaci di comprendere appieno la realtà.

Gendō: Eppure proprio quegli stessi uomini vanno alla ricerca della verità... quale ironia.

Keel: Loro non sono tanto nobili. Le scoperte sono fonte di gioia, e la comprensione sfocia nel dominio. Ciò che in effetti cercano, è soltanto il proprio piacere.

Neon Genesis Evangelion, Episode 21, Nerv, la nascita / He was aware that he was still a child